UCRL-19046

cy. 2

MICRO-MECHANICAL APPROACH TO STRESS CORROSION CRACKING IN TITANIUM ALLOYS

RECEIVED
LAWRENCE
RADIATION LABORATORY

OCT 23 1969

LIBRARY AND
DOCUMENTS SECTION

Yosef Katz
(Ph. D. Thesis)

September 1969

AEC Contract No. W-7405-eng-48

TWO-WEEK LOAN COPY

This is a Library Circulating Copy which may be borrowed for two weeks. For a personal retention copy, call Tech. Info. Division, Ext. 5545

LAWRENCE RADIATION LABORATORY
UNIVERSITY of CALIFORNIA BERKELEY

UCRL-19046
cy. 2

DISCLAIMER

This document was prepared as an account of work sponsored by the United States Government. While this document is believed to contain correct information, neither the United States Government nor any agency thereof, nor the Regents of the University of California, nor any of their employees, makes any warranty, express or implied, or assumes any legal responsibility for the accuracy, completeness, or usefulness of any information, apparatus, product, or process disclosed, or represents that its use would not infringe privately owned rights. Reference herein to any specific commercial product, process, or service by its trade name, trademark, manufacturer, or otherwise, does not necessarily constitute or imply its endorsement, recommendation, or favoring by the United States Government or any agency thereof, or the Regents of the University of California. The views and opinions of authors expressed herein do not necessarily state or reflect those of the United States Government or any agency thereof or the Regents of the University of California.

TABLE OF CONTENTS

ABSTRACT

I. INTRODUCTION ---------- 1

II. EXPERIMENTAL ---------- 4

A. Material ---------- 4

B. Tensile and Fracture Toughness Tests ---------- 4

C. Stress Wave Instrumentation ---------- 5

D. Environment Tests ---------- 6

E. Metallography and Fractography ---------- 8

III. EXPERIMENTAL RESULTS AND OBSERVATIONS ---------- 10

A. Materials ---------- 10

B. Mechanical Properties and Fracture Toughness Results ---------- 11

C. Environment Tests Results ---------- 13

1. Fracture Criteria and Time to Failure ---------- 13

2. Slow Crack Growth Velocities ---------- 14

3. SWE-Observations and Results ---------- 16

D. Cracking Observations and Fracture Surface Investigations ---------- 18

E. Temperature Effects ---------- 20

IV. DISCUSSION ---------- 22

A. General ---------- 22

B. Mechanics Aspects ---------- 23

1. Energy Balance Considerations ---------- 23

2. Stress Intensity Parameters and Crack Velocity ---------- 26

C. Metallurgical Condierations ---------- 28

D. Electrochemical Aspects ---------- 32

E. Fracture Classification ---------- 33

F. Mechanism ---------- 33

V. CONCLUSIONS ---------- 39

APPENDIX I ---------- 41

APPENDIX II ---------- 43

ACKNOWLEDGEMENTS ---------- 46

REFERENCES ---------- 47

FIGURE CAPTIONS ---------- 52

TABLES AND FIGURES ---------- 56

MICRO-MECHANICAL APPROACH TO STRESS CORROSION CRACKING IN TITANIUM ALLOYS

Yosef Katz

Inorganic Materials Research Division, Lawrence Radiation Laboratory,
Department of Materials Science and Engineering of the College of Engineering,
University of California, Berkeley, California

ABSTRACT

SCC in Ti-aqueous 3-1/2% NaCl systems were investigated on pre-cracked specimens under constant load. Materials tested were commerically pure Ti-75A, alpha-beta Ti-8Al-1Mo-1V and Ti-5Al-2.5Sn, and all beta Ti-13V-11Cr-3Al alloys. Contoured specimens, with stress intensity (K) independent of crack length, allowed a determination of the crack propagation rate dependence on K. Such a relationship was utilized for evaluating the total time to failure in a single-edge notch specimen since K=f(c) was available.

An acoustic emission technique was designed for investigating the micro-mechanical nature of SCC. Acoustic emission results as well as fractographic evidence show the process to be discontinous slow crack growth. Corrolation between stress wave emission activity and crack velocity was shown with a higher velocity being associated with more frequent activity and larger wave amplitudes. Transgranular cleavage dominated the fracture surface under active environmental conditions. In the Ti-13-11-3 the cleavage was on the {100} planes.

Tests performed at different temperature show SCC to be a thermally activated process. The apparent activation energy was about 9.5 kcal/mole for the Ti-75A, 4.5 kcal/mole for the Ti-5-2.5 and ranged from 2.3 to 3.5 kcal/mole for the Ti-8-1-1. In the latter the apparent activation

energy was affected by the applied stress intensity factor. Consequently a thermally activated triggering mechanism, combined with a mechanically controlled crack jump was proposed. The initiation and reinitation of the crack step was attributed to a diffusion controlled process while the crack step was attributed to a mechanical driving force. Introducing a mechanical term in the rate equation both the low apparent activation energy observed as well as the high crack velocity could be explained. Hydrogen embrittlement was hypothesized to be a possible mechanism for the thermally activated process.

I. INTRODUCTION

Stress corrosion cracking (SCC) is a complex phenomenon involving a combination of electrochemical as well as mechanical processes (i.e. two major interacting influences). SCC refers to the cooperative influence of a chemically active environment and some stress system (static, dynamic, or residual) on the mechanical properties of a material, and specifically on the materials resistance to crack initiation and propagation. SCC is generally characterized by a relatively slow rate propagation which can be reduced or stopped by cathodic polarization. In contrast, hydrogen embrittlement is enhanced by cathodic polarization because of the increased production of hydrogen which enters and embrittles the metal.

It is obvious from information gathered to date that no single mechanism can account for all of the phenomena observed. Many variables, both macroscopic and microscopic, affect SCC.

The present work is oriented toward the mechanical aspects of SCC. It takes into consideration the importance of a well defined stress system, an essential requirement for a systematic investigation of a SSC phenomenon. Linear fracture mechanics concepts[1,2] were used, which provided a quantitative background for the local state of stress, quantitative estimates of plastic zone size, geometry effects, catastrophic crack instability, and to a lesser extent slow crack growth. The latter is a form of steady state behavior in which the critical stress intensity factor K_{Crit} (or the elastic strain energy release rate G_{Crit}) is alternatively slightly greater then slightly less than the materials resistance to crack propagation. Fatigue pre-cracked notch specimens were used to enhance SCC.

The parameter considered was the stress intensity factor defined in the neighborhood of a crack by:

$$\sigma_{ij} = \frac{K}{(2\pi r)^{1/2}} f_{ij}(\theta) \qquad (1)$$

where r, θ are polar coordinates centered at the crack tip, $f_{ij}(\theta)$ is dependent upon the particular stress component but not on the specimen geometry or applied load. K is called the stress intensity factor which is the same for all stress components.

The applied stress intensity factor was called K_i and was used to define the stress state in the region around the crack tip when SCC is involved. Two particular limits for the stress intensity factor should be defined. First K_{ISCC} which is the upper limit of the applied stress intensity factor that will not cause the material to fail in a finite time. Secondly K_{Crit} which is the lower limit of the stress intensity factor which will cause the material to fail in the absence of an active chemical environment. K_{Crit} therefore is dependent on specimen geometry, which might apply also to K_{ISCC} in case of a mechanism controlled by the plastic zone developed at the crack tip.

The fracture mechanics approach is useful for determining the relationships between "time to failure" or crack growth rate and the stress intensity factor. This approach was used by McEvily and Bond[3] for cold rolled brass, by Weber and McEvily for Al alloys,[4] and by Johnson and Willner[5] for H-11 steels.

Since plastic strain is involved in the nucleation of cracks, K_i can be considered to be a parameter related to the plastic behavior at the crack tip.

The materials selected for investigation were commerically pure Ti and three Ti-alloys. The work on Ti alloys dates back to the early

1960s. The phenomenon of SCC was observed in commerically pure Ti,[6] but not in an aqueous environment. Within the past three years it has become evident that SCC in titanium alloys is a potentially serious problem. The environment used in the recent work was aqueous (3-1/2% NaCl) which, as shown by Brown,[7] can cause SCC in Ti-alloys.

The role of microstructure can be studied with titanium alloys. The important phases include 100% α, $\alpha + \beta$, α + less β and 100% β. The microstructural investigation is interesting because of the possibility of evaluating the relative susceptibilities of the two phases to SCC and the results of the investigation have the potential for being useful in developing alloys that are less susceptible to SCC.

The experimental program did not include electrochemical studies; information of this type was taken from the literature.[8-10]

Data on time to failure and on crack propagation rates were obtained with edge notch specimens and crack line-loaded edge crack specimens of the types shown in Figs. 3 and 4. Information has been accumulated on the fracture characteristic and modes. Examinations were made by means of light microscopy, electron microscopy, and scanning electron microscopy. The experiments also included determination of the temperature dependence of crack growth rates and measurements of apparent activation energies. A technique was devised to differentitate between the electrochemical mechanism and the brittle-crack stage mechanism of crack growth. It involved the use of stress wave emission measurements. The experimental results obtained in this investigation were evaluated in terms of the various mechanisms proposed by Logan,[10] West,[11] Uhlig,[12] and Pugh[13] as well as others.[3,14,15]

II. EXPERIMENTAL

A. Material

The work was carried out on Ti-systems comprising four different commercial materials as described below.

1. Ti-75A (unalloyed), annealed at 700°C for 2 hr - AC
2. Ti-8Al-1Mo-1V, annealed at 780°C for 8 hr - FC
3. Ti-5A-2.5Sn, annealed at 760°C for 2 hr - AC
4. Ti-13V-11Cr-3Al, annealed for 10 min at 780°C - AC

All materials were in sheet form; they were 0.125 in. thick. Alloys 2 and 3 contained α mixed with β phase. The chemical compositions are given in Table I. Pure elements are not generally considered to be susceptible to SCC. However, commercially pure Ti could be because of impurity elements like oxygen. The Ti-75A alloy served as a basis for comparison with the two phase alloys, as did the single phase β alloy.

B. Tensile and Fracture Toughness Tests

Uniaxial tensile tests were performed at room temperature on sheet specimens with 2 in. gage lengths and 0.250 in. widths. The test for all of the materials was made in a 5000 kg Instron machine using a crosshead speed of 0.08 in./min. Elastic modulus and plastic elongation data were obtained with a standard Instron extensometer. Fracture toughness values were measured on fatigued precracked specimens. The geometry selected was the compact crack line loaded type of specimen used by Manjoine[16] and Ripling.[17] This geometry has the mechanical advantage of good ratios of applied load to stress intensity factors, both c/W and H/W (c is specimen crack length and H is half of the specimen length, and W is the specimen width) were about 0.6 as recommended by Brown and Srawley.[18] The specimen configuration is shown in Figs. 2-4. The pre-fatigue

cracking was done by tension-tension fatigue, controlled to a minimum of 20,000 cycles for about 0.070 in. crack extension, which corresponds to more than half the specimen thickness. The fracture tests were made on an Instron using a crosshead speed of 0.04 in/min, and K_{Crit} was determined from the relationship:

$$K_{Crit} = \frac{P_{Crit}}{BW^{1/2}} \; f\,(c/W) \qquad (2)$$

where P is the applied load, B is specimen thickness and f(c/W) is a correction function due to the finite specimen width. These correction function values were taken from the literature.[18] Fracture toughness tests were made on relatively thin specimens. The stress wave emission (SWE) technique was utilized to assist in determining K_{Ic} values. This technique can indicate bursts of stress waves associated with local instabilities even before catastrophic failure. This is a more sensitive way to determine the macroscopic "pop-in," which is used for establishing plane strain values in relative thin specimens. More details on the SWE technique are given in the next paragraph.

C. Stress Wave Instrumentation

The micromechanics of the crack growth in air and in the corrosive environment were investigated by the use of the SWE technique. When crack growing is associated with discontinuous local instabilities, as is the case of cleavage jumps, elastic stress waves are emitted which can be detected and monitored by a piezoelectric transducer attached to the specimen under test.[19] The set-up is schematically shown in Fig. 5. Care was taken to obtain a sensitive detection system.

Preliminary work had shown that when mechanical stress waves are emitted in these systems, they are caused by the formation of very small cracks which release small amounts of energy when they form. These stress waves were of such low amplitude that they could have been masked by the background noise level, so it was necessary to devise equipment that had a very high signal gain and a low noise level. The Endevco transducer used for detecting the stress waves was a model No. 2234E with mechanical resonance of about 34 KHz and a charge sensitivity of 59.5 picocoulomb/g. The signals from the accelerometer were amplified by charge and voltage amplifiers to provide a combined gain of about 60,000. The band of frequencies after filtering were between 30 KHz and about 48 KHz. The signal was recorded on a Mincom C-100 tape recorder with frequency response of 50 Hz-60KHz at 30 in./sec. The recorded data could be played back and observed on an oscilloscope, and a strip chart record, with proper reduction of speed, could be made from the taped record.

D. Environment Tests

The SCC tests were performed in a 3-1/2% NaCl aqueous solution on precracked fatigue specimens subjected to a constant load. All tests were made on a 300,000 lbs capacity MTS tensile machine as shown in Fig. 1. Two specimen geometries were used. The first was a single edge notched (SEN) specimen 3 in. × 10 in. with an initial c/W of about 0.2, and the second was a tapered specimen of the kind used by Ripling[17] and Mostovoy.[20] The SEN specimen was selected for obtaining data on total time for failure (the value being dependent on specimen geometry) as a function of the applied K_I. Here the emphasis was on the initial portion of the curve, i.e., the region where the delayed failure involved short times. The

assumption used to establish a value for K_{ISCC} was that a delayed failure of more than 60 minutes would be defined as "no failure," for the purpose of this report. The SEN specimen provided a reasonable range for slow crack growth that could be followed before catastrophic failure occurred, at the same time the SEN specimen provides only one source for possible stress waves. The initial stress intensity factor was changed by varying the applied load. This type of specimen was also instrumented to provide data on the crack growth kinetic and stress wave emission data. The crack propagation rate was measured by using a crack opening displacement gage, with linear characteristic in the working range, which was attached to the specimen as shown in Fig. 3. The measured surface displacement could be related by means of a nondimensional calibration to the crack length so that the velocity could be determined as a function of crack length. The emitted stress waves were monitored during the experiment and were then related to the crack propagation rate and the applied K_i as well as the time for failure.

The tapered specimen (See Appendix I) was used specifically to obtain precise values of crack velocities where very small changes occur in K as the cracks grew. (In the SEN specimen K varies considerably as the crack grows.) Stress wave emission data were also collected from these specimens.

The temperature effect on SCC was studied only on tapered specimens, and in a temperature range of about 70°C, for the purpose of establishing the apparent activation energy for the process. The influence of temperature on the nature of the stress waves was studied for several different values of K_i.

E. Metallography and Fractography

Standard metallography techniques were used to determine the microstructures of the materials investigated. Primary and secondary cracks were observed after SCC tests. The relation of the cracking pattern to the microstructural background was studied to augment information about crack growth. The physical characteristics of cracking, whether intergranular or transgranular, the cracking preference of phases, and the crystallographic nature of cracking could be observed with these techniques. Additional information on crack propagation features was also determined by other methods. The relationship between secondary cracks and slip bands was examined by using etched cracked specimens of Ti-13-11-3 which had relatively coarse grains. Specimens of this alloy were plastically deformed locally by a microhardness indenter to obtain slip band patterns as well as cracks. The observations were made with a light microscope and at magnifications of up to 1000×. Most of the specimens were electropolished with Blackhorn solution[21] and etched with a reagent[22] containing 60% glycerine, 20% NO_3, and 20% HF. The Ti-75A alloy was anodized after electropolishing with a solution containing 60 ml ethanol, 35 nl H_2O, 5 ml phosphoric acid, 10 ml latic, 20 ml glycerin, and 2 g citric acid. A portential of 20 V was applied for 15 seconds.

The fracture surface morphology was studied by means of carbon replication using the electron microscope at magnifications between 3000 and 20,000×. A two step replication technique was employed using acetyle cellulose tape as the first layer. After stripping, the plastic was shadowed with platinum-palladium at an angle of approximately 45°. Therefore carbon was deposited for the second step. Paraffin was placed

on the replica to strengthen it during dissolution of the acetyle cellulose.

Complimentary information was obtained with a scanning electron microscopy at magnifications up to 3000×. The fracture area in the slow crack growth region (under the active media) was compared with the fracture surface in the catastrophic failure region. For the Ti-13-11-3 alloy particular emphasis was plated on studies of the crystallographic habit of cracking as well as the roll of grain boundaries or phase interfaces on the fracture characteristic..

III. EXPERIMENTAL RESULTS AND OBSERVATIONS

A. Materials

The microstructures of the materials investigated are shown in Fig. 6. The Ti-75A had a single phase α structure with a grain size of about 25μ. The Ti-8-1-1 and the Ti-5-2.5 alloys had a multi-phase structure, consisting of an α matrix containing a dispersion of β. The grain sizes were about 10μ and 15μ respectively. The Ti-13-11-3 was 100 percent β. It had relatively coarse grains of about 150μ.

The single phase materials were examined with an electron beam microprobe analyzer to establish the uniformity of composition. Concentration of the alloying elements Fe, V, Cr, and Al were checked using the K_α x-ray characteristic emission of these elements. The electron acceleration potential was 20 kV. Counting results did not show differences in concentration or segregation at grain boundaries. Statistically, the materials appeared to be uniform. For the multiphase materials, Mo and Sn were checked in addition to the elements mentioned above. The L_α characteristic emission was used for Mo and Sn determinations.

For the Ti-8-1-1 alloy, counts were taken within the α and within the β phases as well as across α/β boundaries. Figure 7 represents qualitatively the result obtained. It shows the microstructural morphology besides the specimen current projection and the line profile for the scanning beam. Similar information was obtained for the Ti-5-2.5 alloy, which also showed different solubilities of the heavy elements in the β phase. The current projection image and the microstructure image after etching are similar in these two cases. Looking at the counting data for the Ti-8-1-1, the Al concentration appeared to be uniform so it was

evident that any Ti-Al intermetallic compound that might have formed would have had to be in the form of very fine particles. There was a consistent tendency for the Al to be in higher concentration in the α phase as compared to the β phase although the differences in solubilities are small. The Mo in the Ti-8-1-1 alloy resided wholly in the β phase with the concentration therein being about 2-1/2 wt.%. The V concentration was about twice as high in the β phase as in the α. The Fe was totally contained in the β phase.

For the Ti-5-2.5 alloy, similar results were found for the Al, and Fe, while the Sn element was almost equally soluble in α and β. This information agrees in general with the expectation that α stabilizing elements like Mo, V and Fe are preferentially dissolved in the β phase.[22,23] One important point that must be borne in mind is that the α and β phases in the two alloys investigated were not chemically identical. The phases are designated according to their crystal structures. The different alloying elements in solution might be an important factor affecting the behavior during SCC. In addition, the possibility of formation of finely dispersed intermetallic compounds like Ti_3Al and changes in plastic deformation mechanisms produced by alloying elements should be considered.

B. Mechanical Properties and Fracture Toughness Results

The uniaxial tension test results are summarized in Table II and Figs. 8 and 9. The table shows the engineering stress-strain data and the elastic moduli needed for the calibration of specimens to obtain values of K, and crack length. The figures show the true stress ($\bar{\sigma}$) - true strain ($\bar{\epsilon}$) curves. They were computed by using the usual relationship of $\bar{\sigma} = P(1+e)/A_0$ and $\epsilon = \ln(1+e)$ (where P is the load, e is the engineering strain and A_0 is the initial cross section of the specimen), in

the uniform plastic deformation region, i.e. until necking starts. The last points of the curves were obtained from $\ell n(A_0/Af)$ and the actual load at fracture, where A_f is the specimen cross section at fracture. In general, all the materials investigated showed high ductility under static uniaxial tension loading. As can be seen from the data, minimum values of 15% elongation and 30% reduction in area at fracture were obtained. Fracture toughness data obtained in air on compact crackline loaded specimens (2.5 in. × 3. in.) are shown also in Table II. Except for the T-8-1-1, which fractured catastrophically, the alloys failed in a typically ductile manner characterized by a tearing fracture process. The typical load-displacement curve for the notched specimen were linear for the Ti-8-1-1 while the others had a deviation from linearity before reaching maximum load. As mentioned the last type of curve may be characteristic of a ductile rupture in which the material's resistance to crack propagation increases with increasing stress intensity factor along a limited slow crack extension. The K_{IC} values were estimated by considering the loads where bursts of stress waves were emitted because the 0.125 in. thickness was too small to provide effective plane strain fracture toughness conditions. The K_{Crit} was computed by taking the maximum load and the corresponding crack length. K_{Crit} might be in the transition range between K_{IC} and K_C values. However, to establish K_C values, more information concerning the specimen thickness dependence is needed. In the case of Ti-8-1-1 the K_{Crit} was not established due to the slow crack growth uncertainty. Nevertheless, this value should be only slightly higher than 55.5×10^3 psi $\sqrt{\text{in.}}$ In case of the Ti-5-2.5, no stress waves were detected and the process of failure appeared very quiet without local crack instabilites that could be monitored. The fracture toughness data in general seemed to be in reasonably close agreement with values given

by others[24,25] for similar materials.

C. Environment Tests Results

1. Fracture Criteria and Time to Failure

The top macroscopic pictures given in Figs. 10, 11, 12 and 13 demonstrates the failure stages in the SEN (3 in. × 10 in.) specimen in a corrosive environment. Starting from the prefatigue crack, a region of slow crack growth followed. The length of this zone was dependent on the initial value of K_i. When a critical crack length was reached, the specimens fractured catastrophically with a completely different mode of fracture that could easily be distinguished macroscopically. It was concluded that the critical crack length corresponds to the critical stress intensity factor K_{Crit} characteristic of the material where crack growth instability would occur without an active chemical environment. In the SEN specimen used and under constant load, K varies with crack length as a rapidly increasing monotonic function. Initially, the cracks grew slowly, but when K approached K_{Crit} the material then failed at a high crack velocity. Figures 14 and 15 shows data relevant to this point for the four materials investigated. This figure needs some explanation. The general formula used to express K in a notched specimen was given by Brown and Srawley[18]

$$K = Y \sigma c^{1/2} \qquad (3)$$

where $Y = f(c/W)$ is the correction factor for finite width and crack geometry. They proposed that for the SEN specimen:

$$Y = 1.99 - 0.41\,(c/W) + 18.70\,(c/W)^2 - 38.48\,(c/W)^3 + 53.85\,(c/W)^4 \qquad (4)$$

This polynomial expression computed to fit experimental data and collocation solution was estimated also by a different expression:[26]

$$Y = f\ (c/W) \quad = \quad 2\left[\sin^2\left(\frac{c\pi}{W}\right) + \sec^2\left(\frac{c\pi}{W}\right)\right] \qquad (5)$$

which is more of a closed form solution. Using this expression for Y and realizing the constant load condition test, one obtains

$$\sigma \quad = \quad K\ f\ (c)\ 1/c^{1/2} \Big|_{W\ =\ \text{const.}} \qquad (6)$$

This dependence of stress vs $f(c)\ 1/c^{1/2}$ at fracture was plotted for different initial conditions. The linear dependence shows that the critical stress intensity factor at fracture was constant. This observation that K_{Crit} is independent of the initial conditions or independent on time-to-failure will be used later in Appendix II. The total time-for-failure data for the SEN specimens (3 in. × 10 in.) are shown in Figs. 16 and 17. The first observation is that all four materials showed high susceptibility to SCC. Observing the curves in more detailed way, the Ti-8-1-1 alloy seems to be the most susceptible to SCC under the environment used, considering the fracture times that are involved as well as the K_i level to be applied in order to stimulate the phenomena. The K_{ISCC} for the Ti-75A for the limited time of 1 hour was about $K_i/K_{Crit} = 0.7$, which is higher than $\left(K_i/K_{Crit} \leq 0.4\right)$ obtained for the alloys. In the case of Ti-13-11-3, the total time-to-failure was longer than that for the alpha or alpha-beta alloys for the same K_i, although measurements were affected by the tendency of the major crack to branch. It is possible that the times are slightly overestimated in Fig. 17, but it was still concluded that this alloy involved a slower crack growth process. Observation and measurements of crack propagation rates supported these conclusions.

2. <u>Slow Crack Growth Velocities</u>

The crack velocity relation to K_i is shown in Figs. 18 and 19. The data were plotted on log-log scale to show the relationship of $\bar{V}$ to K_i.

Obviously the total time-to-failure and the crack velocity are interrelated. The original idea was to measure the crack velocities on the tapered specimens so that $\bar{V}$ could be expressed as a function of K_i. Having such general information provides estimations of total time-to-failure under the same environment and test conditions of any notched specimen if $K_i = f(c/W)$ is known. Time-to-failure data alone provide very restricted information because they depend mainly on the specimen geometry. For the Ti-75A and Ti-8-1-1 alloy, crack growth rates were measured over the total K_i range. For Ti-5-2.5 and Ti-13-11-3 alloys, this could be done only at values of K_i well below the transition to accelerated crack propagation. This restriction was caused by crack branching effects which limited the use of the tapered specimen for the last two alloys at high stress intensity levels. The values for higher K_i in these alloys were determined from experimental data on the SEN specimen. The formulation aspects of the velocity dependent of K_i is given in Appendix II.

The velocity is strongly dependent on K_i above about $K_i = 95\times10^3$ psi$\sqrt{\text{in.}}$ for the Ti-75A. This result will be discussed later in terms of crack acceleration due to excess mechanical energy. This non-alloyed material is less susceptible to SCC than the others. The K_i needed to stimulate cracking was high, and the initial crack velocity was about 2×10^{-4} in/sec. The following example illustrates the nature of the velocity profile in the SEN specimen. During slow crack growth with $K_i \simeq 90\times10^{-3}$ ksi $\sqrt{\text{in.}}$, the total time for failure was 82 sec; 80 sec of this time involved an average velocity of 5×10^{-4} in/sec while the crack grew 0.175 in. in length. The remaining 0.135 in. growth occurred at an average velocity of about 0.07 in/sec. The Ti-8-1-1 alloy seemed to be the most susceptible to

SCC. The initial conditions were $K_i/K_{Crit} = 0.32$, with a velocity of about 1×10^{-3} in/sec at $K_i = 30\times10^3$ psi $\sqrt{in}$. The velocity was strongly dependent of K_i. Also, a mechanically dominated portion of the curve can be seen in Fig. 18 starting at about 58×10^3 psi $\sqrt{in}$. The Ti-5-2.5 alloy had similar characteristics, with the exception that the velocity below $K_i = 120$ psi $\sqrt{in}$. had a very small dependence on K_i. This case will be described assuming $\bar{V}$ = constant later on. The crack propagation rate for the Ti-13-11-3 alloy is given in Fig. 19 for a range of K_i from 50 ksi $\sqrt{in}$. to 95 ksi $\sqrt{in}$. The velocities in this range were slower than those of the other materials, even though the mechanically dominated part was still very high. This caused a rapid failure in the high K_i range but slower growth as the ratio K_i/K_{Crit} decreases, (Fig. 17).

3. <u>SWE - Observations and Results</u>

The SCC phenomenon in all of the materials tested was associated with stress wave activity. Figures 20 and 21 shows some representative illustrations of the monitored waves, which vary in amplitude and frequency of occurrences. Most of them were recorded from SEN specimens. At the beginning they were small in amplitude and less frequent and then they increased later on as the stress intensity factor became higher. The average stress waves amplitudes were about 0.001g with a noise level of about 0.0001g. Although the signal-to-noise ratio of 10:1 can be considered reasonably good, some small amplitude waves might still have been masked. This was a particular limitation in the Ti-8-1-1 alloy where the observed stress waves were small in amplitude. Figures 22 and 23 shows the relationship between SWE counts per unit time vs. K_i for Ti-75A and Ti-8-1-1 and Ti-5-2.5 alloys. From observing these data and the crack velocity data in Figs. 18 and 19 it can be concluded that the velocity and SWE/sec

are well correlated; the higher crack velocities were associated with greater numbers of waves per unit time. In general, the curves of velocity and SWE/sec vs. K_i have similar tendencies. The Ti-13-11-3 data were plotted differently in Fig. 23 i.e. SWE/sec vs. time, because crack branching prevented calculation of large K values. Here, the same characteristic of increasing numbers of SWE/sec as the crack growth rate increases was observed. The SWE counting taken from data stored on recording tape and analyzed on an oscilloscope screen is only of major waves of about $3\text{-}4\times10^{-4}$ g. The real SWE activity might have been much higher involving many more low energy stress waves. The major waves were records of major incremental crack formation so their importance is of primary concern.

Beside a qualitative picture of micromechnanical behavior during the slow crack propagation region, some quatitative estimations and remarks can be made. First, qualitatively, the SWE observations show longer incubation times between subscritical microcrack coalescence in the SEN at low stress intensity factors. At the same time small crack growth increments were involved. As the critical stress intensity factor was approached, incubation times decreased and crack increments became larger. The significant increase of the stress wave amplitudes as mechanical instability was approached support this conclusion. The amplitude increase was well above the value attributable to an increase in stress intensity factor. In the tapered specimen the stress wave activity was statistically much more uniform, but the frequency and magnitude changed markedly after significant crack propagation because of the stress intensity increase produced by the specimen edge effect. The magnitude of the waves was higher in the Ti-75A and Ti-13-11-3 than in the Ti-8-1-1 and Ti-5-2.5 alloys.

For quantitative estimations of the discontinuous crack growth, Gerberich and Hartbower's[19] relationship between incremental crack growth and stress wave activity was utilized. According to experimental work which included also 6Al-4V titanium alloy, they suggest a semi-empirical relationship of the form:

$$\Delta A \sim \frac{g^2 E}{K^2} \qquad (7)$$

where ΔA is the incremental area swept out by the crack, g is the stress wave amplitude, E is the elastic modulus, and K the applied stress intensity factor. Applying this relationship to smaller incremental areas by extrapolation[27] it is believed that the SWE results from average sources of the grain size magnitudes in area. Obviously the amplitude variations in the SEN suggest that at low K_i the growth increments were smaller in size than the grains, but increased to larger values of a few grains as K_i approached K_{Crit}. An average SWE in the Ti-13-11-3 corresponded to an amplitude of 0.0026 g at $K \simeq 90$ ksi $\sqrt{\text{in.}}$ This resulted in a theoretically determined increment of about 9×10^{-6} in.^{2} compared to 21×10^{-6} in.^{2} for circular grain size cross section of 150μ.

The tendency of much smaller amplitudes for the Ti-8-1-1 and Ti-5-2.5 alloys (compared with the T-13-11-3 and Ti-75A alloys at similar K_i) can be explained by assuming that the crack jumps are of the order of the grain size. A reduction in grain size will result in a decrease in amplitude because ΔA is proportional to g^2.

D. Cracking Observations and Fracture Surface Investigations

Figures 10,11,12 and 13 shows the fracture modes associated with SCC phenomena for the four materials. Following the prefatigued region (A) the slow crack growth region (B) appears as a cleavage mode for all the materials. The fracture surface changes completely in region C, where rapid fracture occurred because of the mechanical instability.

The Ti-75A showed less cleavage in the rapid growth region. This area had more long dimples (Figs. 10 and 24). The Ti-8-1-1 and Ti-5-2.5 alloys showed low energy small dimples indicating more ductile fracture behavior. In the Ti-13-11-3 the change in mode of fracture from region (B) to (C) was very great. Relatively high energy dimples dominated, with almost 100% dimpled fracture mode in (C). Region (B) did not reveal the formation of any chemical products due to the environment. The fracture surface of the Ti-8-1-1, Ti-5-2.5 alloys, which had multiphase structure of α/β did not clearly show a fracture pattern that could be related to either the α or the β phases.

Figures 25 and 26 are pictures showing the nature of the major crack path and the cracking behavior in region (B). In the Ti-75A no micro-secondary cracks formed, while secondary cracks were observed in the other materials. From this series of pictures, together with electron micrographs, it was concluded that in the slow crack growth region trans-granular fracture occurred. In the Ti-8-1-1 and Ti-5-2.5 alloys, no preferential fracture path could be established that indicated a higher susceptibility of one particular phase to attack.

For the Ti-8-1-1 alloy, Figs. 27 and 28 illustrates a typical observation of striations in the (B) region. The striations are very finely spaced and are in localized regions on the fracture surface. The number and size of these regions could not be related to locations of α or β phases. These observations will be discussed further in a later section.

Figure 29 shows an optical micrograph with secondary cracks in the Ti-13-11-2.5 alloy. Figure 30 shows a light micrograph and a scanning electron fractograph of secondary cracks around a grain boundary. These pictures illustrate the crystallographic nature of the environmentally

induced cracks in the β alloy. Because of its relatively large grain size, this alloy yielded some observations of the crystallographic aspect of fracture. However, the grain size was not large enough for easy x-ray investigation by the back-reflection Laue technique and so that alternative of trace analysis was used. Figures 31 and 32 shows more of the morphology of the fracture surface and the clear crystallographic nature of the microcracks. The chevron traces in Fig. 13B are well defined in Fig. 31B and they have a clear relationship to the cracking direction. Figure 33 shows a light micrograph with traces of slip bands around a microcrack, these traces were developed by local microplastic deformation near the existing crack. The fact that a maximum of 3 cracking directions could be observed in one grain and the nature of the 3 planes intersecting at 90°, as shown in Fig. 31A led to the assumption that the cracking planes were of the {100} type. In order to verify this assumption a single trace analysis was made, as illustrated on the stereographic projection in Fig. 34. The angles between cracks in a single grain were measured and listed in Table III. All of these angles are allowed, assuming that cracking is on the cube planes.

E. Temperature Effects

Figure 35 shows the results of temperature effects on the crack propagation rates. The tests were performed on tapered specimen in order to eliminate the stress intensity factor as a parameter. The data were plotted as the log of the crack velocity vs 1/T so that an "apparent activation energy" for the process could be determined. Further discussion of these tests will be considered later. The main point was to provide some information on role of the chemical action. The mechanical contribution was not expected to be affected by changing the temperature by only 65°C. (The tests were carried on in 5°C, RT, and about 70°C.)

The apparent activation energy was higher for the Ti-75A (9.5 kcal/mole) and Ti-5-2.5(4.5 kcal/mole) alloy than for the Ti-8-1-1-alloy. In case of the Ti-8-1-1, two levels of stress intensity factors were used and the activation energy changed from 3.5 kcal/mole to 2.3 kcal/mole when K_i was raised from 38 ksi $\sqrt{in}$ to 45.5 ksi $\sqrt{in}$. It seems that an increase of mechanical components of fracture causes the temperature dependence to decrease. The comparison of activation energies for the various alloys was not particularly meaningful because different values of K_i were involved in the testing. SWE data associated with these tests showed the tendency for an increased number of stress waves with an increased crack velocity during the higher temperature tests.

IV DISCUSSION

A. General

In order to analyze the result and to link the information together, it seems advisable to indicate the major factors influencing SCC. Later on ideas about proposed mechanisms will be discussed, considering macroscopic and microscopic aspects. Summarizing the experimental results in a general way, the delayed failures on the SEN specimens involved short times because of relatively high crack velocities. There were two distinct fracture regions, a slow crack growth region and a fast one when mechanical instability occurred when the stress intensity factor reached K_{Crit}. In the slow crack growth region, the velocity was dependent on K_i and on temperature, but K_{Crit} was independent of the test conditions. There was also a change of fracture mode, from a brittle transgranular cleavage in the slow growth region to a dimpled mode in the mechanical instability region (typical of the fracture mode under "dry" conditions). Also found was evidence of a distinct crystallographic fracture process. Striations were found in the case of the Ti-8-1-1; the fracture planes were not necessarily associated with the slip planes. SWE activity corrolated with the crack propagation velocities and relatively low apparent activation energies were shown to be dependent on the K_i level.

Considering the discontinuous nature of the process, the transgranular mode of fracture following crystallographic habit planes, the role of mechanical parameters like K_i on the crack growth rate, particular attention to the mechanical aspects of the fracture process is warranted. Furthermore, it is believed that with alloys investigated, the chemical factors predominate in the nucleation stage of the microcracking and the

crack propagation is dominated by a mechanical driving force. Obviously, a well distinguished role of each of the factors, namely the chemical and mechanical factors is difficult to describe because of their interactions. It is clear that the stress field in the vicinity of the crack tip might affect crack nucleation. At the same time, the active environment could affect the surface energy so that the mechanical energy balance for crack instability would be altered. Purely chemical considerations could not account for the growth rates observed.

B. Mechanics Aspects

1. Energy Balance Considerations

The experimental result can be interpreted according to macromechanics concepts. A model can provide a qualitative explanation of the slow crack growth phenomena in a notched specimen subjected to a stress field and in a chemically active environment. Rice[28] in a general examination of the fracture mechanics energy balance equations, and Rice and Drucker[29] in an investigation on changes in stressed bodies due to void and crack growth, treated the mechanical aspects of SCC. Their treatments resulted in a general formulation of the Griffith fracture criteria in extended form in which elastic-plastic systems (small scale plastic zone) are included. Here, the fracture criteria considers the plastic energy dissipation due to deformation away from the crack surfaces as a separate term and not as part of the modified surface energy term in the Orowan-Irwin sense.

Two important points should be mentioned concerning the active environment problem. First the total potential energy of a stressed elastic body, U_p^a, is changed by creation of new traction free surfaces due to material removal, assuming the same load and displacement condition.

If we denote the potential energy after void or crack growth due to fracture of material removal, U_p^b, Rice's analysis shows,

$$U_p^a > U_p^b \tag{8}$$

which means that potential energy is released in a process which introduces an extension of discontinuities in the loaded segment. The important application from this energetical comparison will be that mechanical energy surplus is available and work can be done in formation of new surfaces. The usual energy balance equation in incremental form in an elastic body is actually not more than:

$$U_p^a - U_p^b = 2\gamma\,(A^a - A^b) \tag{9}$$

where γ is the modified surface energy and $A^a - A^b$ the incremental area extension. Until now the active environment released mechanical energy due to void or crack extension like in the case where dissolution process takes place and the effect of the active environment on γ was not considered. This leads to the second point. Obviously, a drastic change in γ can lead to fracture, the point being illustrated in Fig. 36A. This schematic figure is based on Rice's formulation for the energy balance equation in elastic-plastic material which has the form of:

$$G = \frac{\partial U_p}{\partial A} = p + 2\gamma \tag{10}$$

where G is the elastic strain energy release rate per unit crack extension and p the plastic energy dissipation rate, a term due to irreversible energy dissipated by plastic flow during a unit of crack propagation.

The plot shows the dependence of G and p on the applied load. If L^m is the critical load needed for instability in the "dry" material in order to balance γ_m, only L^e will be needed in the active medium which is a

lower load providing γ_m is changed to the lower value of γ_e in the active environment case. The assumption made is that the plastic flow behavior is not affected strongly by the environment. The dashed areas show the surplus energy which is increasing as the applied load is exceeding the value of L^e and approaching L^m.

Up to this point, the reasons for low stress intensity initiation of crack growth and the role of mechanical energy as a driving force for SCC have been considered. The approach for explaining the slow crack growth region will be similar to the one originated by Irwin[30] and discussed in detail by Krafft et al.,[31] for explaining pop-in mode compared to the stable slow crack propagation. Assuming the discontinuous nature of the SCC process as shown experimentally in this report, the idea of an unstable running crack due to corrosion and mechanical effects on one side and relaxation factors which will cause stress arrest on the other side should be considered. Figure 36B provides such a schematic explanation showing the energy rates G and R where R is the resistance energy term to crack propagation vs. crack length. G is actually originated by the applied stress which has a linear trace as shown in the figure. Normally, under "dry" conditions a specimen that will show a resistance curve as given in the figure due to geometry effects or more ductile behavior will become unstable at C_{Crit} which corresponds to the stress σ^m_{Crit} to fulfill this condition we need.

$$\frac{\partial G}{\partial A} = \frac{\partial R}{\partial A} \qquad (11)$$

In case of the environment the crack will become unstable at σ^e_{Crit} which is low due to the decrease of γ_m to γ_e but a small increment of the crack will cause the extended tip to be characterized by the R curve and time will be needed for the active medium to initiate the next step. Obviously

the size of the step in this discontinuous process will be dependent on the mechanical energy available and the duration of the slow crack growth process cannot exceed more than c_{Crit} where fracture will occur also without the corrosive environment. A similar approach was proposed by Coleman et al.[32] in SCC of steel and Mg-6% Al alloy assuming that the brittle fracture process is enhanced by the reduction of surface energy due to specific species adsorbed at the tip front. Still, the fracture process was considered to be mechanically controlled obeying the Stroh-Petch equation which relates the fracture stress and the grain size. This approach has also been considered for the liquid metal embrittlement process.[33]

In general, the macro-mechanics model that was described is not concerned with the specific micro-mechanism taking place although the adsorption model is a proposal along this line. It is hard to verify this model experimentally since determinations of γ and the changes in γ due to environment are difficult. Still the macro concept is descriptive and qualitatively explains the major events happening in the materials investigated in the present paper. Refinements are needed for the micro-mechanisms involved which may or may not necessarily be due to adsorption. This will be discussed further in a later section. It is important to mention that the fractographic observations in the Ti systems are consistent with the concept of having a strong mechanical component involved in the fracture process. That is, the existence of the cleavage mode and transgranular cracks with a crystallographic orientation, support the idea that basically brittle fracture is progressing in the usual sense but enhanced at a lower stress due to the environment.

2. Stress Intensity Parameters and Crack Velocity

The results shown in Figs. 18 and 19 for the crack growth rate dependency on K indicates that a universal behavior is not occurring. This

fact was realized by McEvily and Bond[3,34] and is very clearly emphasized in the present investigation. The relationship changes from material to material, and even in the same material characteristic regions in the curve can be noticed going from low K_i values toward instability. Using the function $\bar{V} = mK^n$, n is dependent on the stress intensity range and is initially low, about $n \approx 1$ or less for the Ti-5-2.5, Ti-13-11-3, and about $n = 4$ for the Ti-8-1-1. It is interesting to point out that the transition in the Ti-8-1-1-to high dependence of velocity with K occurs at values estimated as the plane strain fracture toughness values for this material keeping in mind that the specimens used are in the transition region between K_{IC} and K_C and catastrophic failure occurs at much higher values than K_{IC}. Consequently, the crack propagation rate cannot be described in the present case simply by the plastic zone size or the plastic strain at the tip of the crack which will yield a dependence on K^2. It is believed that in the initial portion of the curve, i.e. low K_i, the stage of nucleation sites for cracking is strongly affected by metallurigical factors as well as electrochemical factors. Here, the rate dependency on the stress intensity level is not controlled by the plastic zone characteristic. Later at high values of K_i nucleation sites can be changed by local mechanical instabilities, as in the case where K_{IC} is reached which cause strong dependency of the crack rate on K. A schematic plot illustrating this point from the mechanical point of view is given in Fig. 37. The low crack growth rate at low values of K is considered to result from a larger damaged zone (denoted as C^*_{Crit}) needed for mechanical instability. At the high values of K the critical zone needed is smaller and ΔC can exceed a few grains. The nucleation stage is considered to be much slower than the cracking at high velocity resulting from the cleavage process.

C. Metallurgical Considerations

As mentioned, the Ti-8-1-1 showed a higher dependency on K before reaching the mechanically dominated portion of the curve (characteristic fact for all the materials.) Comparing this alloy with the Ti-5-2.5 emphasized the different behavior in the latter where a very small dependence on K_i occurred. This is significant since the mechanical state described, for example by K_i/σ_y (where σ_y is the yield stress) is not less in the Ti-5-2.5. Considering the present interpretation of the experimental result, namely, that the active environment is triggering discontinuous brittle fracture, it is not difficult to visualize the role of metallurgical factors affecting the process kinetics. Williams[35] investigated the role of different compositions on susceptibility to SCC in Ti-systems with aqueous environment (3-1/2 % NaCl). He concluded that the α phase was susceptible, particularly in the alloys with higher Al content. When the content of 4-6 wt. % Al was reached, a sharp transition occurred from ductile to cleavage fracture. On the other hand the β-Ti showed ductile rupture not influenced by different heat treatments. Fager and Spurr[25] in similar systems investigated changes in SCC susceptibility due to the influence of microstructural features concluding also that the resistance of the materials to SCC was increasing as the percentage of β phase transformed to martensite increased in the alloy. Curtis and Spurr[36] in an extended study on the fracture behavior of Ti-6Al-4V and Ti-4Al-3Mo-1V in air and 3.5% NaCl aqueous solution, concentrated on the effects due to microconstituents formed by different heat.treatments. In addition to the information about the change of resistance to the SCC of the α and the β they reported that superior properties were achieved even by changing the α-Ti morphology in the structure from equiaxed α to acicular

morphology. In the present investigation the conclusion about significant differences in resistance to SCC for α-Ti to β-Ti was not confirmed. The electron fractography information did not indicate ductile zones that could be related to the β phase, or typical cracking arrest phenomena from secondary microcracks encountering the β phase. It is believed that either the small volume fraction and the small dispersion size of the β was not an appropriate system to clarify the above point, or the possibility that differences of susceptibility between the α and the β is relatively small. If the Ti-13-11-3 alloy can be taken as a base line for estimating susceptibility of the β phase, then the kinetics seem to be about two to three times slower than in the Ti-5-2.5. alloy. It could well happen that at higher stress intensity factors where the cleavage process in enhanced, the β phase is just failing in normal rupture due to load carrying capacity limitations. In such cases the fractograph would show the ductile mode associated with the dispersed β phase, and cracks would be seen in the α-Ti arrested at α/β interfaces. Fager and Spurr[25] studied also the case of precipitated α in the β matrix of the Ti-13-11-3 alloy. Observing the cracking nature in this structure leaves also the impression as the α is inhibiting cracking in a similar fashion as observed in the β dispersion in the α matrix. This might strengthen the argument that some critical size might be involved in the second phase before taking an active part in the cracking process. At the same time the finely dispersed second phase might slow the kinetics as total time to failure is dependent upon the length of the cleavage jumps and the reinitiation of failure from blunted cracks. In fact, the α/β interface might act as a deterrent to environmentally induced cleavage since the kinetics across the boundary may be interrupted. Thus, the cracking process may prefer to detour around small second phase particles whether they are α particles

in a β matrix or β particles in an α matrix. Referring back to the high crack growth rate dependency of Ti-8-1-1 on K_i, it is believed to result from metallurgical and mechanical origins. Williams and Blackburn[21,37] in their investigation on phase transformation of Ti-Al alloys and commercial Ti alloys indicated that there are three phase fields at low temperatures. The Ti-Al phase diagram proposed by Blackburn[21] showed the phases to be a disordered hcp α-solid solution on one side an ordered phase, α_2, near the Ti_3Al composition, and a two-phase region $\alpha + \alpha_2$. The ordered Ti_3Al has the DO_{19} type structure, which is hexagonal. It can be related to four unit cells of the disordered hexagonal phase by keeping the C parameter unchanged and by doubling the length of the a parameter. The formation of the $\alpha + \alpha_2$ phase region has been shown to start at about 8 wt. % Al (12 at.% Al) and that the size, dispersion, and the morphology of the α_2 is dependent upon the alloy composition and the heat treatment. Similar conclusion about the formation of α_2 was indicated by Crossley[38] while Ence and Margolin[39] proposed two intermetallic phases, the Ti_3Al and Ti_2Al as well. In the case of commercial alloys, the Ti-8-1-1 was found[40] to precipitate the α_2 phase and seems to be very near to the minimum Al content required for the formation of this ordered phase. For example, it has not been resolved whether or not Ti-6Al-4V contains α_2 and in the Ti-4Al-3Mo-1V Blackburn concluded that no α_2 phase was formed. In the present case, except for the Ti-8-1-1, none of the other alloys exceed the 5 wt.% Al content which probably isolated the Ti-8-1-1 in respect to the formation of the intermetallic compound.

Although it has not been conclusively established, the α_2 might also affect the dislocation structure. For example, Williams[35] has shown that coplanar dislocation arrangements may form confined to the Ti-8-1-1

slip plane in contrast to dense-tangled arrangements in alloys with aluminum content less than 5 wt%. In case of the Ti-8-1-1, therefore, two origins of enhancement of cleavage failure might be realized. First, the existence of the intermetallic phase, even in small dispersion size estimated about 200 Å, might serve as nucleation sites available for the active surface environment process to take place. Secondly, the coplanar dislocation arrangement can cause a large stress concentration which might raise the normal stress to a level high enough for cleavage. Lane and Cavallaro[41] attributed the SCC susceptibility of the Ti alloys in sea water mainly to the presence of the coherent Ti_3Al precipitate. This conclusion may be too general because relatively fast SCC of the Ti-5-2.5 and Ti-13-11-3 alloys occurs, although here the argumentation of Ti_3Al precipitation cannot be applied. However, the greater dependency of SCC kinetics on K in the Ti-8-1-1 may result from the Ti_3Al considerations. Two features were found on the fracture surfaces of the Ti-8-1-1 which were not noted in the other alloys. Figures 27A and 28 show striations occurring in the Ti-8-1-1 on the fracture surfaces. On the other hand, the striations visible in Fig. 27B appear like traces of a slip band. Striations are associated with the SCC process in many systems[42] and might support the idea of the discontinuous nature of the crack extension. The localized nature of the striation regions might indicate that the enhancement of the process results from higher kinetics of crack-slip reinitations. Between reinitiation points, a larger cleavage step would occur without any traces of the finely spaced striations.

D. Electrochemical Aspects

The work done by Beck[8,9] leaves no doubts about the significant role of the electro-chemical component in SCC process. The work was performed specifically on Ti-8-1-1 but many of the considerations seem to be generally applicable. The complexity of the possible electro-chemical processes taking place at the tip of the crack is well described in Beck's paper. Another complexity results from the very localized chemical activity just at the crack tip where the material-environment interaction is probably different than that far away from the crack tip. Without going into the nearly endless details of electrochemical models, there are some experimental facts which need to be mentioned. Beck[8] concluded in his investigation of Ti-8-1-1 that notched specimens were susceptible to SCC in chloride, bromide, and iodide solutions and immune of fluoride, hydroxide, sulfide, sulfate, nitride and perchlorate solutions. He also found that cathodic protection can prevent crack growth in NaCl aqueous solutions and that there is a linear relationship of the crack velocity to the applied potential in all the halide solutions. In addition, there is a temperature effect for crack growth rate in the Ti systems as was shown for the Ti-8-1-1[8] and in the present investigation for the same alloy as well as for the Ti-75A and the Ti-5-2.5 alloys. This evidence demonstrates that the electrochemical component is a necessary part of any model. Consequently a pure mechanical model describing the SCC in Ti-systems could hardly be accepted. At the same time, purely electrochemical models, are not sufficient to explain the phenomena. As mentioned before, the triggering description seems to combine some of the interactions taking place. Here, the electrochemical activity would be associated more with the initiation and reinitiation of

the discontinuous mechanical instabilities which are affected strongly by metallurgical factors.

E. Fracture Classification

Some additional remarks should be mentioned concerning the crystallographic nature of the SCC. The fact that the mode of fracture in the slow crack growth due to the active environment is transgranular and takes place on the normal cleavage planes, is probably one of the more important experimental facts. Blackburn[13] has shown that the crack orientation in the α phase corresponds to the planes nearly to the basal plane. The planes that were identified as $(10\bar{1}7)$ or $(10\bar{1}8)$ were found to be the cleavage planes observed in fracture under "dry" condition. A similar conclusion was reached by Meyn[44] investigating the Ti-7Al-2Cb -1Ta alloy. Here, also the plane of the cracks was identified as about $16^{\circ}\pm2^{\circ}$ to the basal plane.

The crystallographic nature of the cracks in the Ti-13-11-3 used in this investigation has already been discussed. The mode of fracture in the mechanical instability region (Region C in Fig. 13) was dimpled. Therefore the cleavage process (no dimples) had to be associated with the existence of the active environment. As shown by Meyn[45] in a notched specimen the fracture surface gradually changed from cleavage to cleavage/dimple mode as K increased. The dimpled zones were increased with K, reaching a completely dimpled rupture appearance when K_{Crit} was reached.

F. Mechanisms

In addition to the adsorption model that was already mentioned in relation to the proposed surface energy decrease, there are several other proposed mechanisms for SCC. First, there is the dissolution mechanism which is concerned with a preferential anodic attack taking place at the

crack tip. A different mechanism involves the formation of a brittle layer at the crack front, like an oxide layer or a brittle hydride layer. In case of the hydrogen effect, another alternative is considered, namely the diffusion of hydrogen in the plastic zone causing hydride precipitation and embrittlement. If we consider the data (Figs. 18 and 19) for the crack propagation rates in the present Ti alloys, these proposed mechanisms alone could not be applicable.

The experimental crack propagation rates are much too high to agree with a dissolution mechanism acting alone. For example, in the Ti-8-1-1 the experimental values for the crack propagation rate are about 5×10^{-3} in/sec without excessive polarization. Considering Faraday's Law for dissolution, the equivalent current density required to fit such a rate would be about 500 Ams/cm^2 which excludes the applicability of the dissolution mechanisms in this case. Beck[9] rejected also the oxide layer mechanisms due to kinetic considerations since the crack velocities are too high to allow the oxide film formation to keep up with the crack. Recently experimental information has been accumulated[43] to support the concepts of hydrogen embrittlement, but still more refinements are needed to explain the micro-mechanism involved. In the present Ti-alloys, if bulk diffusion of hydrogen is considered, the alternative of hydrogen diffusion control in the α phase seems to be too slow. For example, the diffusion coefficient D in α-Ti taken from extrapolated high temperature data of Papazoglou and Hepworth[46] is of the order of 10^{-13} cm^2/sec. at room temperature. Considering migration of hydrogen per unit time, a distance on the order of more than 10^{-6} in/sec results, which is too slow even for the Ti-75A in case the model assumes that essentially the high concentration of hydrogen has to be ahead of the crack tip. If we assume that in the α/β alloys, Ti-8-1-1 and Ti-5-2.5, the β-Ti controls hydrogen diffusion, the experimental

result by Holman et al[47] for diffusion in β-Ti is appropriate. Here D is of the order of 5×10^{-7} cm^2/sec at room temperature which gives a hydrogen migration of about 10^{-4} in/sec. This is substantially closer to observed rates of crack propagation particularly if enhancement by plastic deformation is considered.

It has to be mentioned that the discontinuous nature of the process as shown to occur by the SWE results can be explained by purely electrochemical arguments if the concepts of passivity and passivity breakdown is introduced. The breakdown can be attributed either to chemical factors or to the stress in what is called the "Film Rupture" concept. Nevertheless the high kinetics, particularly in the high K_i range suggest that the combined (mechanical-chemical) mechanism is operating. Furthermore, the observed discontinuous crack growth process does not exclude any of the previously described mechanisms. If the process is assisted strongly by the mechanical energy, the crack propagation rate should be expected to be higher than that predicted by electrochemical models alone. Thus the prediction of slow kinetics by theory actually supports the triggering concept. Referring to the apparent activation energies as given in Fig. 35 a thermodynamic approach used for combined temperature and stress controlled rate process can be applied. The activation energy when K_i is increased was shown in the Ti-8-1-1.

Bartenov and Razumovskaya[48] used the rate process concept in the case of glass. In a similar way the approach was previously applied to SCC in amorphous elastic solids by Hillig and Charles.[49]

Helfrich[50] also approached the SCC problem as a thermally activated process where the rate of activation is dependent on the stress state. The system used was Al-4.2Zn-2.5Mg alloy in aqueous NaCl solution. In

the present Ti alloys, the temperature dependence also suggests a formulation by a rate equation. On the other hand, the small dependence on temperature (or the low apparent activation energy) supports a stress dependent term in the equation.

Consider a discontinuous mechanism where Δt_j is the total time for discontinuous jump step, Δt is the time to trigger and ℓ_j is the distance of the jump. Consider also that ρ_s is the distance between active sites associated with the primarily chemical process which operates before a cleavage step occurs.

The rate equation is of the form:

$$V = v_o \exp(-H/RT) \tag{12}$$

where v_o is the preexponential kinetic factor which depends on the system chemically and mechanically and H is the apparent activation energy for SCC. Essential v_o include the appropriate vibrational frequency and a modified distance which depends on the jump distance ℓ_j. Assume that diffusion of an embrittling element in the titanium is controlling the cracking initiation: ρ_s can be estimated by

$$\rho_s \approx [D_s \quad \Delta t_s]^{1/2} \tag{13}$$

where, D_s = diffusion coefficient of the embrittling species in titanium. Since $\Delta t_s \approx \Delta t_j$ the crack rate can be estimated as following:

$$\frac{da}{dt} \approx \frac{\ell_j}{\Delta t_j} \tag{14}$$

$$\frac{\ell_j}{\Delta t_j} = \frac{\ell_j D_s}{\rho_s^2} = \frac{\ell_j D_s \exp - \{H^* - f_1(U_p)\}}{\rho_s^2} \tag{15}$$

where H^* = activation energy for diffusion in Ti; $f_1(U_p)$ = a mechanical function dependent on the state of stress and specimen geometry, and U_p = potential energy of the loaded specimen.

If N_s are the numbers of active sites along a grain front of size d;

$$\rho_s = \frac{d}{N_s} \tag{16}$$

N_s is dependent on chemical factors as well as on mechanical factors. Dispersion of a second phase or active site due to coarse slip bands might reduce ρ_s so that a relatively small distance of migration at the crack front could cause a cleavage jump.

If N_s can be expressed in the form;

$$N_s = n_s \exp\left(f_2(U_p)/RT\right) \tag{17}$$

where $f_2(U_p)$ = a different mechanical function dependent on the mechanical energy. Equation (15) for the average crack propagation rate can be written:

$$\bar{v} = \frac{\ell_j\, n_s^2\, D_o \exp - \{H^* - F(U_p)\}/RT}{d^2} \tag{18}$$

where $F(U_p) = f_1(U_p) + 2f_2(U_p)$. Comparing to equation (12)

$$H = H^* - F(U_p) \tag{19}$$

The function $F(U_p)$ can be expressed by K the stress intensity factor or G the strain energy release rate, since G, $(G=K^2/E)$ multiply by the effective surface area A_s gives the potential energy U_p. A_s the activation surface has an equivalent meaning to the activation volume term in case where the mechanical term in the rate equation is a stress function. It is now appropriate to reconsider SCC in the Ti-8-1-1 and the Ti-5-2.5 alloys. Assuming hydrogen diffusion in the β phase is controlling

and that the diffusion coefficient in the α/β structure is similar to the Ti-13-11-3[47] $D_\beta = 0.245\ 10^{-3} \exp(-5140/RT)\ in^2/sec$. The apparent activation energy for the Ti-8-1-1 was 3.5 kcal/mole and 2.3 kcal/mole for an applied stress intensity factor of 38×10^3 psi $\sqrt{in}$ and 45.5×10^3 psi $\sqrt{in}$, respectively. For the Ti-5-2.5 alloy the apparent activation energy was 4.5 kcal/mole, for a K_i of 93×10^3 psi $\sqrt{in}$. The SWE results show that ℓ_j for the Ti-8-1-1 was less then that for Ti-5-2.5 even though d is about 10^{-3} in. in both. Utilizing these and taking $F(U_p)$ to be $A_s G$ result A_s and n_s to be higher values for the Ti-8-1-1 than for the Ti-5-2.5 alloy in order to satisfy the crack propagation rate data given in Figs. 18 and 19. The higher values for the activation surface and n_s which is related to the active site, might be attributed to the existing ordered α_2 phase in the Ti-8-1-1 already discussed.

Two important points can be deduced from the above diffusion controlled mechanism. First the rapid kinetics of the process can be explained by the combined chemical and mechanical model. Secondly, the acoustic emission technique can provide information on two major values the incremental jump ℓ_j and the interval between jumps associated with Δt_s. In general, the SWE data support the discontinuous mechanism in the present investigation. The increase of amplitude and frequency of the stress wave with the stress intensity factor suggest that the higher velocities at high K_i level results from two origins, enhanced crack initiations and larger jump distances due to the higher mechanical energy.

V. CONCLUSIONS

(a) In the case of pre-cracked specimens, commerically-pure Ti-75A as well as alpha-beta Ti-8-1-1 and Ti-5-2.5; and all beta Ti-13-11-3 alloys are susceptible to SCC in an aqueous 3-1/2% NaCl soultion.

(b) Crack propagation rates for SCC were determined as a function of applied stress intensity factor (K_i) using tapered crackline-loaded specimens. The stress intensity factor was controlled only by the applied load since K is independent of crack length.

(c) Crack propagation rates in the slow crack growth region (below the transition to a strong mechanically dominated region) were on the order of 0.001 in/sec.

(d) As opposed to observations in other SCC processes, dc/dt was not proportional to K_i^2. The K_i exponent varies in the range of about 1 to 8.

(e) Ti-8-1-1 exhibited stronger dependency of crack propagation rate an K_i than the other materials. K_i needed to stimulate SCC was low ($K_i/K_{Crit} = 0.32$) even though the mechanical state described by K_{ISCC}/σ_y was the lowest ($K_{ISCC}/\sigma_y = 0.160$). This was interpreted in terms of metallurgical factors as the dispersion of the α_2 phase in the structure.

(f) Catastrophic failure in notched specimens followed slow crack growth with the transition occurring at the critical stress intensity factors.

(g) The establishment of the crack propagation rate as a function of K_i allowed estimates of the total time to failure for notched specimen regardless of specimen geometry.

(h) The acoustic emission techniques was applied to the study of SCC in titanium alloy systems. This showed that the stress-corrosion cracking was discontinous emphasizing that the mechanical component in the phenomena was significant. It also suggested a method for measuring to discontinous crack jumps and the time between them.

(i) A correlation between crack propagation rates and SWE/sec was established. High crack velocities were associated with frequent stress wave activity and an increase in wave amplitude.

(j) The fracture mode in the SCC fracture region was found to be transgranular cleavage for all the materials, in contrast to ductile rupture (dimpled mode) in specimen tested in air.

(k) SCC in the all beta Ti-13-11-3 alloy was found to be crystallographic cleavage in the {100} planes.

(l) Crack growth rates at different test temperature established that the SCC process was thermally activated in all cases. The apparent activation energies were 9.5 kcal/mole for the Ti-75A; 3 kcal/mole for the Ti-8-1-1 and 4.5 kcal/mole for the Ti-5-2.5 alloy. In the case of the Ti-8-1-1 an increase in K_i of about 8×10^3 psi $\sqrt{\text{in}}$ reduced the apparent activation energy from 3.5 to 2.3 kcal/mole.

(m) A combined chemical and mechanical mechanism for discontinous cracking was proposed which allows for the relatively rapid crack propagation rates observed. A diffusion controlled mechanism of hydrogen in the β-phase is hypothesized as a possible crack initiation mechanism. The stress intensity contribution is to effect either the number of activated sites for the chemical reaction, the mechanical driving force for crack initiation or the discontinous crack step.

APPENDIX I

CRACKLINE-LOADED EDGE CRACK SPECIMEN (TAPERED BOUNDARIES)

The determination of K or G in an elastic notched specimen follows two approaches. One is a fundamental procedure namely by analyzing the stress field in the vicinity of the crack tip, where a mathematical relationship for K is determined. The other approach developed by Irwin and Kies[51] is not concerned with the detailed description of the stress field but relates the strain energy release rate G with the total change of the elastic compliance of the specimen during crack propagation, specifically:

$$G = \frac{P^2}{2B}\left(\frac{d\lambda}{dc}\right) \qquad \text{(A-1)}$$

where P is the applied load, B is the specimen thickness, c is the crack length and λ is the compliance defined as the specimen extension per unit load. Alternatively in terms of the stress intensity factor, K, for plane strain;

$$\frac{2K^2(1-V)^2\ WB^2}{P^2} = \frac{d(E\lambda B)}{d\left(c/W\right)} \qquad \text{(A-2)}$$

Here V and E are Poissons ratio and Young's modulus respectively, and W is the specimen width.

Considering a fixed specimen geometry, the right hand side of equation (A-2) is dominated by the functional relationship between λ and the crack length c. Mostovoy, Crosley and Ripling[17] derived the equation for λ in the case of a crackline loaded edge crack specimen using the beam theory. Looking for a linear function for λ they suggested that a particular shaping of the crackline loaded edge crack specimen can provide a reasonable linear estimation for the λ function (Fig. 38B). This being the case, K then depends only on P and not on c. Srawley and Gross[32] studied analytically this specimen geometry in a broad parametric way utilizing a

boundary collocation procedure making use of Williams[53] stress function. Their analysis emphaiszed that the normal free boundary has to be far enough from the crack tip, otherwise the stress field is dominated by this boundary. In such a case K values will increase in a monotonic way as c increases.

Preliminary studies were done on this specimen type before utilizing it for SCC studies. The geometry ($H/e = 0.4$) and dimensions are given in Fig. 4. Most of the experimental work was done on brittle polymers in order to confirm the specimen dimensions and to determine calibration curves. The arguments for using polymer specimens are given elsewhere.[54] Figures 39 and 40 show the photoelastic pattern for two differently applied K_i values and 3 different crack lengths with c/W ranging from 0.2 to 0.4. The similarity of the stress field close to the crack tip can be seen which was observed in the range of K_i/K_{IC} from 0.2 to 0.6. Figure 38A shows that the critical load for instability in the polycarbonate occurred almost at constant load values up to $c/W = 0.4$. Since $c/W = 0.4$ appeared to be a limiting value, it was concluded that for the SCC investigation the measured range should not exceed $c/W = 0.3$.

Figure 41 demonstrates the use of the specimen for the Ti-2.5-5 alloy for several levels of K_i controlled only by the applied load. The crack extension increment at each K_i was long enough for the velocity determination. Figure 42 gives the calibration curve for the crack opening displacement gage instrumented to the tapered specimen. The data is plotted in the dimensional form, namely EBV/P vs. c/W where V is the surface displacement at the crack edge (see Fig. 3).

APPENDIX II

CRACK PROPAGATION RATES AND TOTAL TIME-TO-FAILURE IN NOTCHED SPECIMENS

Many investigations of SCC include values concerning the total time to failure. Obviously such information is restricted in the general case since the time-to-failure is dependent on the particular specimen geometry used. Crack propagation rates as a function of the applied stress intensity factor (K_i) provide more fundamental information. In a notched specimen, K normally increases as the crack extends and the functional form of K vs. crack length is usually obtainable. This provides calculations of time-to-failure (t_f) from the velocity function. It has been shown in this report that K_{Crit} is not dependent on K_i (Figs. 14 and 15).

Consider a notched specimen where K is given for a fixed W (specimen width)

$$K = F(c) \tag{B-1}$$

Assume that experimentally the crack propagation rate is determined

$$dc/dt = f(K) \tag{B-2}$$

thus t_f can be obtained from the following expression

$$t_f = \int_{K_i}^{K_{Crit}} \frac{(dc/dK)\, dK}{f(K)} \tag{B-3}$$

Practically it is more convenient to consider the crack length as a parameter since this is directly measurable. Consequently, if the crack propagation rate function is given

$$dc/dt = mK^n \tag{B-4}$$

and $K = \sigma c^{1/2} \psi\ (c,W)$ where σ is the applied stress and $\psi\ (c,W)$ a correction function for the specimen finite width, then

$$t_f = \frac{1}{m\sigma^n} \int_{c_i}^{c_{Crit}} \frac{dc}{c^{n/2}\,[\psi(c,W)]^n} \qquad \text{(B-6)}$$

For the SEN specimen, $\psi(c,W)$ can be expressed in a polynomial form[18] or in a trigonometrical form.[26]

Estimations of t_f in the case of Ti-8-1-1 and Ti-5-2.5 can be demonstrated. These two alloys have different dc/dt characteristics. The Ti-8-1-1 was strongly dependent upon K_i, where the value of the exponent is n = 4. Considering the SEN specimen (Fig. 3) where W = 3 in. and the initial crack length, c_i, was about 0.600 in., the correction function for the finite width was estimated by the relationship;

$$\psi(c) = 3.4c^{1/2} \qquad \text{(B-7)}$$

using equation (B-6), t_f can be estimated by

$$t_f = \frac{1}{3m'\,\sigma^4} \left(\frac{1}{c_i^{\,3}} - \frac{1}{c_{Crit}^{\,3}} \right) \qquad \text{(B-8)}$$

where $m' = 3.4^4 \times 10^{-21}$. The following table gives a comparison of the results obtained using equation B-8 with those obtained experimentally:

K_i/K_{Crit}	t_f - calculated (sec)	t_f experimental (sec)
0.33	308	135
0.46	88	100
0.85	9.1	13

In the case of Ti-5-2.5 alloy the crack propagation rate showed small dependence on K_i before reaching the mechanically dominated region (Fig. 19).

The estimation of t_f, an average velocity is assumed on equivalently n=0. Since

$$c_{Crit} = c_i + t_f v \qquad \text{(B-9)}$$

in the case where v=const, c_{Crit} should have a linear dependence with t_f. Figure 43 illustrates this behavior for the Ti-5-2.5 alloy.

Consequently, t_f for v=const, can be formulated, by

$$t_f = \left[\frac{1}{(K_i/K_{Crit})^2} \left(\frac{\psi(c_i)}{\psi(c_{Crit})} \right) - 1 \right] \frac{c_i}{\bar{v}} \qquad \text{(B-10)}$$

The vaules of $\psi(c)$ are obtained from equation (5). The following table gives a comparison of the results obtained by using equation B-10, with those obtained experimentally where $c_i = 0.60$ in and $\bar{v} = 1.7\times10^{-3}$ in/sec

K_i/K_{Crit}	t_f calculated (min)	t_f experimental (min)
0.40	5.50	4.57
0.57	2.92	3.00
0.74	0.97	1.10

Figure (43) illustreates schematically the variations in the t_f curve vs. K_i/K_{Crit} for different crack rate dependencies on K_i.

ACKNOWLEDGEMENT

The author wishes to express his appreciation to Professor Earl Parker, Professor Victor F. Zackay and Mr. William W. Gerberich for advice and encouragement. Thanks are due also to the staff of the Inorganic Materials Research Division of the Lawrence Radiation Laboratory for their support and services. In particular the author wishes to mention Mr. D. Wixson and Mr. G. Georgakopoulos.

The assistance of Dr. D. Porter and Mr. P. Guest during the present investigation is also acknowledged. The assistance of G. Pelatowski (preparation of line drawings) and J. Ball (preparation of manuscript) is well appreciated.

This work was carried out under the auspices of the United States Atomic Energy Commission through the Inorganic Materials Research Division of the Lawrence Radiation Laboratory.

REFERENCES

1. G. R. Irwin, Fracture Mechanics in Structural Mechanics, Pergamon Press, London, p. 557 (1960).

2. G. R. Irwin and A. H. Wells, A Continuum - Mechanics View of Crack Propagation, Met. Rev. 10, 38 (1965).

3. A. J. McEvily and A. P. Bond, J. Electrochem. Soc., 112. p. 131 (1965)

4. R. G. Weber and A. J. McEvily, The Stress Corrosion Cracking of a Non-Age-Hardenable Al-Alloy, 2nd International Conf., Brighton, England (1969).

5. H. H. Johnson and A. M. Willner, Applied Materials Research, Jan. (1965).

6. G. C. Kiefer and W. W. Harple, Metal Progress, p. 74, Feb. (1953).

7. B. F. Brown, Materials Research and Standards, 6, No. 3., p. 129 (1966).

8. T. R. Beck, SCC of Titanium Alloys, J. Electrochem. Soc. June p. 551, (1967).

9. T. R. Beck, SCC of Titanium Alloys, J. Electrochem. Soc., Sept. p. 890, (1968).

10. T. P. Hoar and C. J. L. Booker, The Electrochemistry of the Stress Corrosion Cracking of α-Brass-Corrosion Science, 5, p. 821, (1965).

11. J. M. West, Electrodeposition and Corrosion Processes, Chapter 7 D. Van Nostrand Co., London, (1965).

12. H. H. Uhlig, Effects of Microstructure on Corrosion, Trans. ASM 46A, p. 189, (1954).

13. E. N. Pugh, Environment, Sensitive Mechanical Behavior, Eds. A.R.C. Westwood and J. S. Stoloff, AIME, 35, p. 351, Gordon and Breach, Co. (1966).

14. G. Sanderson, and J. C. Scully, Observations on the Stress Corrosion Cracking of Ti Alloys, Environment Sensitive Mechanical Behavior, Eds. A.R.C. Westwood and N. S. Stoleff, AIME 35, p. 511, Gordon and Breach (1966).

15. H. H. Uhlig, New Perspectives in the Stress Corrosion Problem, Physical Metallurgy of Stress Corrosion, Spectral, AIME, 4, Ed. T. N. Rhodin, p. 1, Interscience Publ., N.Y. (1959).

16. M. T. Manjoine, J. of Basic Eng., ASME, p. 293 June (1965).

17. S. Mostovoy, P. B. Crosley and E. J. Ripling, J. of Materials, 2, No. 3, p. 661 (1967).

18. W. F. Brown and J. E. Srawley, Plane Strain Crack Toughness Testing Of High Strength Metallic Materials, ASTM STP, 410, p. 15, (1966).

19. W. W. Gerberich and C. E. Hartbower, Same Observations and Stress Wave Emission as a Measure of Crack Growth, Inter. Journ. of Frac. Mech., 3, No. 3, p. 185 (1967).

20. S. Mostovay, and E. J. Ripling, Fracture Toughness of an Epoxy System, Journ. of Applied Polymer Sci., 10, p. 1351 (1966).

21. M. J. Blackburn, the Ordering Transformation in Ti-Al Alloys, containing up to 25 at. pct. Al, Trans. AIME, 239 p. 1200 (1967).

22. H. H. Hausner, editor, Modern Materials, Chapter on Titanium, Metallurgy Academic Press, N.Y., p. 225. (1960).

23. A. D. McQuillan and M. K. Quillian, Titanium, Chapt. 7, p. 158 Butterworths Scientific Publ., London (1956).

24. A. M. Sullivan, Velocity of Cracks Extending Under Stress in an Adverse Environment, 2nd International Conf., Brighton, England, p. 33, (1969).

25. D. N. Fager and W. F. Spurr, Some Characteristics of Aqueous Stress Corrosion in Ti Alloys, Trans ASM, 61, p. 283, (1968).

26. W. W. Gerberich and Y. Katz, On a Trigonometric Expression for the SEN Case, to be published in J. of Eng. Fract. Mechanics.

27. W. W. Gerberich, Fracture in Metal Metal Composites, presented at Composite-Materials, Fundamentals and Utilization, U.C. Berkeley June (1968).

28. J. R. Rice, An Examination of the Fracture Mechanics Energy Balance From the Point of View of Continuum Mechanics, International Conf. on Fract. Sendai, Japan, Vol. 1 Chapter A., p. 269, (1965).

29. J. R. Rice and D. C. Brucker, Energy Changes in Stressed Bodies due to Void and Crack Growth, International Journal of Fracture Mechanics 3, No. 1, p. 19, (1967).

30. G. R. Irwin, Fracture Testing of High Strength Sheet Materials Under Conditions Appropriate for Stress Analysis, Report 5486 U.S. Naval Research Lab. July (1960).

31. J. M. Krafft, A. M. Sullivan and R. E. Boyle, Effect of Dimension Fast Fracture Instability of Notched Sheets, Proceedings, Crack Propagation Symposium, College of Aeronautics Cranfield, England 1, p. 8, (1961).

32. E. G. Coleman, D. Weinstein and W. Rostoker, On a Surface Energy Mechanism for SCC, Acta Met., 9, p. 491, (1961).

33. H. Nichols and W. Rostoker, Acta Met., 9, p. 504, (1961).

34. A. J. McEvily and A. P. Bond, Environment Sensitive Mechanical Behavior, AIME, 35, p. 421, Gordon and Beach, Eds. A.R.C. Westwood and N.S. Stoloff, (1966).

35. J. C. Williams, Some Observations on the SCC of the Three Commerical Ti Alloys, Trans. ASM, 60, p. 646, (1967).

36. R. E. Curtis and W. F. Spurr, Effect of Microstructure on the Fracture Properties of Ti-Alloys in Air and Salt Solution, Trans. ASM 61, p. 115, (1968).

37. J. C. Williams and M. J. Blackburn, A Comparison of Phase Transformation in Three Commerical Ti-Alloys, Trans. ASM, 60, p. 373, (1967).

38. F. A. Crossley, Titanium, Rich End of the Ti-Al Equilibrium Diagram, Trans. AIME., p. 1174, (1966).

39. E. Ence and H. Margolin, Phase Relations in the Titanium-Aluminum System, Trans. AIME, 221, p. 151, (1961).

40. M. J. Blackburn, Relationship of Microstructure to Some Mechanical Properties of Ti-8Al-1Mo-1V, Trans. ASM, 59, p. 694, (1966).

41. I. R. Lane and J. L. Cavallaro, Metallurgical and Mechanical Aspects of Sea Water Stress Corrosion of Ti, Application Related Phenomena in Ti-Alloys, ASTM, STP, 432, p. 147, (1968).

42. E. J. Pugh, J. A. S. Green and P. W. Slattery, On the Propagation of SCC in a Mg-Al Alloy, Second International Fracture Conf., Brighton England (1969).

43. D. T. Powell and J. C. Scully, Stress Corrosion Cracking of α-Ti Alloys at Room Temperature, Corrosion, NACE, 24, No. 6, p. 151 (1968).

44. Marine Corrosion Studies, Naval Research Lab. NRL 1634 ed. T. J. Lennox, July(1965).

45. D. A. Meyn, Corrosion Sci., 7, p. 721, (1967).

46. T. P. Papazogeou and M. T. Hepworth, The Diffusion of Hydrogen in Ti, Trans. of the AIME,, 242, p. 682, (1968).

47. W. R. Holman, R. W. Crawford, and F. Paredes, Jr., Hydrogen Diffusion in a β-Ti Alloy, Trans, of the AIME., 233, p. 1836, (1965).

48. G. M. Bartenev and I. V. Razumovskaya, The Theory of Time Dependent Strength of Solids in Surface Active Media, International Conference on Fracture, Sendai, Japan, 3, E-3, (1965).

49. W. B. Hillig and E. J. Charles, Surfaces, Stress Dependent Surface Reactions, and Strength, High Strength Materials, ed. V. F. Zackay John Wiley and Sons Inc., N.Y., p. 682 (1965).

50. W. T. Helfrich, Influence of Stress and Temperature an Short-Transverse SCC of an A-4.2 Zn2.5 Mg Alloy, Stress Corrosion Testing STP425 ASTM, p. 21 (1967).

51. G. R. Irwin and T. A. Kies, Critical Energy Rate Analysis of Fracture Strength, Weld. Journal 33, (4) p. 1935, (1954).

52. J. E. Srawley and G. Gross, Stress Intensity Factors for Crackline Loaded Edge-Crack Specimens, Materials Research and Standards, 7, No. 4., p. 155 (1967).

53. M. L. Williams, On the Stress Distribution at the Base of a Stationary Crack, Journal of Applied Mechanics, No. 24, p. 109 (1957).

54. Y. Katz, P. L. Key and E. R. Parker, Dimensionless Fracture Toughness Parameters, Trans. ASME, 10, Series D., p. 662 (1968).

FIGURE CAPTIONS

Fig. 1. (A) Set-up for environmental testing of SEN specimens showing C.O.D. gage and piezoelectric transducer.

(b) Set-up for environmental testing of tapered specimens at different temperatures. Instrumentation like in (A).

Fig. 2. Dimensions of the crackline-loaded specimen for fracture toughness determination in air.

Fig. 3. Single-edge-notch specimen and description of the C.O.D. gage.

Fig. 4. Tapered crackline-loaded specimen for crack velocity determination.

Fig. 5. Schematic of the acoustic emission set-up.

Fig. 6. Light micrograph of (A) Ti-75A commerically pure, (B) α/β Ti-8-1-1 (C) α/β Ti-5-2.5 and (D) all β Ti-13-11-3.

Fig. 7. (A) Ti-8-1-1 current projection taken on the microprobe analyser

(B) microstructural morphology of the same area

(c) line profile (shown in B) along α/β boundaries taken on the microprobe analyser.

Fig. 8. Room temperature tensile behavior of the Ti-75A and Ti-8-1-1 alloys at the cross head speed of 0.08 in/sec.

Fig. 9. Room temperature tensile behavior of the Ti-5-2.5 and Ti-13-11-3 alloys at a cross head speed of 0.08 in./sec.

Fig 10 Electron fractographs for Ti-75A showing fracture regions of a precracked SEN specimen failed under environmental conditions (A) prefatigued region (B) slow crack growth (C) catastrophic mechanical failure.

Fig 11. Electron fractographs of a Ti-8-1-1 and SEN specimen fractured under environmental conditions.

Fig 12. Electron fractographs of a Ti-5-2.5 SEN specimen fractured under environmental conditions.

Fig.13. Electron fractographs of a Ti-13-11-3 SEN specimen fractured under environmental conditions.

Fig.14. Mechanical instability behavior in SEN specimens fractured under environmental conditions for Ti-75A and Ti-8-1-1 $\left(f(c) = 2[\sin^2 (c\pi/W) + \sin^2 (c\pi/W)]\right)$

Fig 15. Mechanical instability behavior in SEN specimens fractured under environmental conditions for Ti-5-2.5 and Ti-13-11-3.

Fig.16. Total time to failure for Ti-75A and Ti-8-1-1 SEN specimens (see Fig. 3).

Fig.17 Total time to failure for Ti-5-2.5 and Ti-13-11-3 SEN specimens.

Fig.18. Crack propagation rate dependence on applied stress intensity factor (K_i) for Ti-75A and Ti-8-1-1 alloys.

Fig 19. Crack propagation rate dependence on K_i for Ti-5-2.5 and Ti-13-11-3 alloys.

Fig 20. Stress wave emission activity and C.O.D. gage output as a function of SCC slow crack growth in Ti-75A.

Fig 21. (A) Stress wave emission activity for the Ti-8-1-1 approaching mechanical instability (from bottom to the top) (B) Same for Ti-5-2.5 alloy (C) Same for Ti-13-11-3. Time range about 3 sec before catastrophic failure occurred.

Fig 22. Stress wave activity for Ti-75A and Ti-8-1-1 alloys during SCC slow crack growth.

Fig 23. Stress wave activity for Ti-5-2.5 and Ti-13-11-3 alloys during SCC slow crack growth.

Fig.24. (A) Scanning electron fractograph for SCC cleavage in Ti-75A (B) Scanning electron fractograph at higher magnification compared

to (C) electron fractograph using a two-step replication technique.

Fig. 25 (A) Light micrograph of transgranular fracture in Ti-75A under environmental conditions (B) Light micrograph showing major crack and secondary cracks in Ti-8-1-1 under environmental conditions.

Fig 26. (A) Light micrograph of transgranular fracture in Ti-5-2.5 alloy under environmental conditions.

Fig. 27 (A) Electron fractograph of Ti-8-1-1 showing SCC striations. (B) Electron fractograph of Ti-8-1-1 failed under environmental condition indicating possible slip traces.

Fig 28. (A) Fractographic evidence of localized striations on Ti-8-1-1 SCC fracture surface. (B) Very finely spaced striations taken from same fracture surface.

Fig 29. (A) Secondary cracks in Ti-13-11-3 with crystallographic nature light micrograph (B) same specimen with fracture planes at 90°- light micrograph.

Fig 30. (A) Fracture path change at grain boundary in Ti-13-11-3, light micrograph, (B) Scanning electron fractograph showing fracture path change at a grain boundary. Same material.

Fig.31. Scanning electron fractograph of (A) transgranular cleavage in Ti-13-11-3, (B) Cheveron traces orientated to the crack direction; (see Fig. 13B), same material.

Fig 32. Scanning electron fractograph of (A) transgranular cleavage (B) crystallographic cracking in Ti-13-11-3.

Fig 33. Relationship between cracks and slip orientations in Ti-13-11-3 cracks are not oriented on slip planes. Light micrograph.

Fig 34. Single surface trace analysis on angles between cracks shown schematically on the (001) stereographic projection, see Table III.

Fig 35. Temperature dependence of crack propagation rates in Ti-75A, Ti-8-1-1 and Ti-5-2.5 alloys.

Fig 36. (A) Schematic plot illustrating mechanical surplus energy released in case of active environmental failure. (B) Schematic plot illustrating slow crack growth region as a result of active environmental conditions.

Fig 37. Schematic illustrations of chemical crack initiation, mechanical crack extension and crack arrest in (a) low K_i (b) high K_i.

Fig 38. (A) Load-displacement curves for polycarbonate-tapered specimens (specimens as in Fig. 4). (B) Ti-75 tapered specimen failed under environmental conditions.

Fig 39. Isochromatic pattern from 0.25 in. thick, tapered polycarbonate, specimens obtained with a circular polarization and quarterwave plate set-up. Loading condition:

$$K_i/K_{IC} = 0.2$$

(A) c/W = 0.2 (B) c/W = 0.3 (C) c/W = 0.4.

Fig 40. Similar to Fig. 39 with loading condition $K_i/K_{IC} = 0.5$.

Fig.41. Loading vs. C.O.D. signal as recorded for velocity measurement of Ti-5-2.5 alloy.

Fig 42. Calibration curve for C.O.D. gage for the tapered specimen gage was fixed as shown in Fig.1.

Fig 43 Top crack length variation at fracture for different initial conditions c_i was about 0.600 in bottom -- schematic plot relating total time to failure and crack rate dependency on K_i.

TABLE I.

Material	Composition											
	C	Fe	N	Al	V	Sn	Cr	Mo	Mn	H	O_2	Ti
Ti-75A(unalloyed)	0.023	0.11	0.011							0.004	0.33	Bal.
Ti-8Al-1Mo-1V	0.021	0.06	0.010	7.9	1.0			1.0		0.007	0.09	Bal.
Ti-5Al-2.5Sn	0.023	0.37	0.014	5.1		2.5			0.002	0.005	0.17	Bal.
Ti-13V-11Cr-3Al	0.016	0.16	0.026	3.1	13.6		10.8			0.010	0.14	Bal.

TABLE II

	Engineering Tensile Data*					Fracture Toughness Data**		
	σy psi 0.2% offset	σu psi	elong. %	area reduc. %	E psi×10^{-6}	K_{IC} ×10^{-3} psi $\sqrt{in}$	K_{Crit} ×10^{-3} psi$\sqrt{in}$	Remarks
Ti-75A	70,000	85,000	24	52.6	16.6	57.4	115	K_{IC}-instability from SWE data
Ti-8-1-1	150,000	160,000	15	30	18.1	55.5	-	catastrophic failure
Ti-5-2.5	126,000	134,000	16.5	45	16.7	--	125	no wave activity before failure
Ti-13-11-3	136,000	136,000	15.0	36.5	15.8	72	147	K_{IC} instability from SWE data

* 2" gage length

** On compact crack line loaded specimen 2.5"×3" t = 0.125

TABLE III

Grain	θ_1°	θ_2°	Remarks
1	43	67	
2	32	78	$\theta_3 = 180 - (\theta_1 + \theta_2)$
3	80	53	
4	52	71	For the case of $\theta_1 \sim 90$
5	83	39	see Figure 29B.
6	76	68	
7	58	70	
8	60	65	
9	78	40	
10	~90	~90	

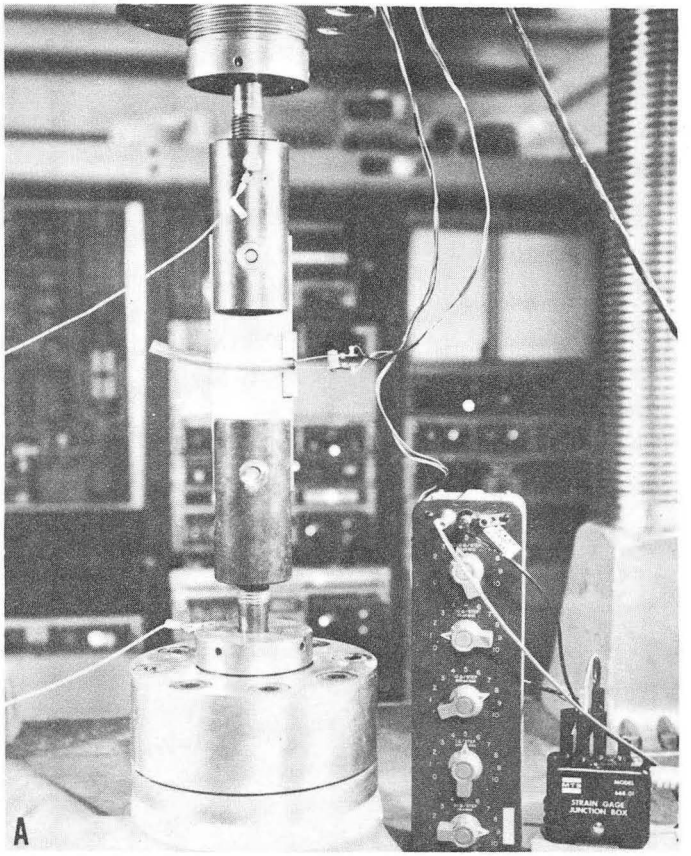

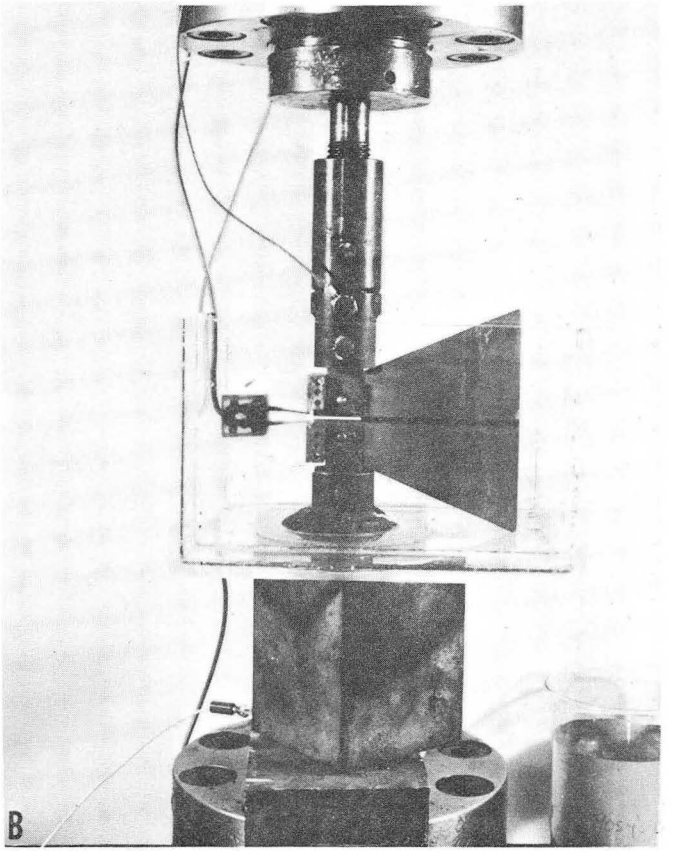

XBB 696-3551

Figure 1

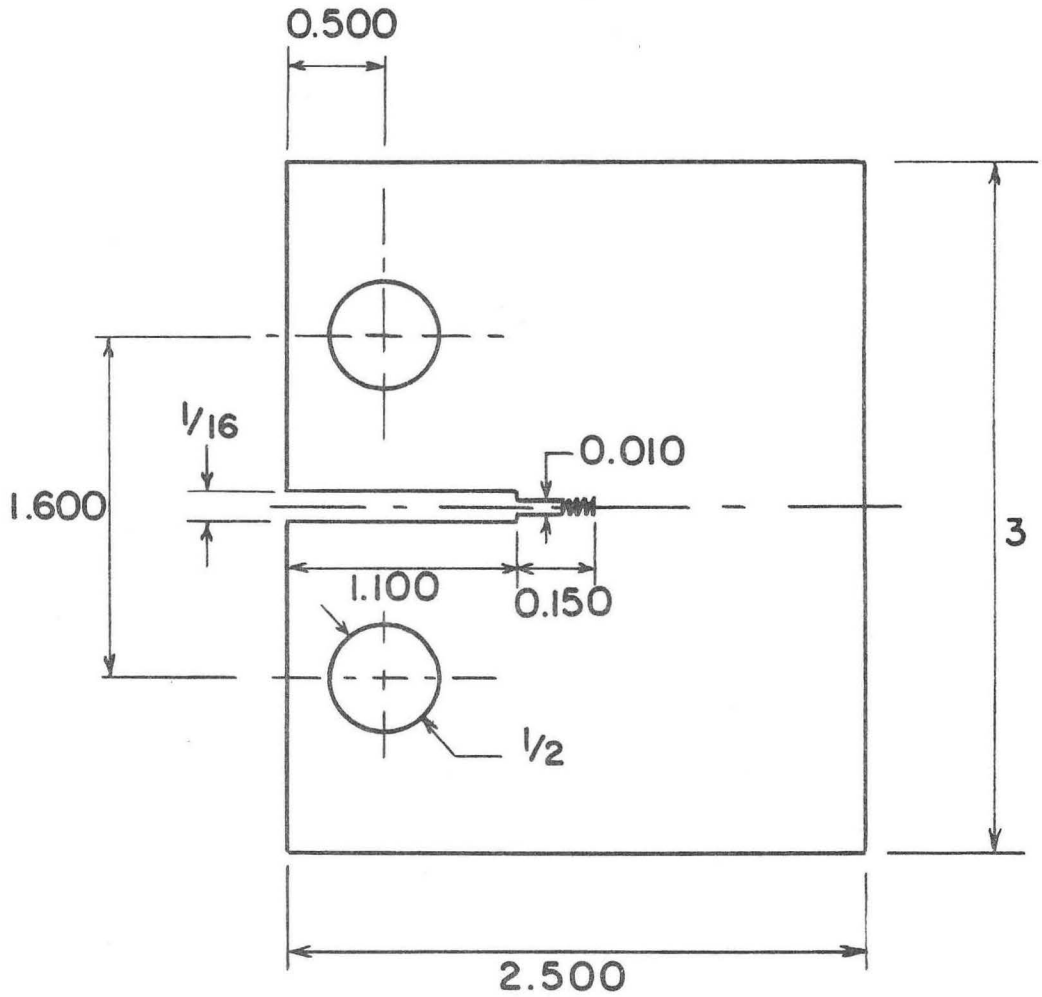

SPECIMEN THICKNESS = 0.125

XBL 694-385

Figure 2

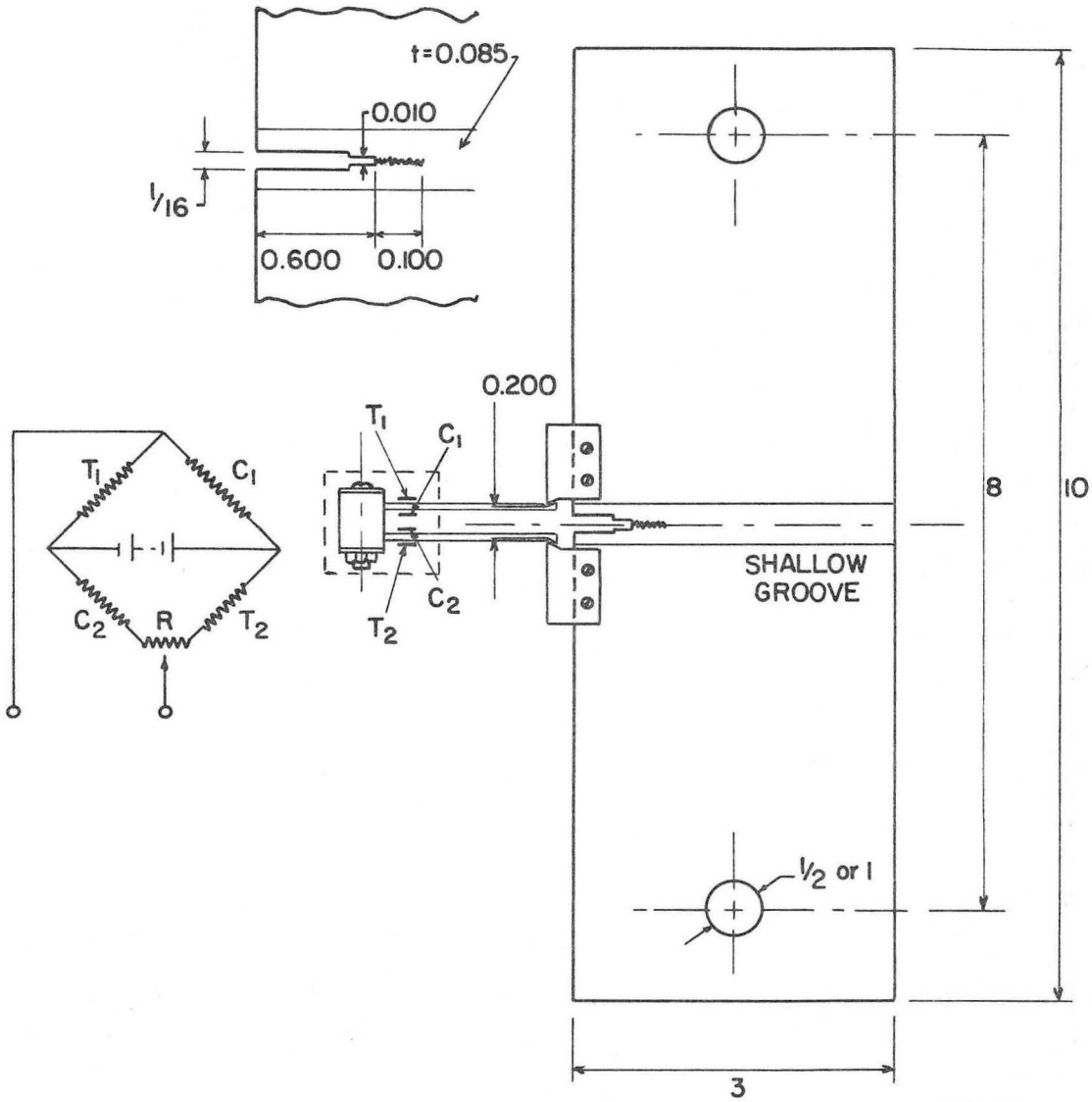

XBL 694-384

Figure 3

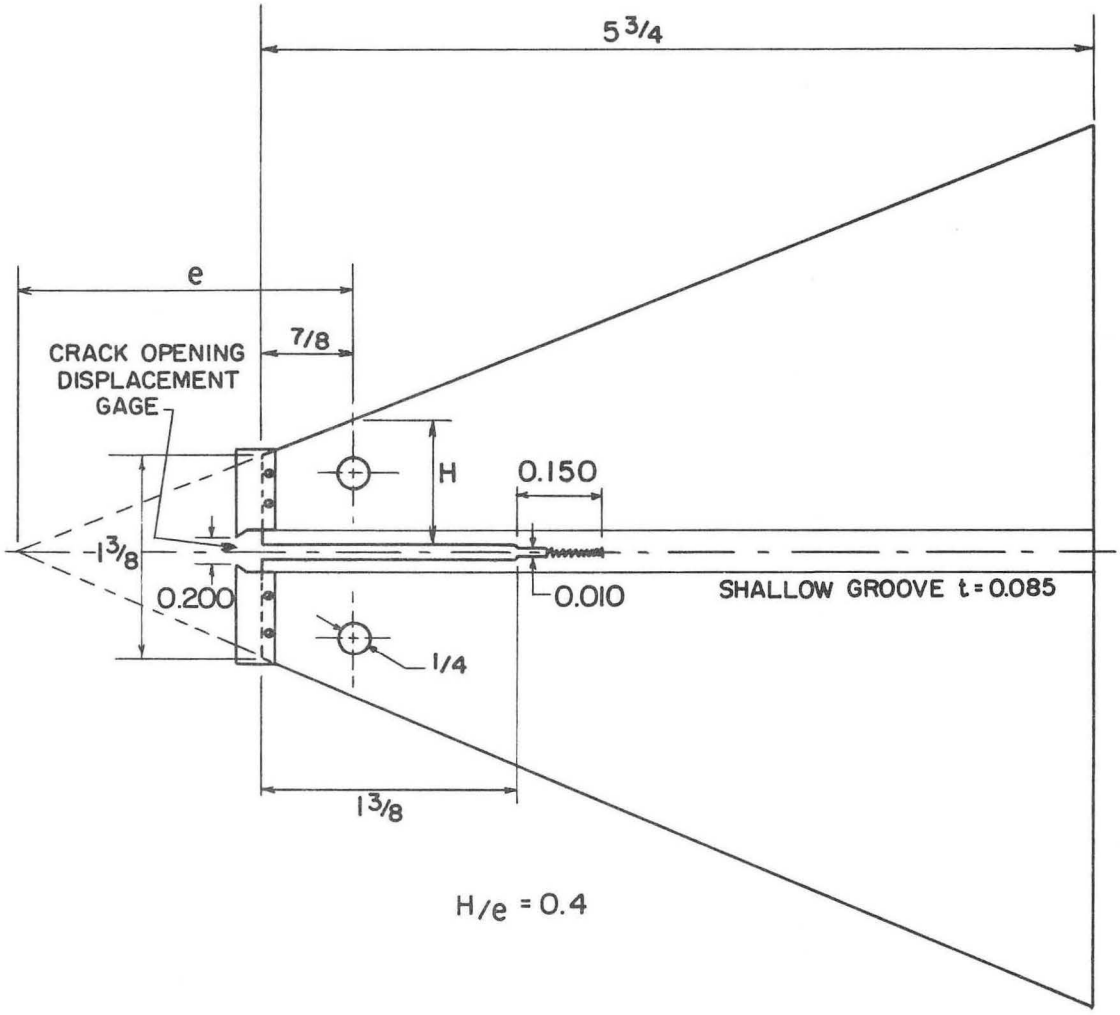

XBL 694-383

Figure 4

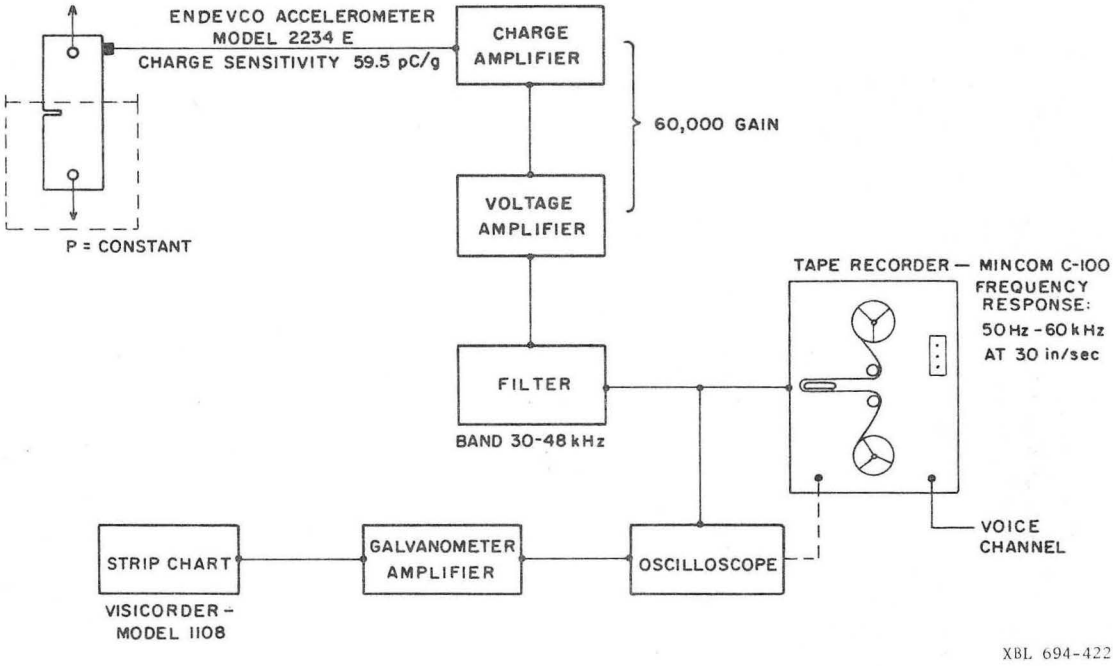
ENDEVCO ACCELEROMETER
MODEL 2234 E
CHARGE SENSITIVITY 59.5 pC/g
CHARGE AMPLIFIER
60,000 GAIN
VOLTAGE AMPLIFIER
P = CONSTANT
TAPE RECORDER — MINCOM C-100
FREQUENCY RESPONSE:
50 Hz - 60 kHz
AT 30 in/sec
FILTER
BAND 30-48 kHz
VOICE CHANNEL
STRIP CHART
GALVANOMETER AMPLIFIER
OSCILLOSCOPE
VISICORDER - MODEL 1108
XBL 694-422

Figure 5

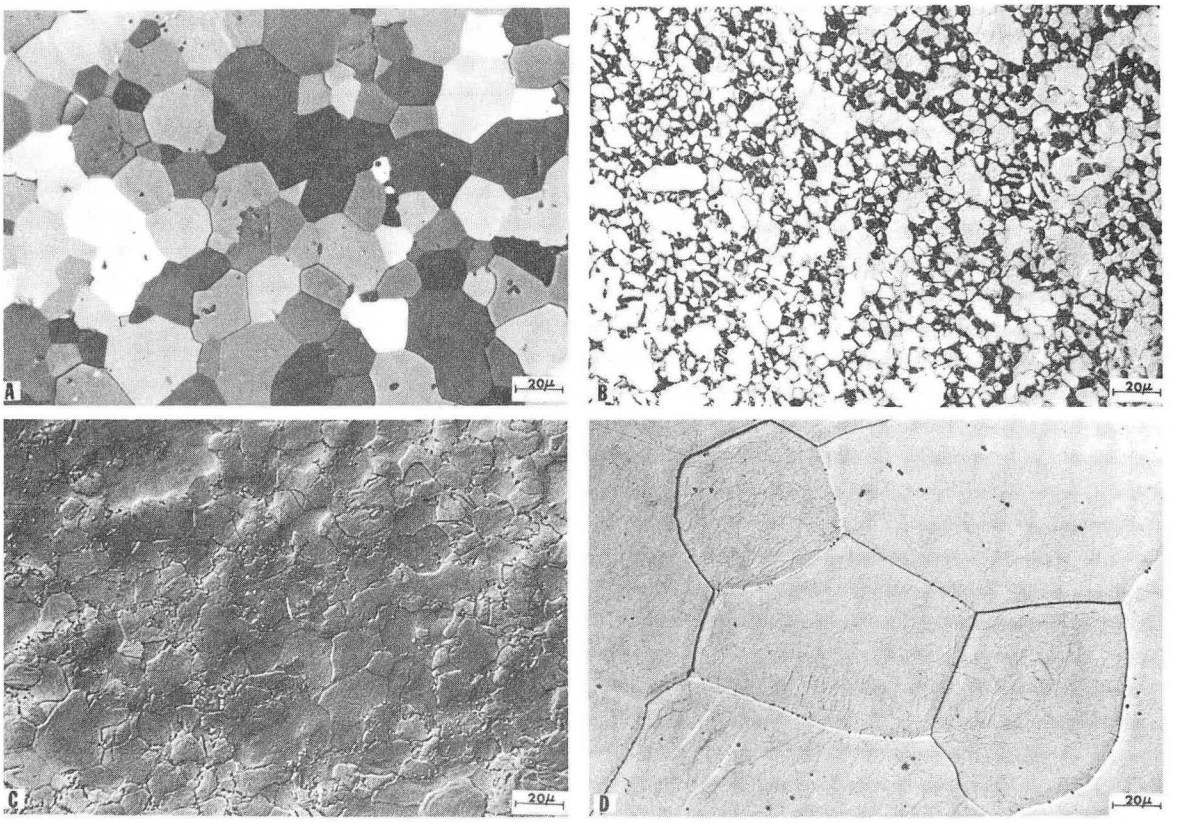

XBB 6812-7715

Figure 6

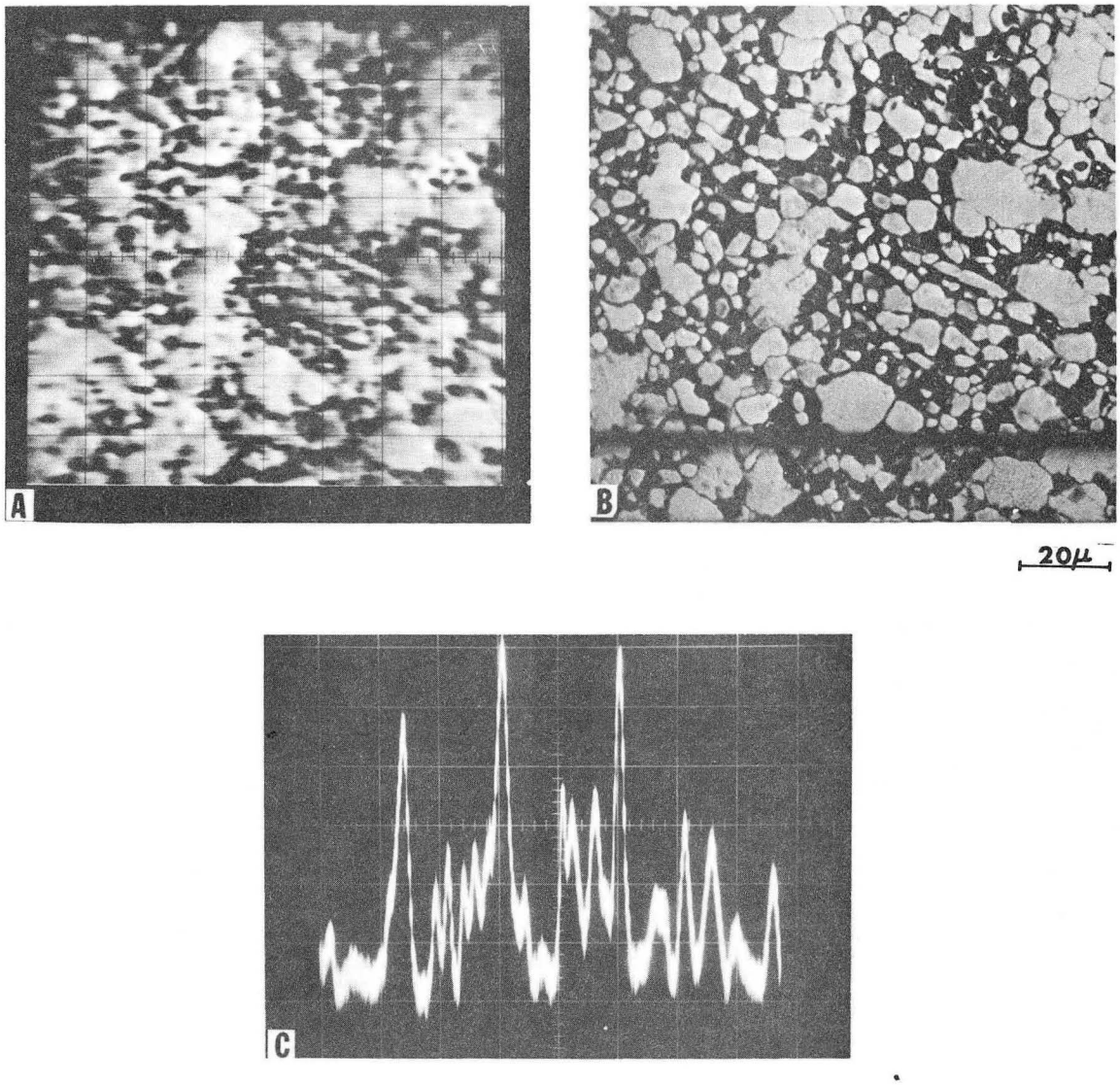

XBB 6812-7716

Figure 7

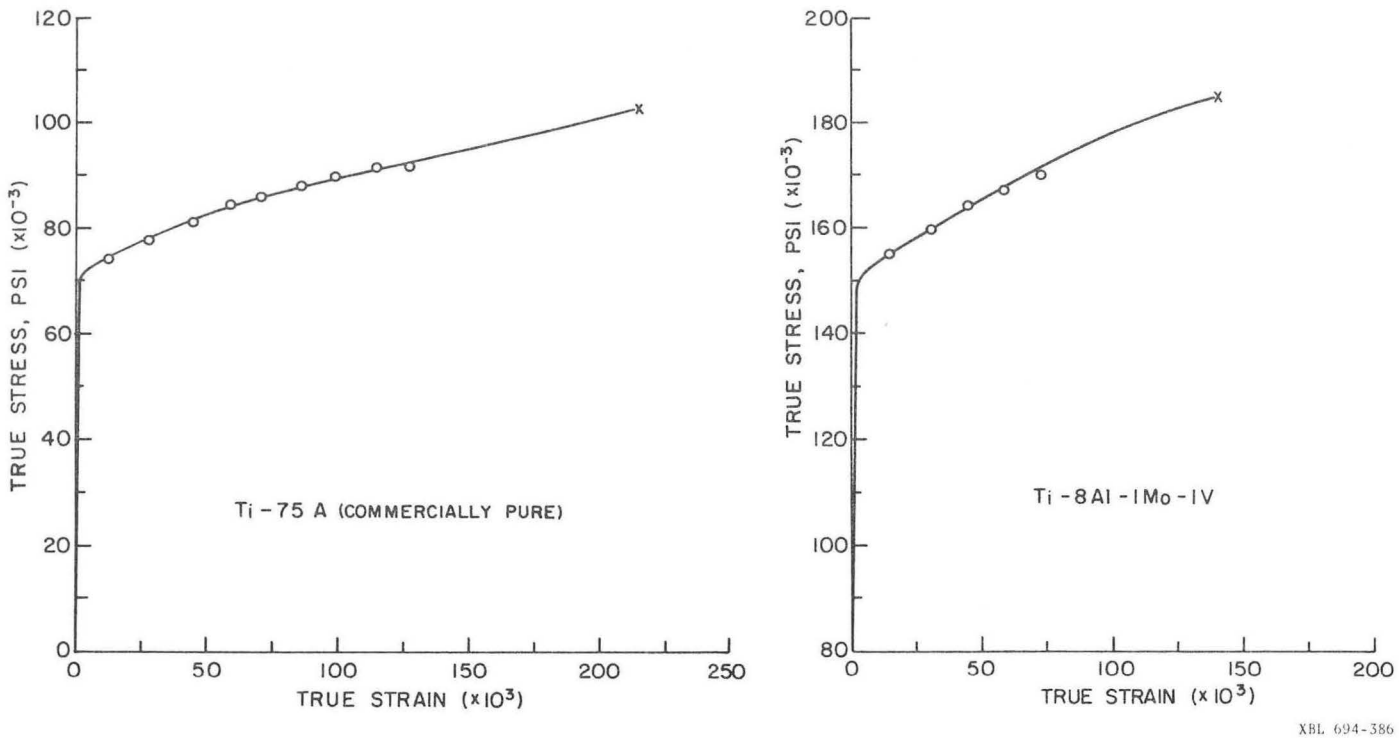
TRUE STRESS, PSI (x10⁻³)
TRUE STRAIN (x10³)
Ti - 75 A (COMMERCIALLY PURE)
Ti - 8Al - 1Mo - 1V
XBL 694-386

Figure 8

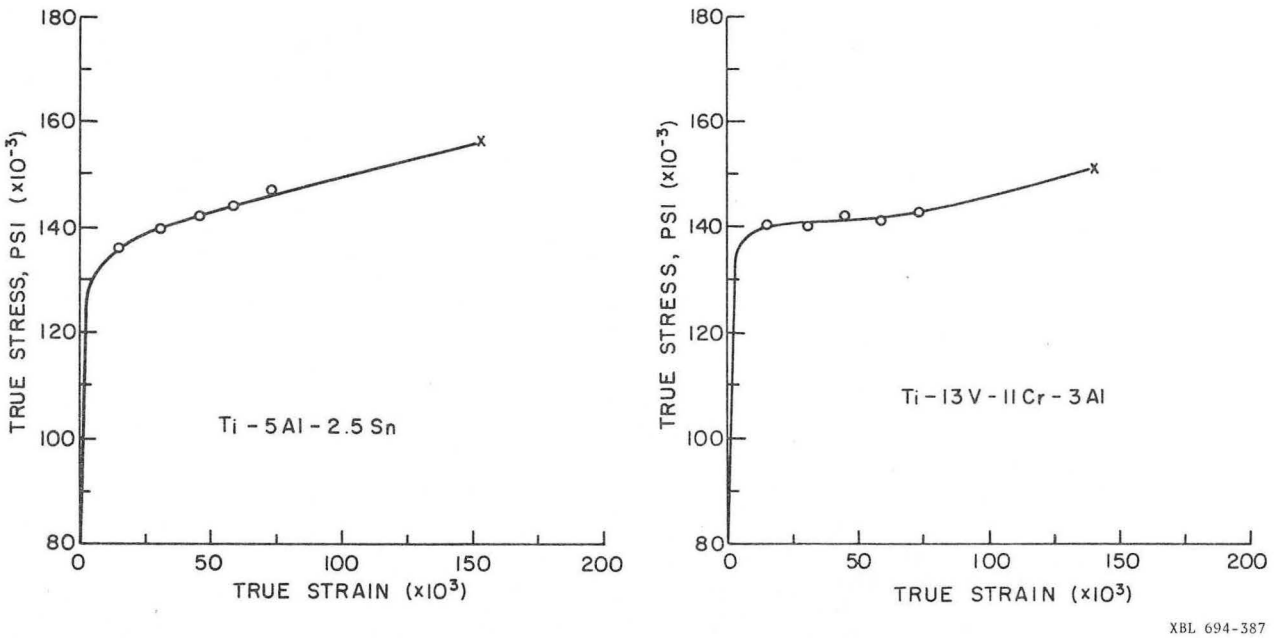
180
160
140
120
100
80
TRUE STRESS, PSI (x10⁻³)
Ti - 5 Al - 2.5 Sn
0
50
100
150
200
TRUE STRAIN (x10³)
180
160
140
120
100
80
TRUE STRESS, PSI (x10⁻³)
Ti - 13 V - 11 Cr - 3 Al
0
50
100
150
200
TRUE STRAIN (x10³)
XBL 694-387

Figure 9

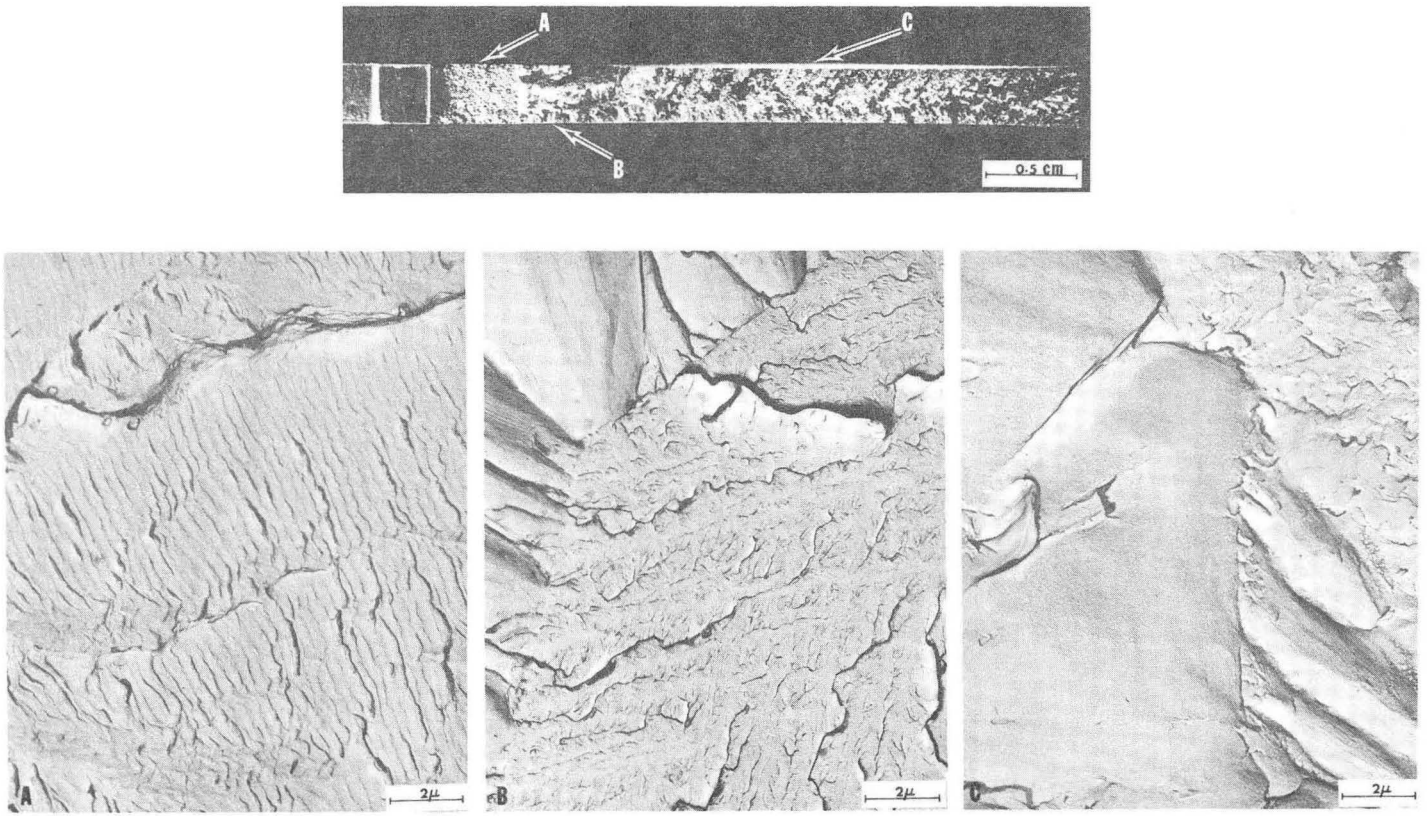

XBB 6812-7703

Figure 10

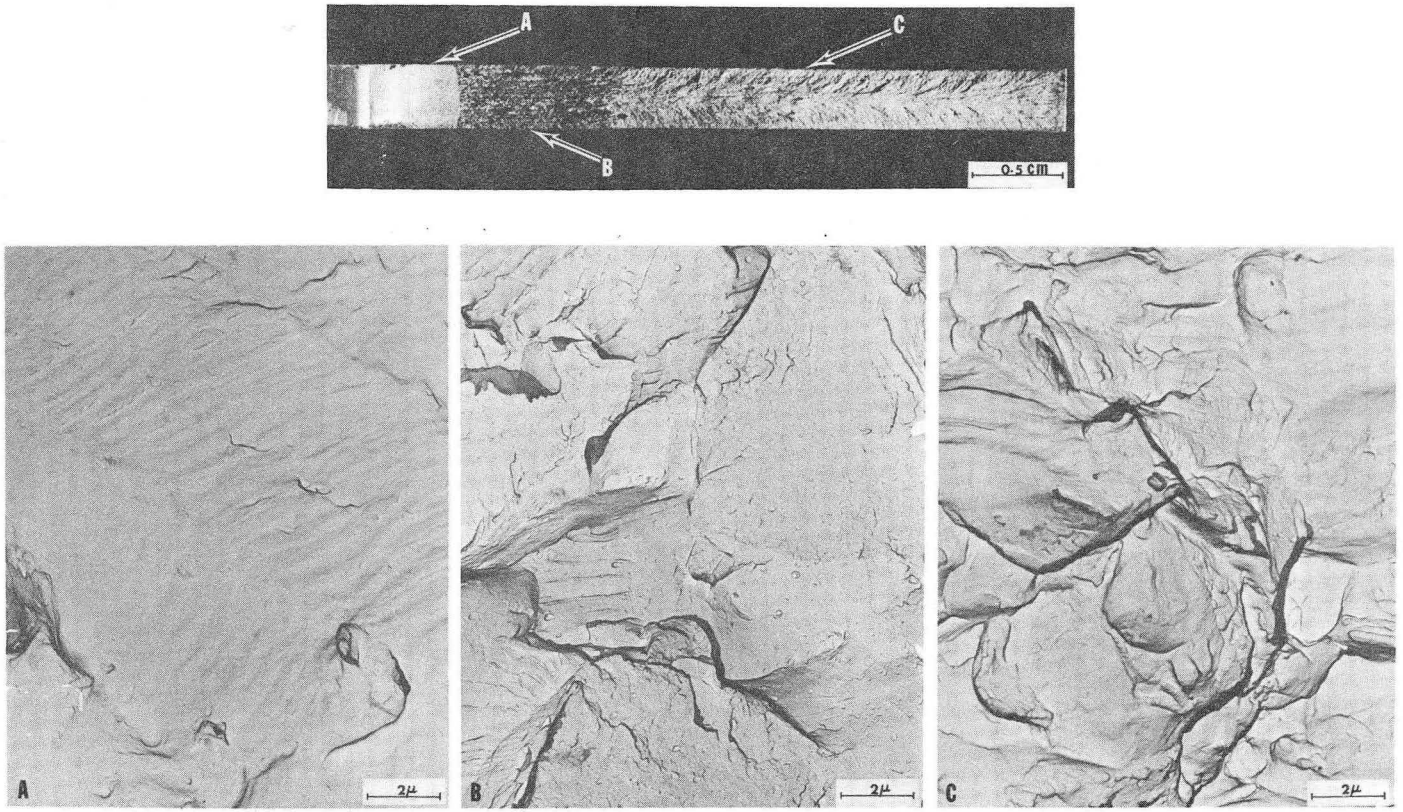

XBB 6812-7706

Figure 11

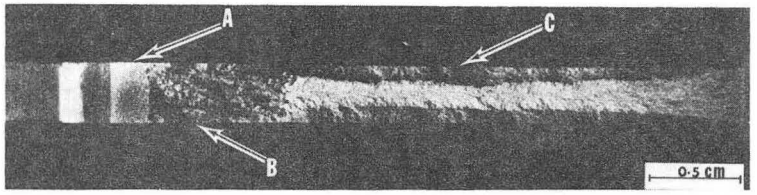

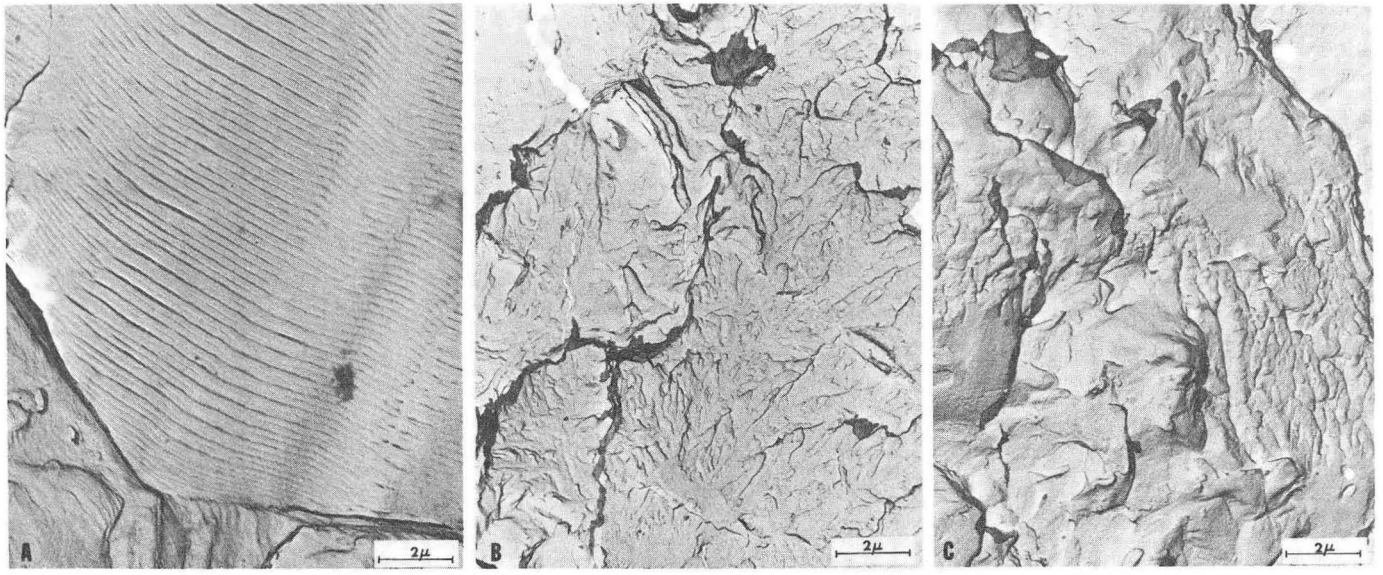

XBB 6812-7705

Figure 12

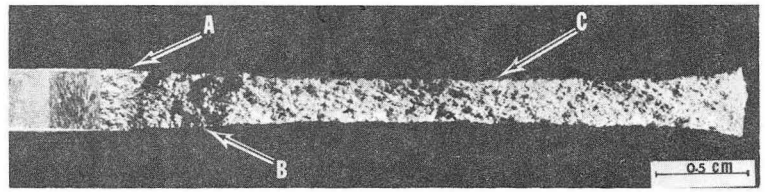

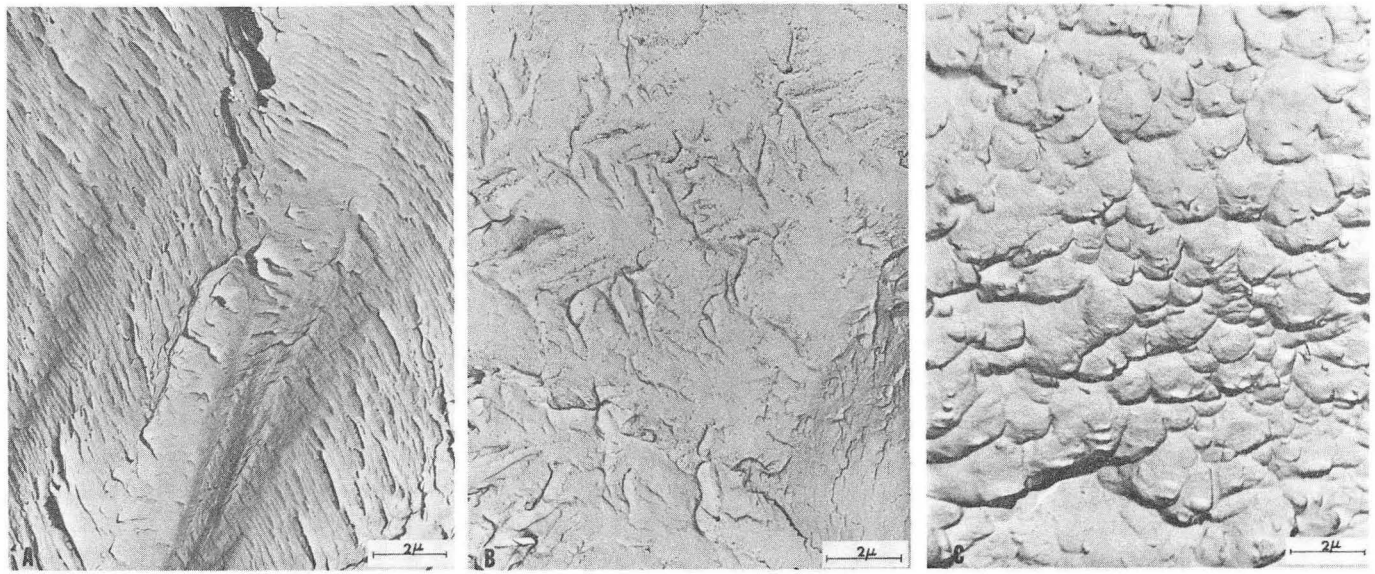

XBB 6812-7704

Figure 13

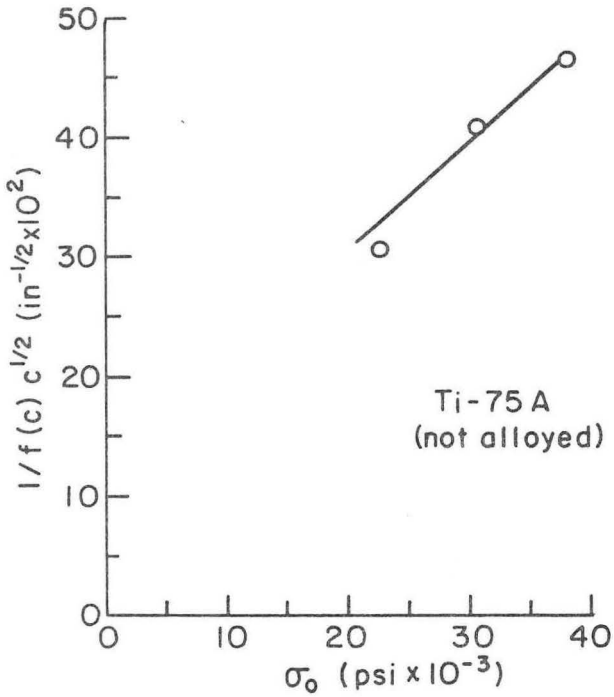

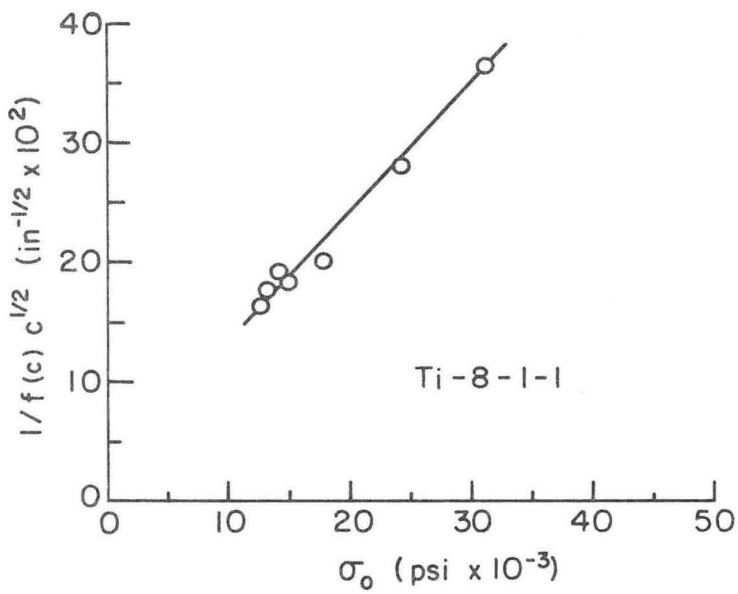

XBL 695-464

Figure 14

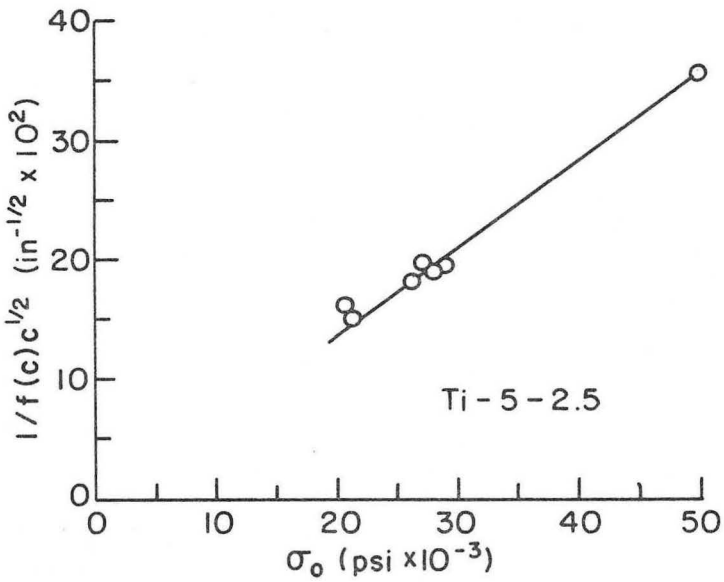

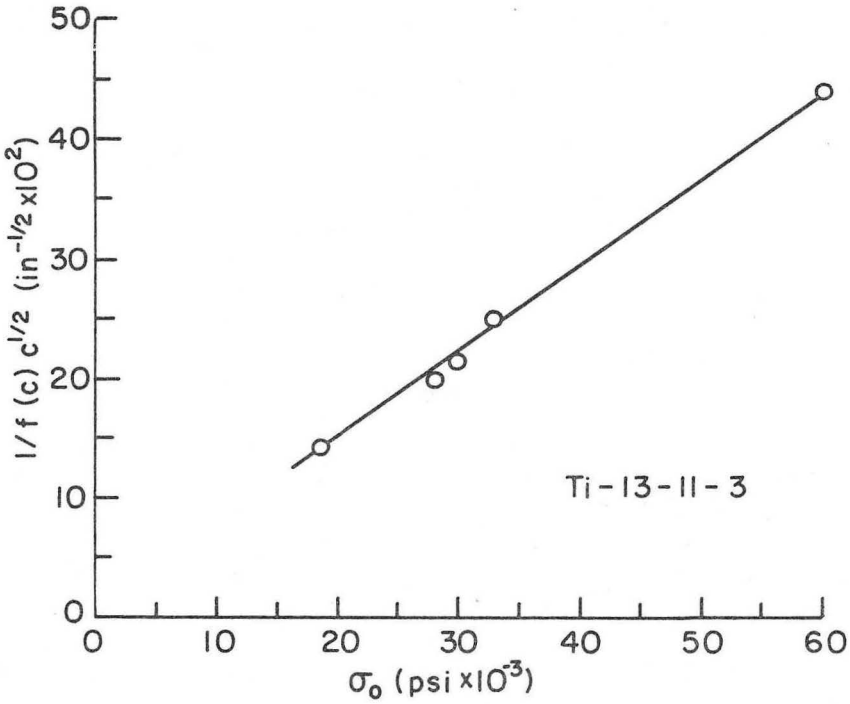

XBL 695-465

Figure 15

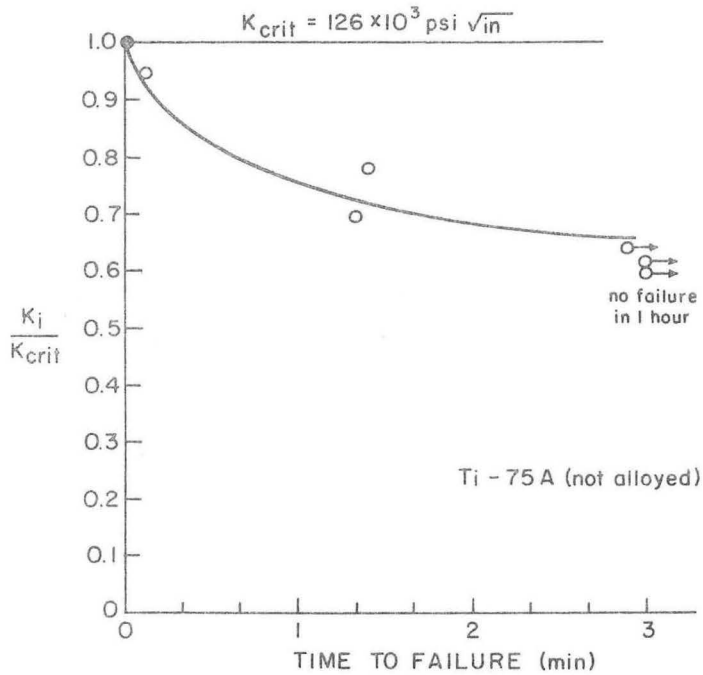

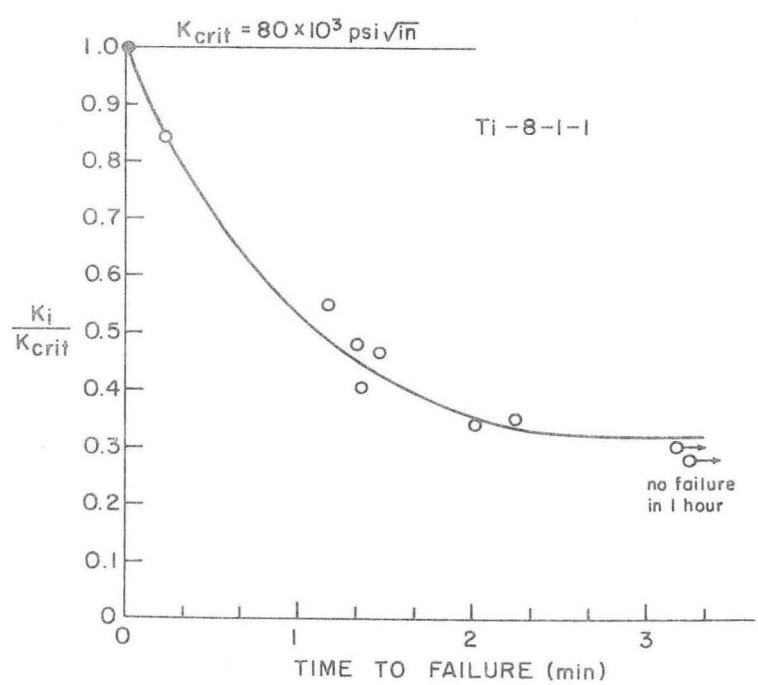

XBL 695-463

Figure 16

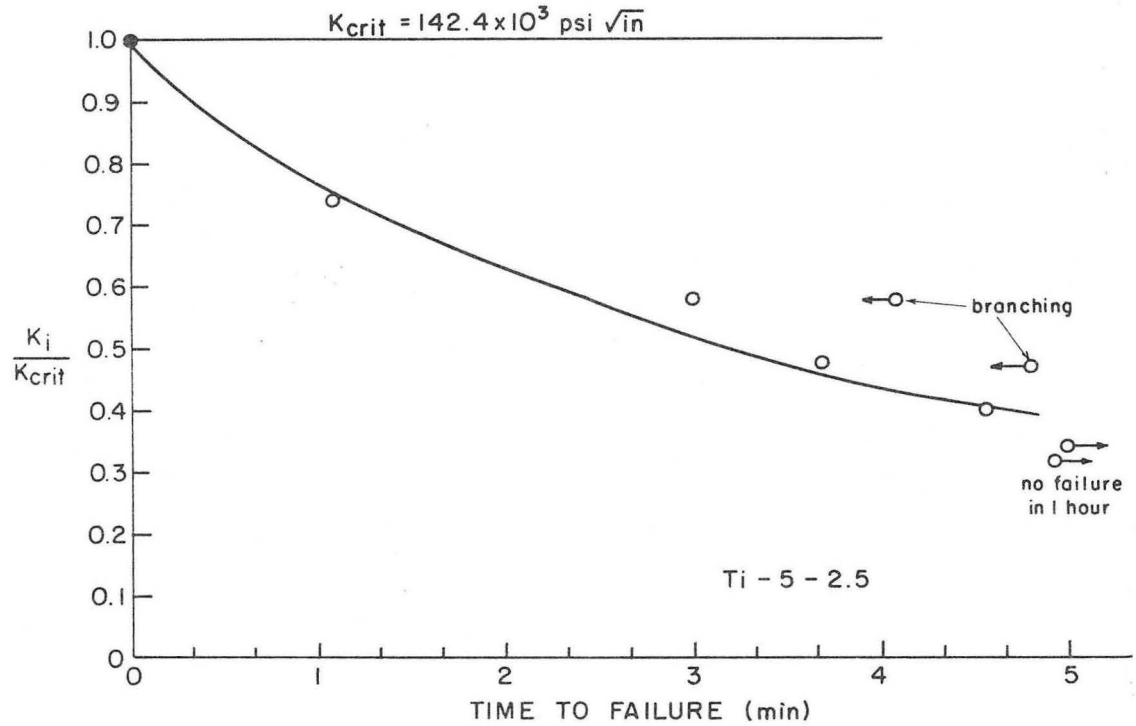

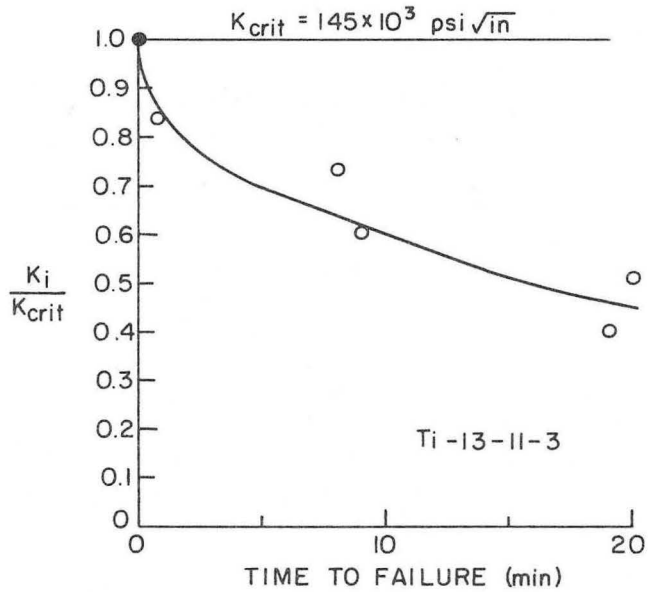

XBL 695-462

Figure 17

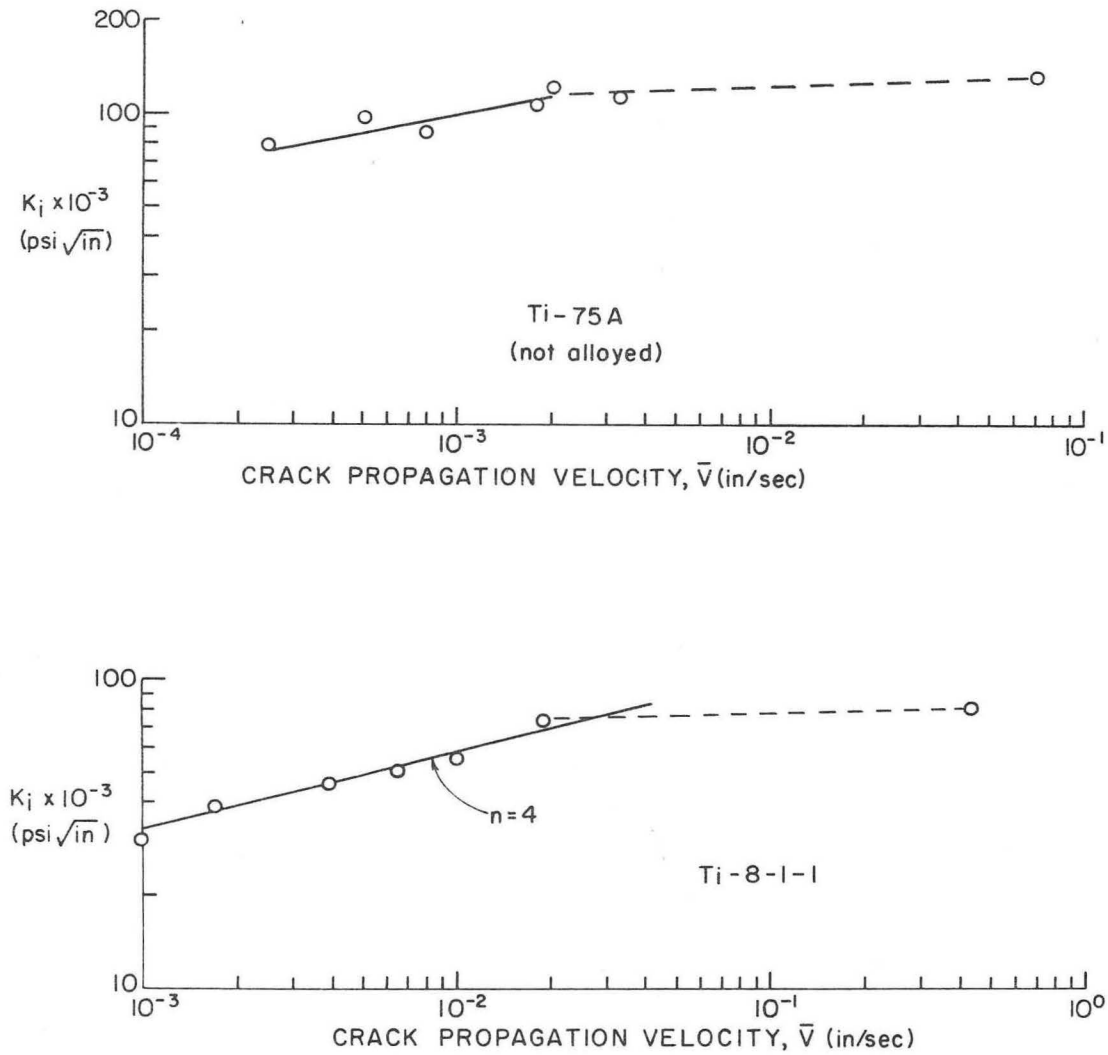

XBL 696-661

Figure 18

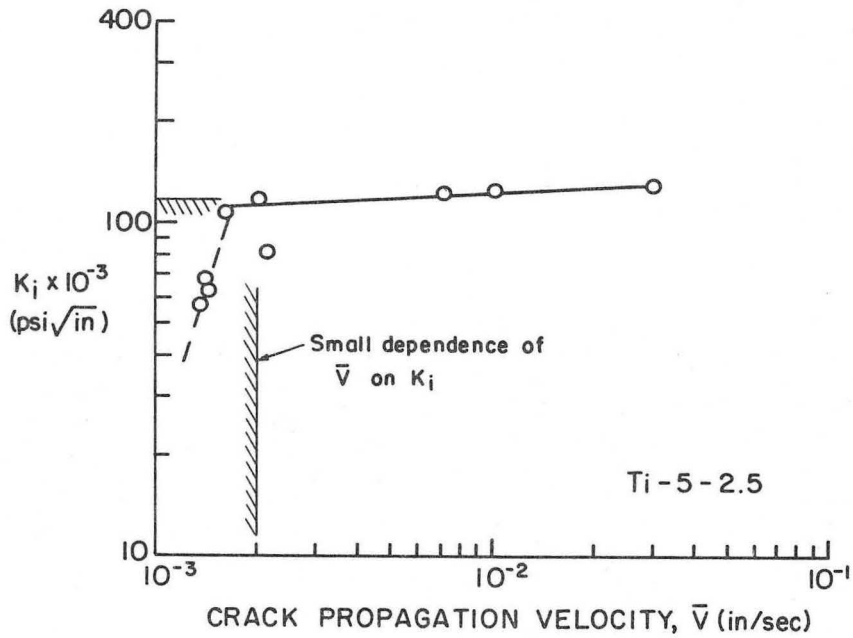

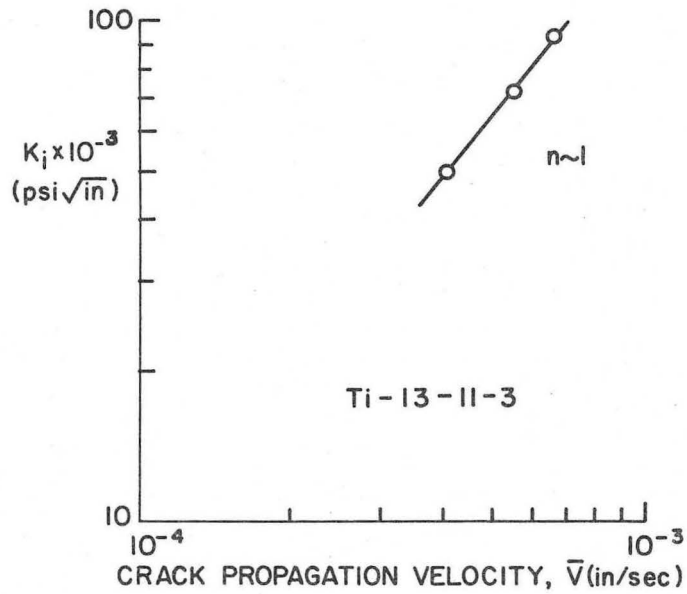

XBL 696-662

Fig. 19

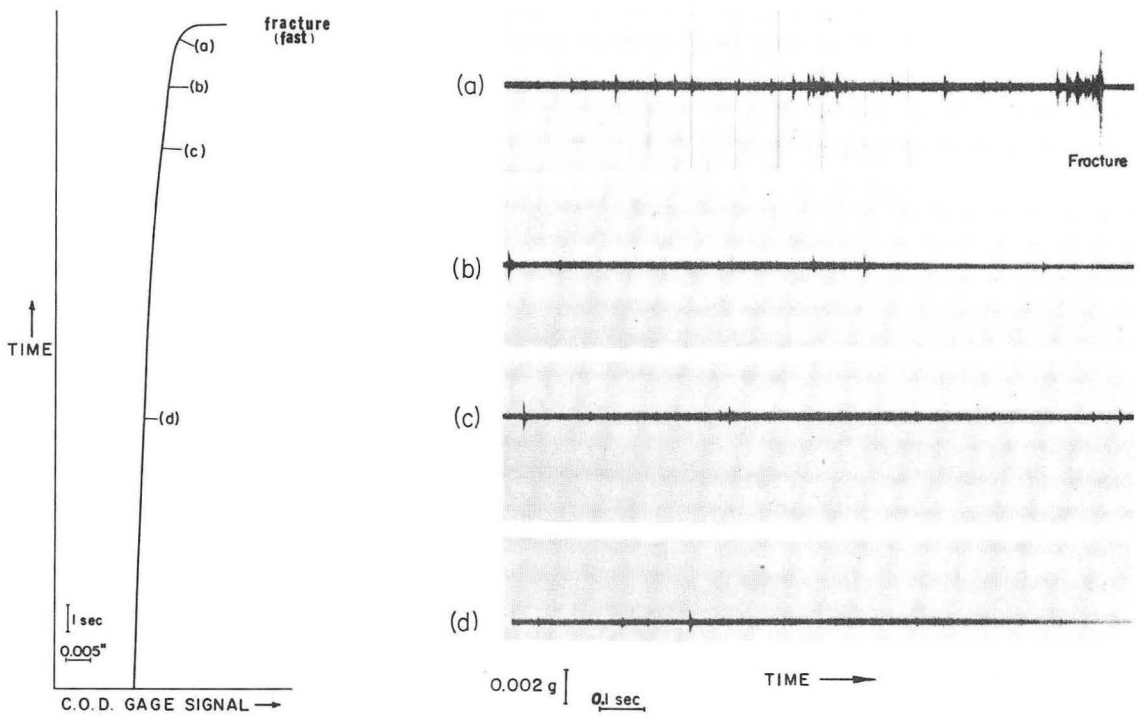

XBB 696-3981

Figure 20

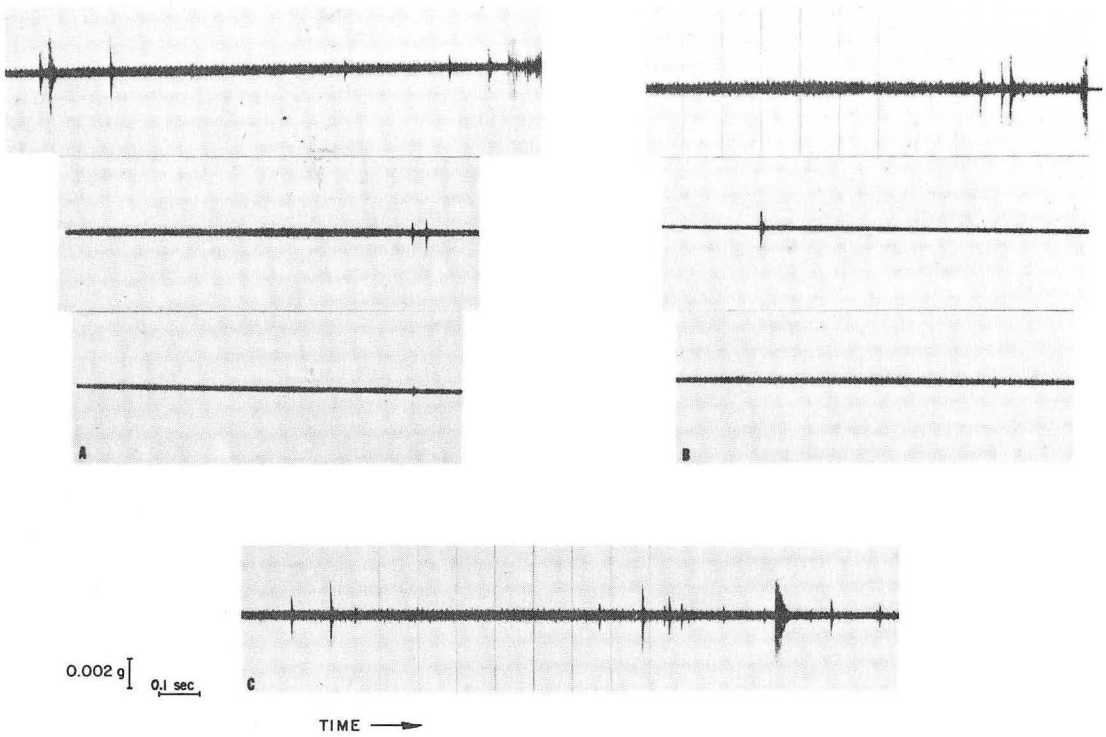

XBB 696-3980

Figure 21

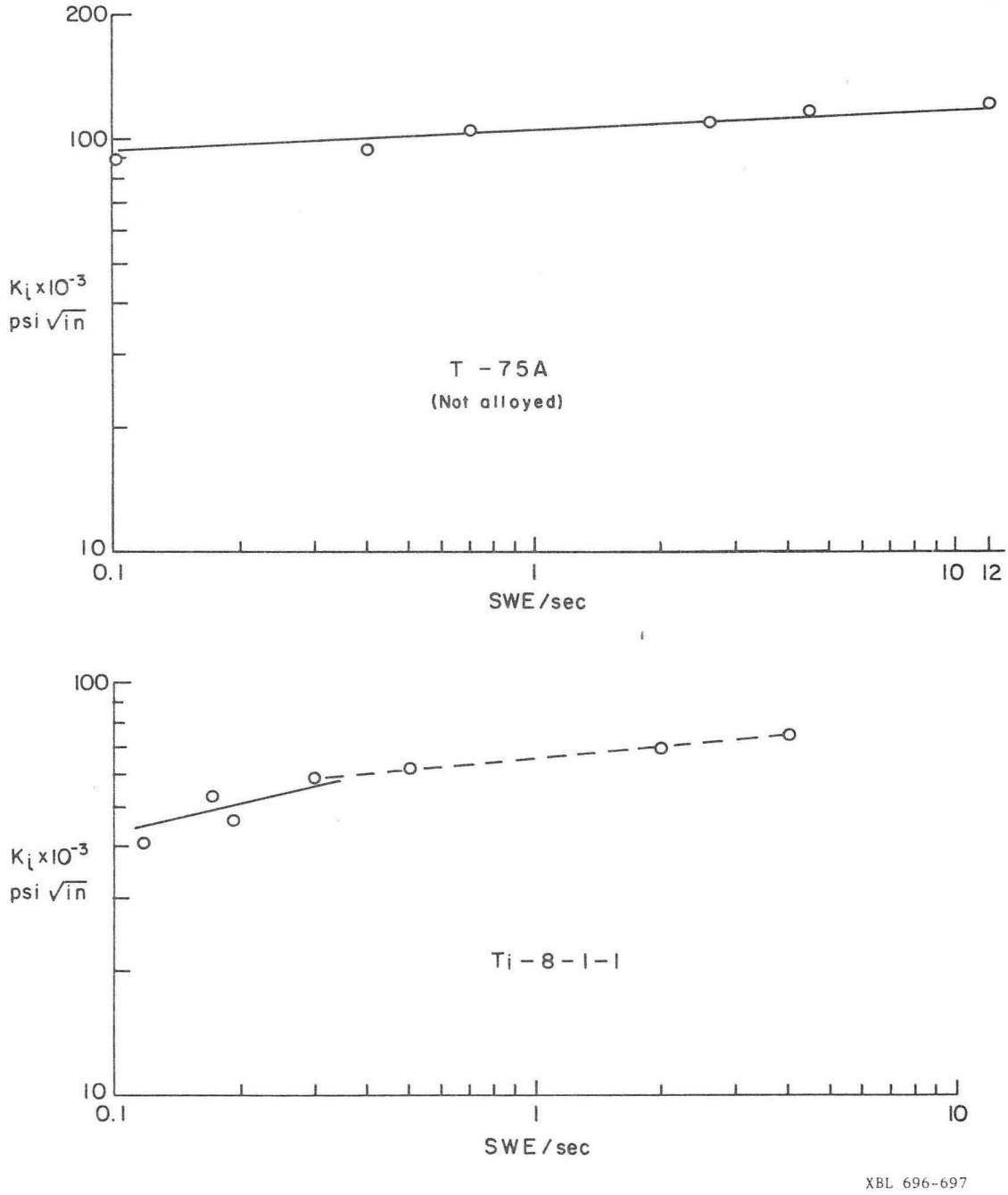
200
100
10
$K_i \times 10^{-3}$
psi $\sqrt{in}$
T - 75A
(Not alloyed)
0.1
1
10
12
SWE/sec
100
10
$K_i \times 10^{-3}$
psi $\sqrt{in}$
Ti - 8 - 1 - 1
0.1
1
10
SWE/sec
XBL 696-697

Figure 22

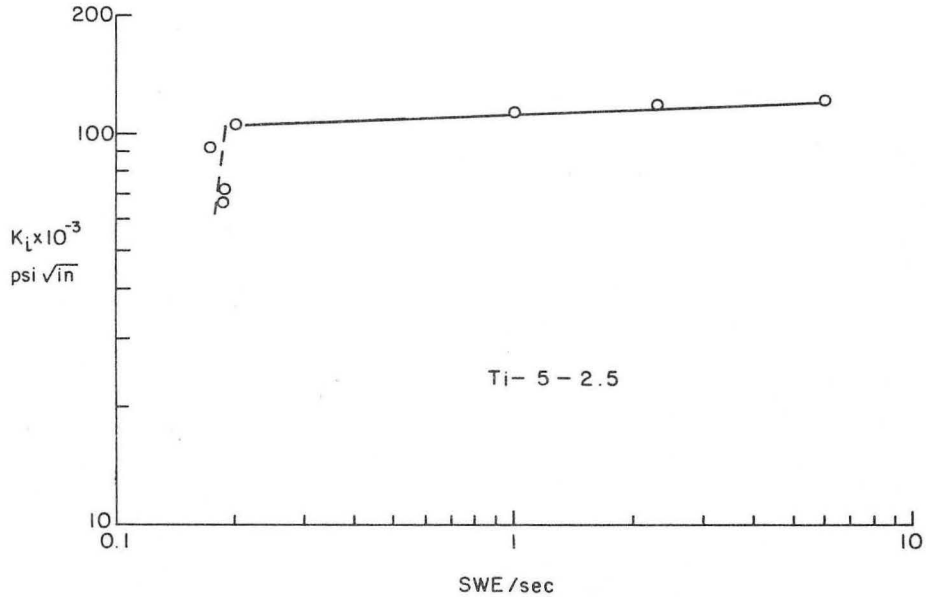

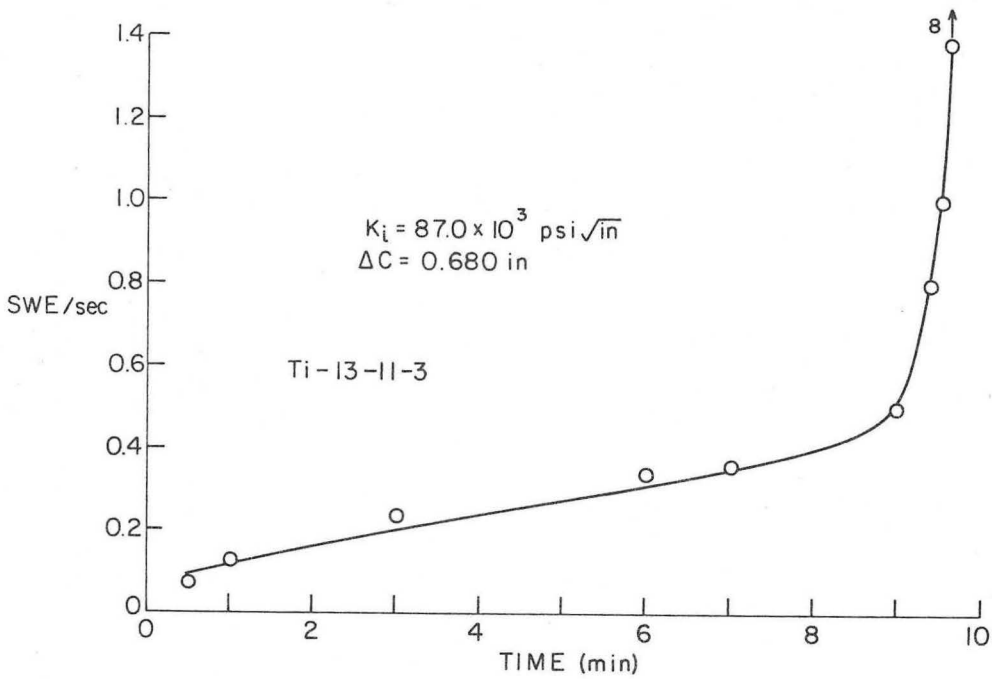

XBL 696-698

Figure 23

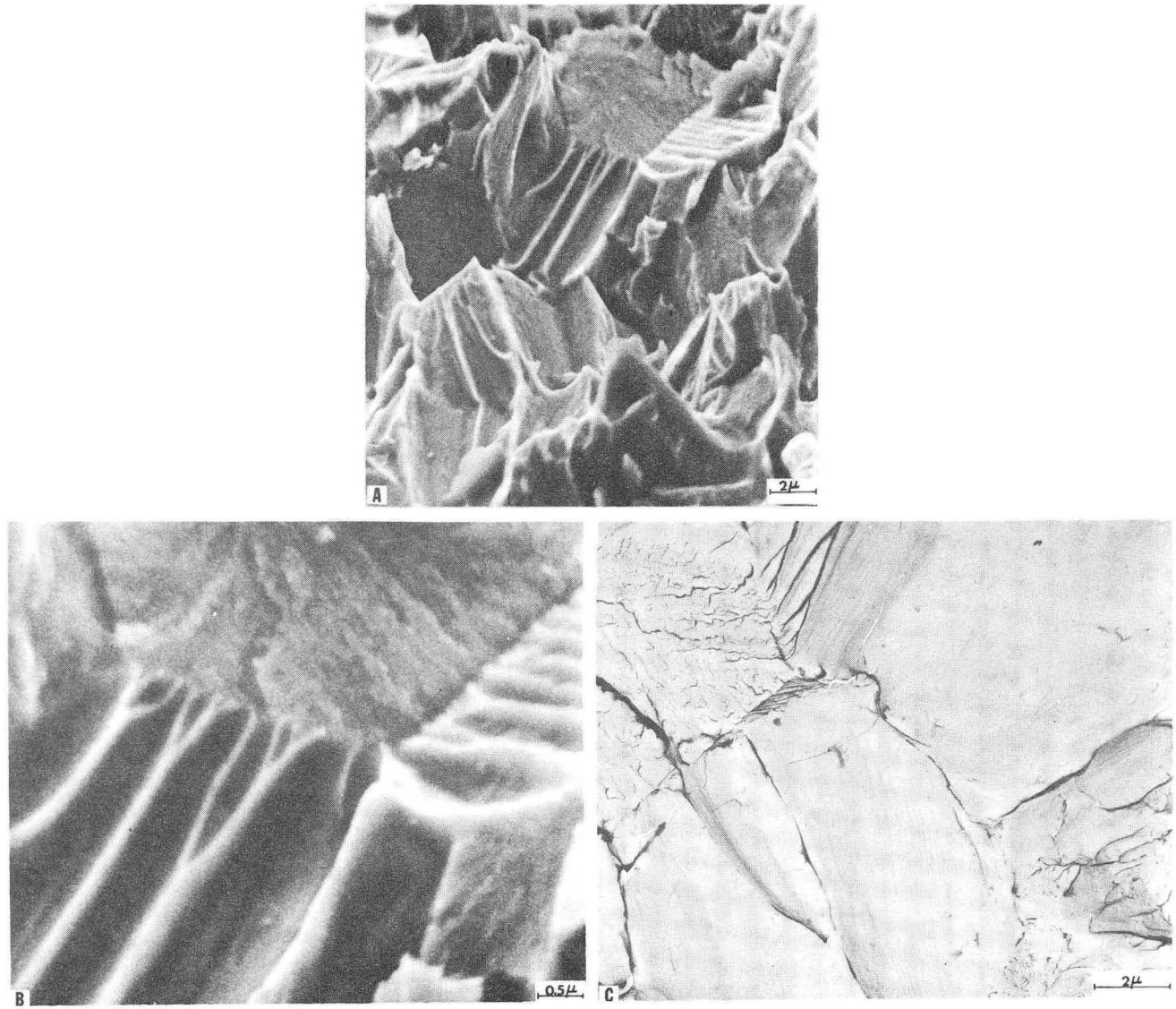

XBB 6812-7700

Figure 24

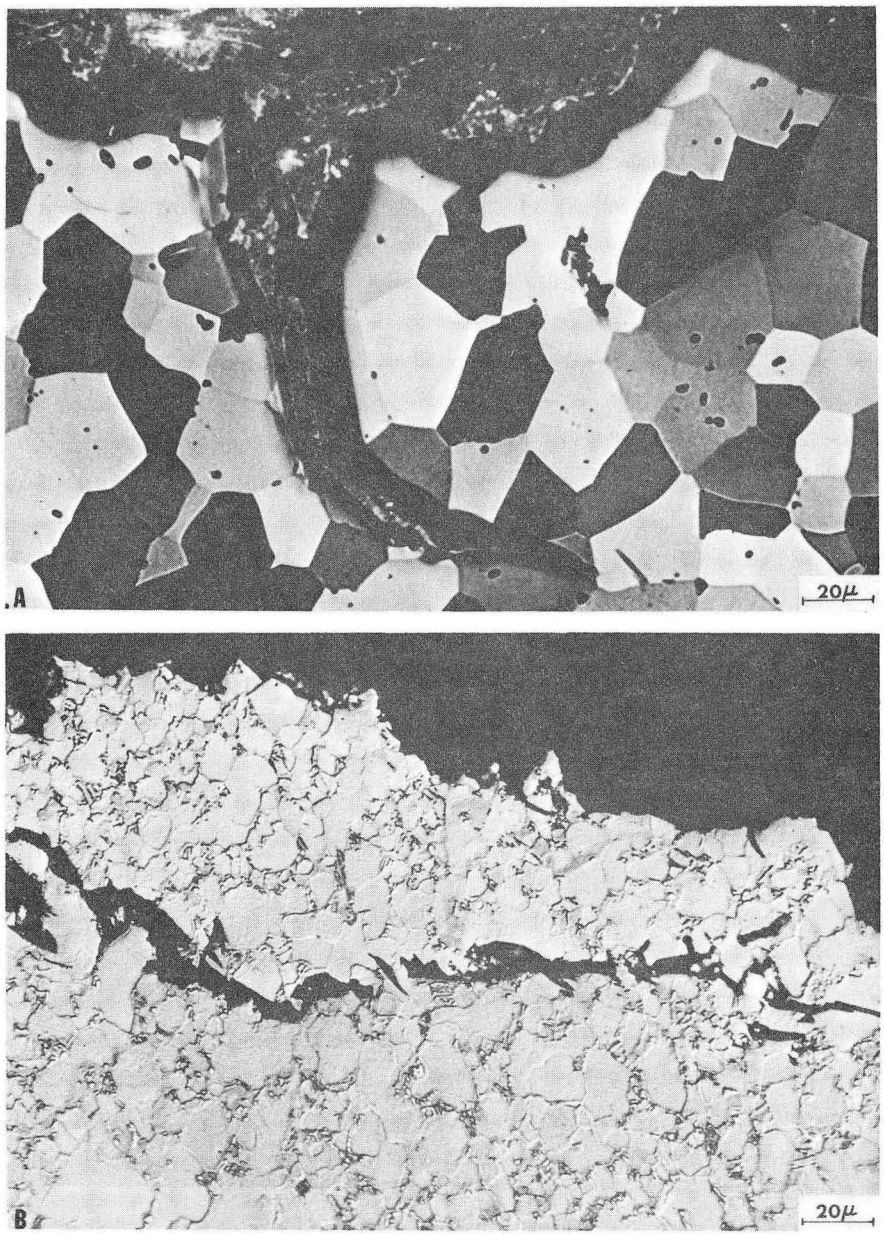

XBB 6812-7710

Figure 25

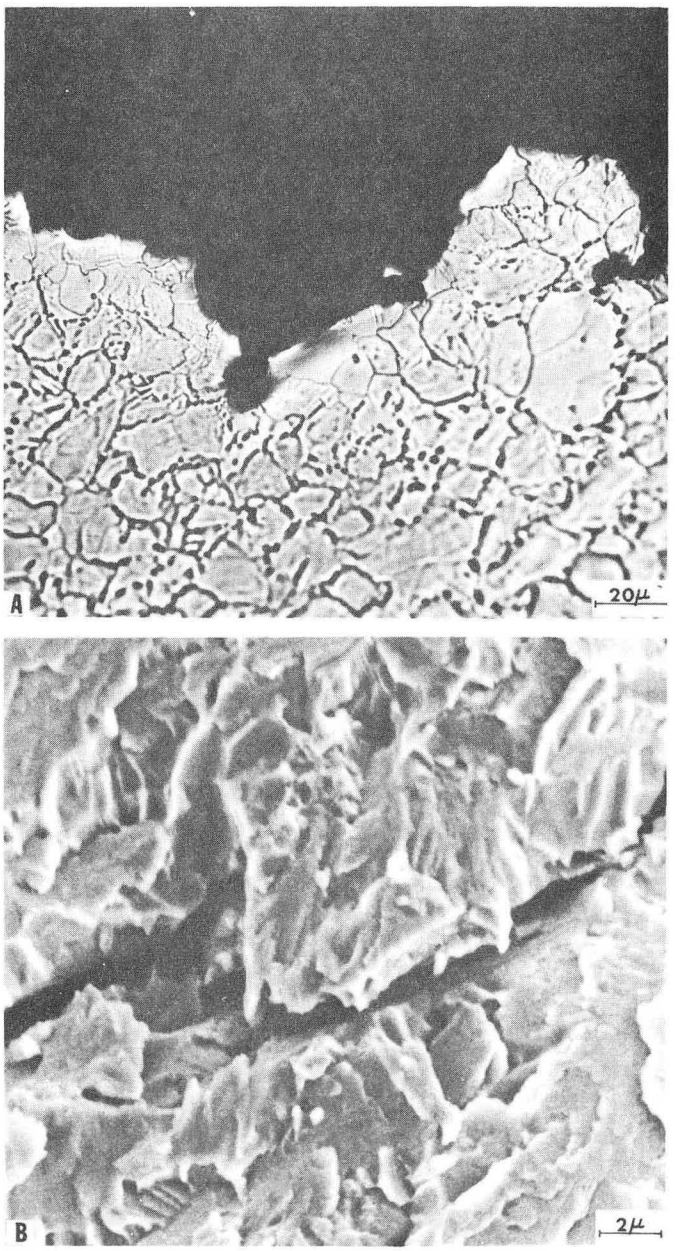

XBB 6812-7714

Figure 26

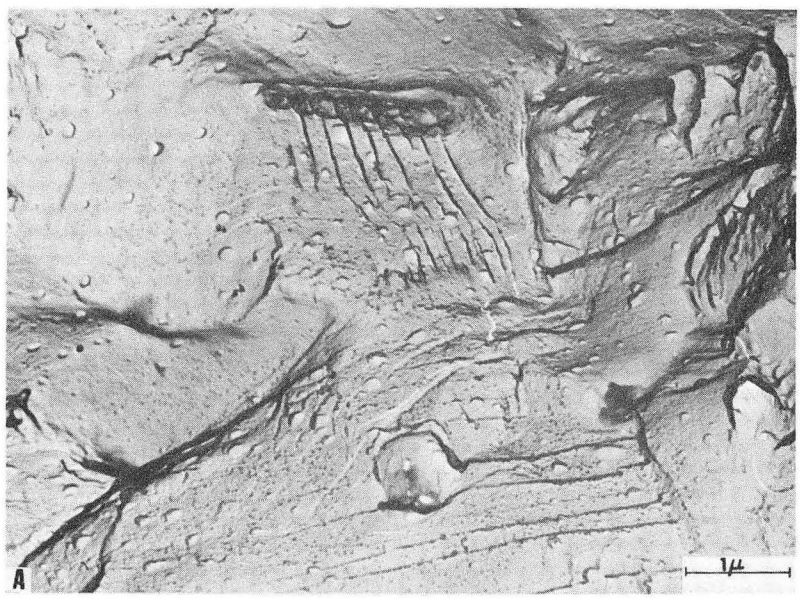

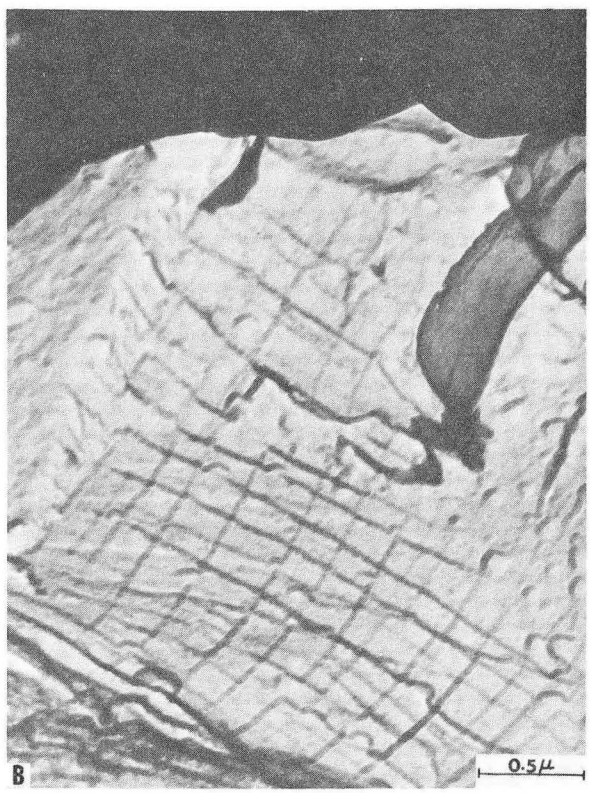

XBB 6812-7708

Figure 27

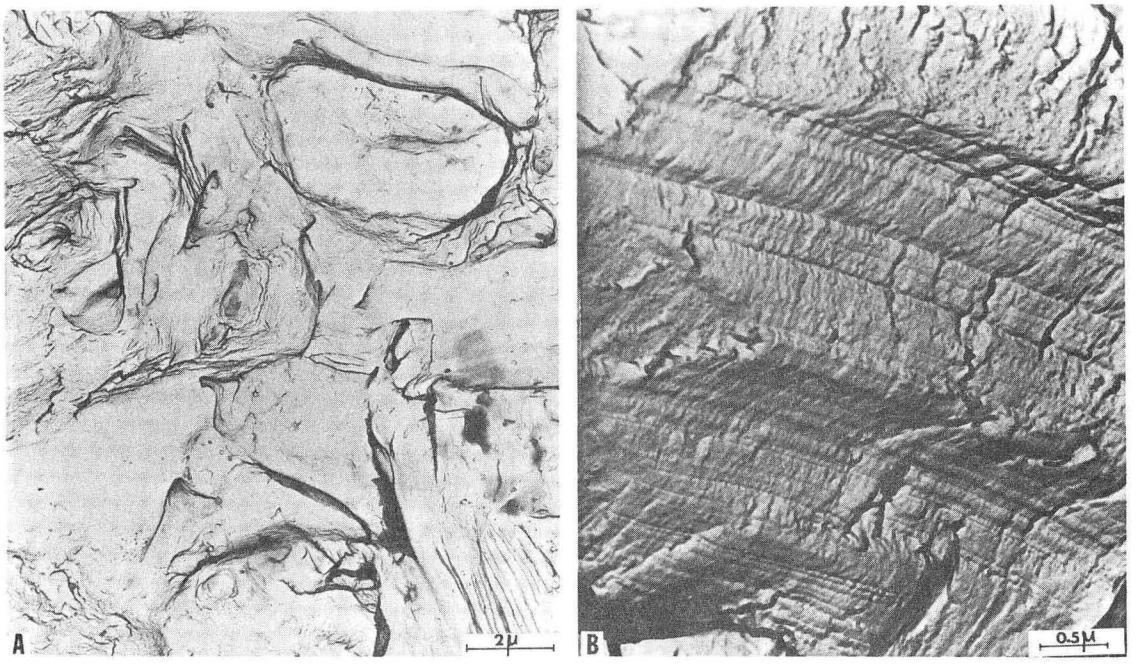

XBB 695-2724

Figure 28

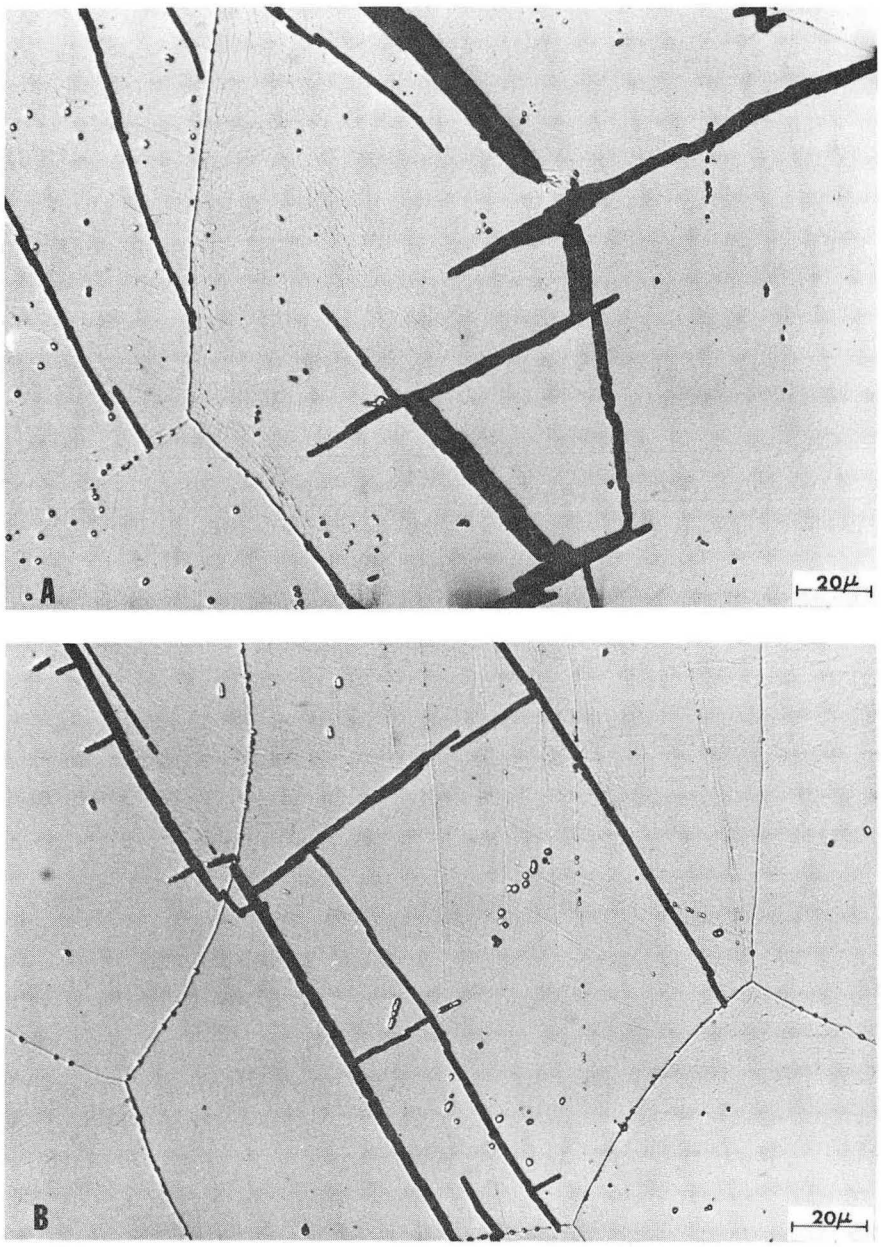

XBB 6812-7711

Figure 29

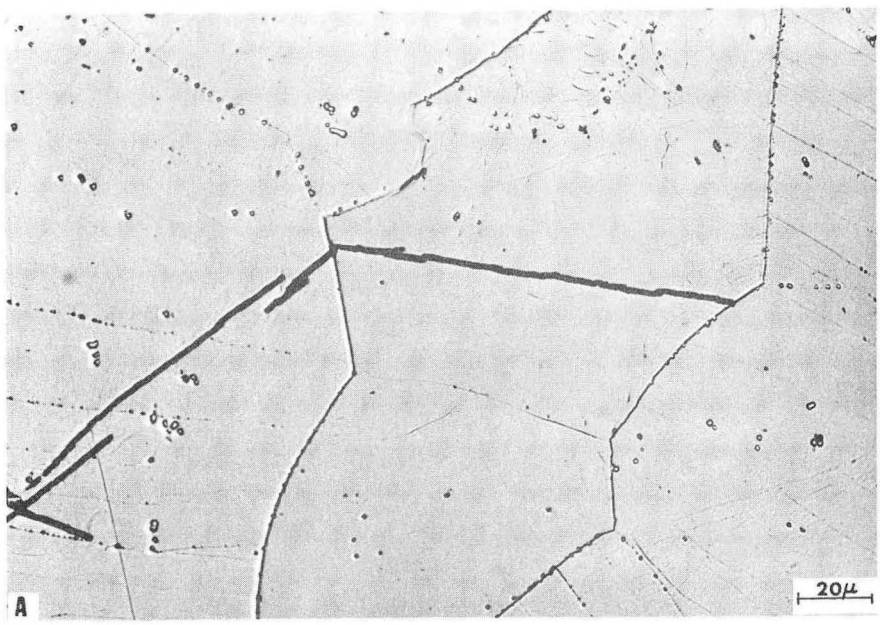

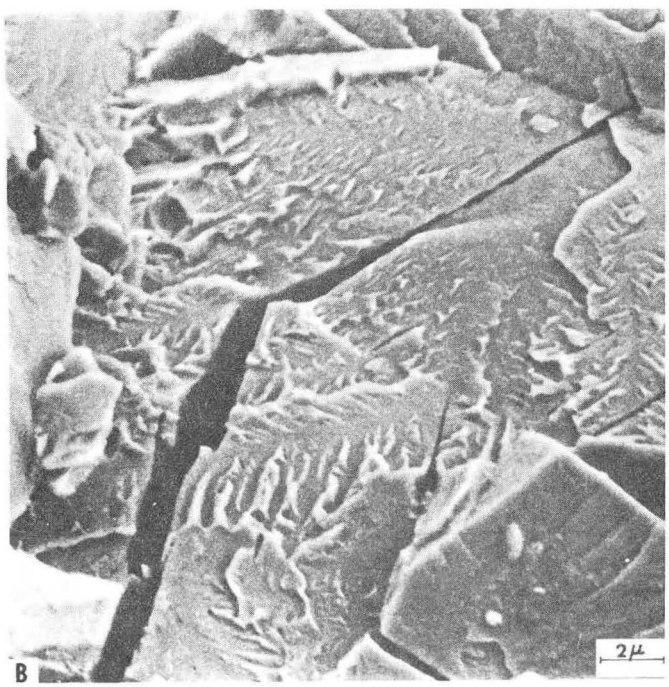

XBB 6812-7709

Figure 30

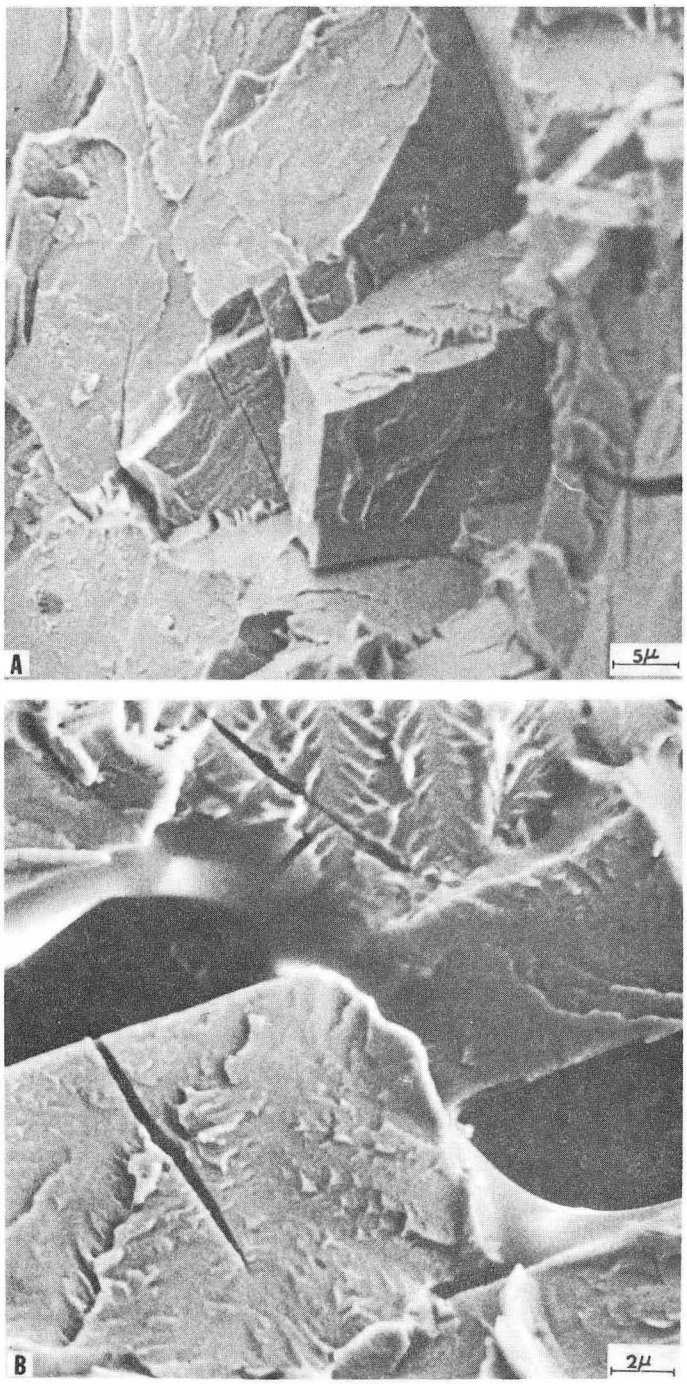

XBB 6812-7712

Figure 31

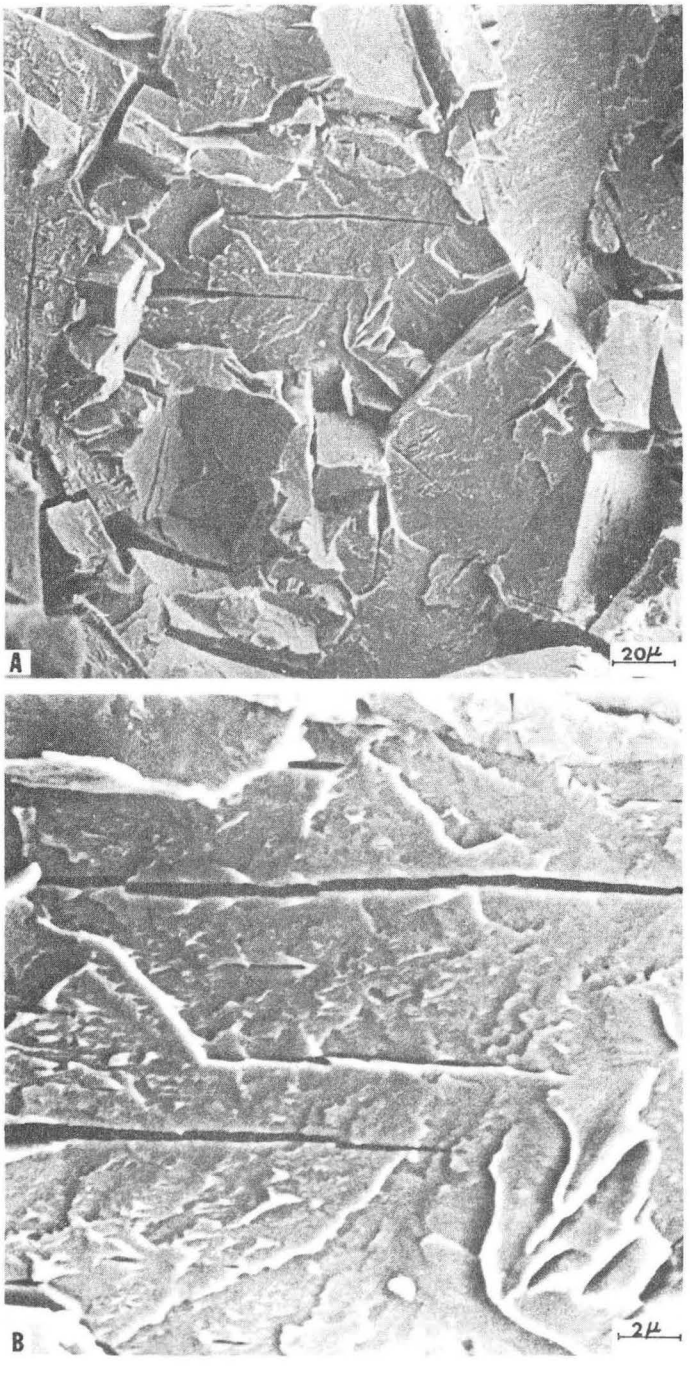

XBB 6812-7713

Figure 32

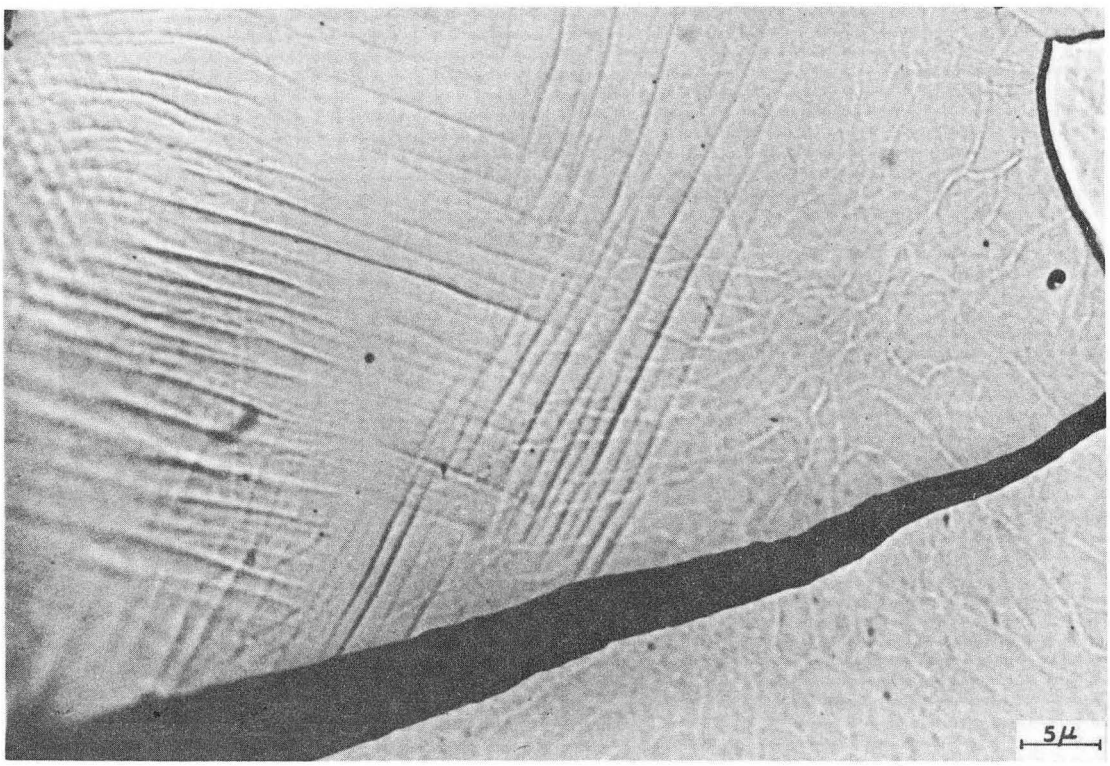

XBB 6812-7707

Figure 33

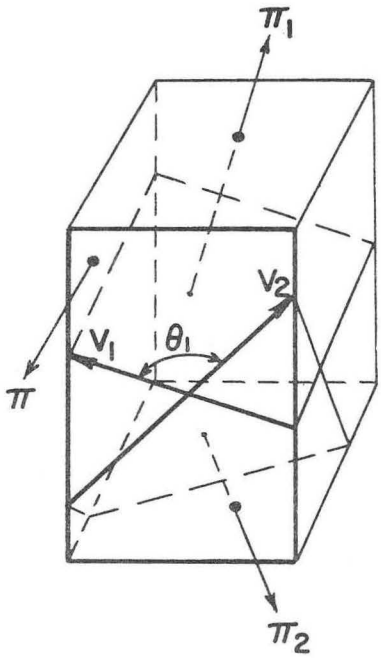

$\bar{V}_1 \perp \pi_1; \pi$

$\bar{V}_2 \perp \pi_2; \pi$

CONSIDER THE VECTOR $\bar{V}_3$
(NOT SHOWN)

$\measuredangle\ \bar{V}_1\ \bar{V}_2 = \theta_1$

$\measuredangle\ \bar{V}_1\ \bar{V}_3 = \theta_2$

$\measuredangle\ \bar{V}_2\ \bar{V}_3 = \theta_3 = 180° - (\theta_1 + \theta_2)$

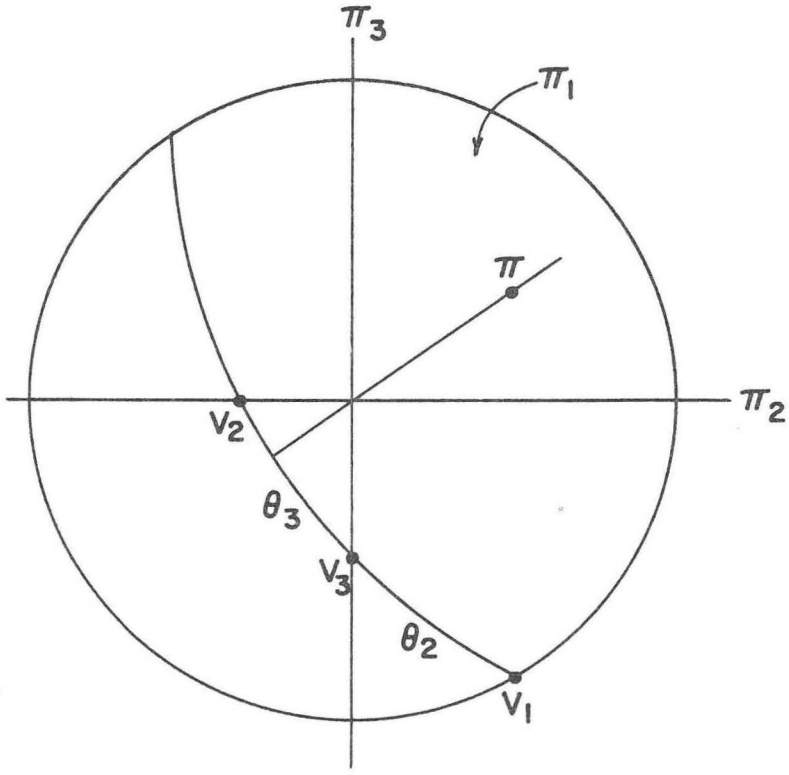

XBL 694-421

Figure 34

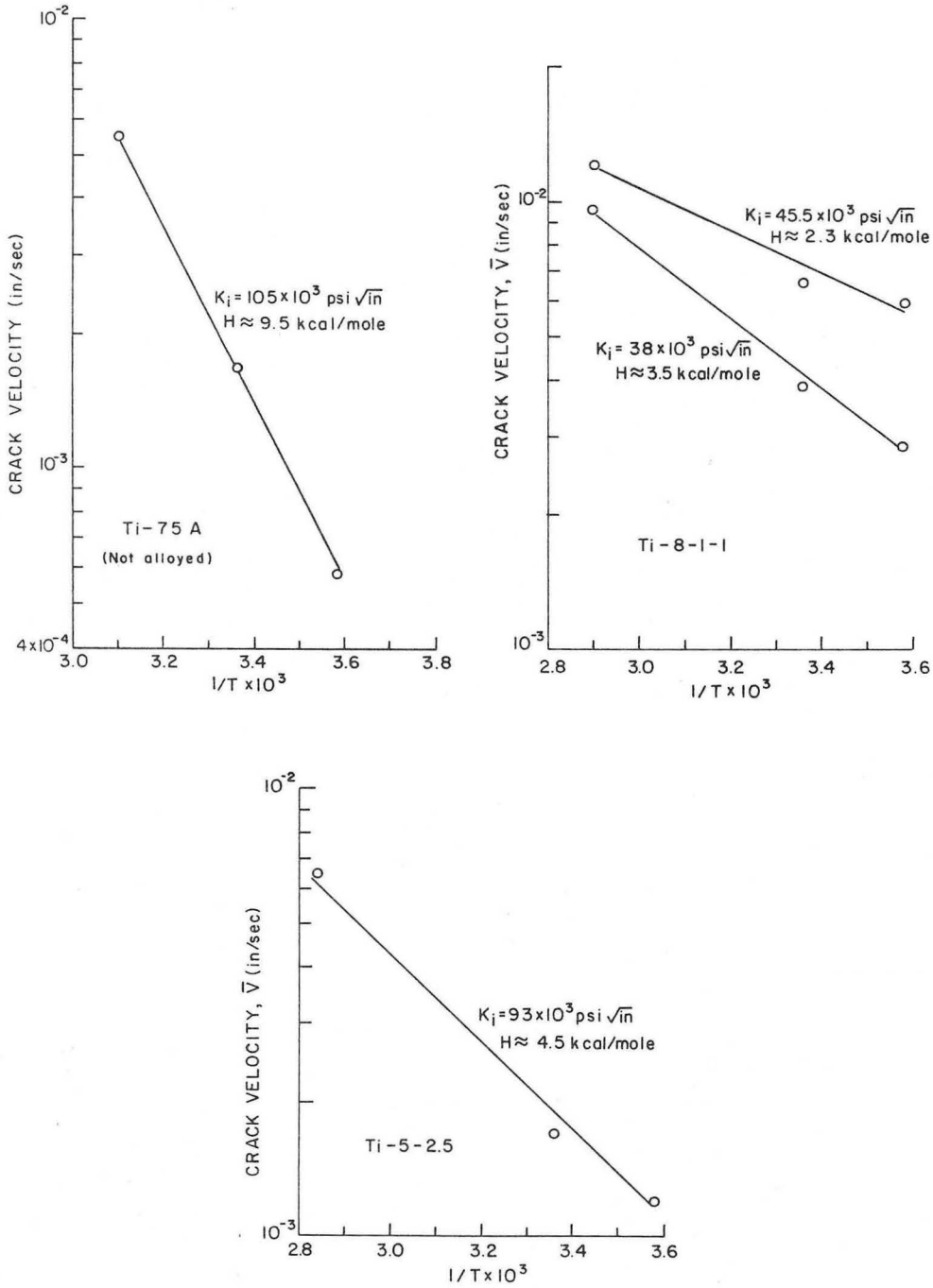

XBL 696-763

Figure 35

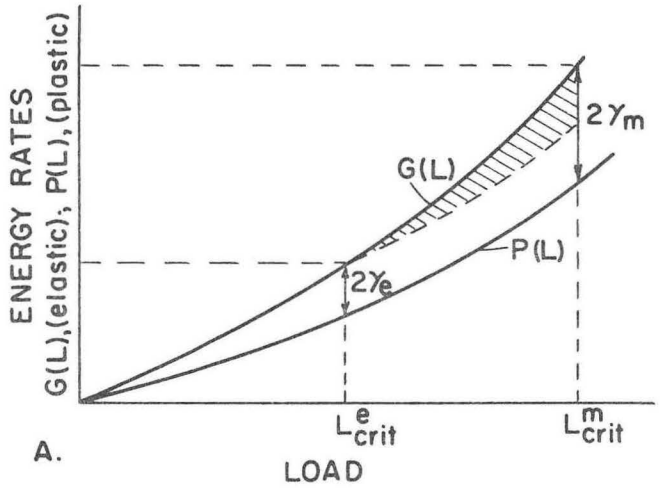

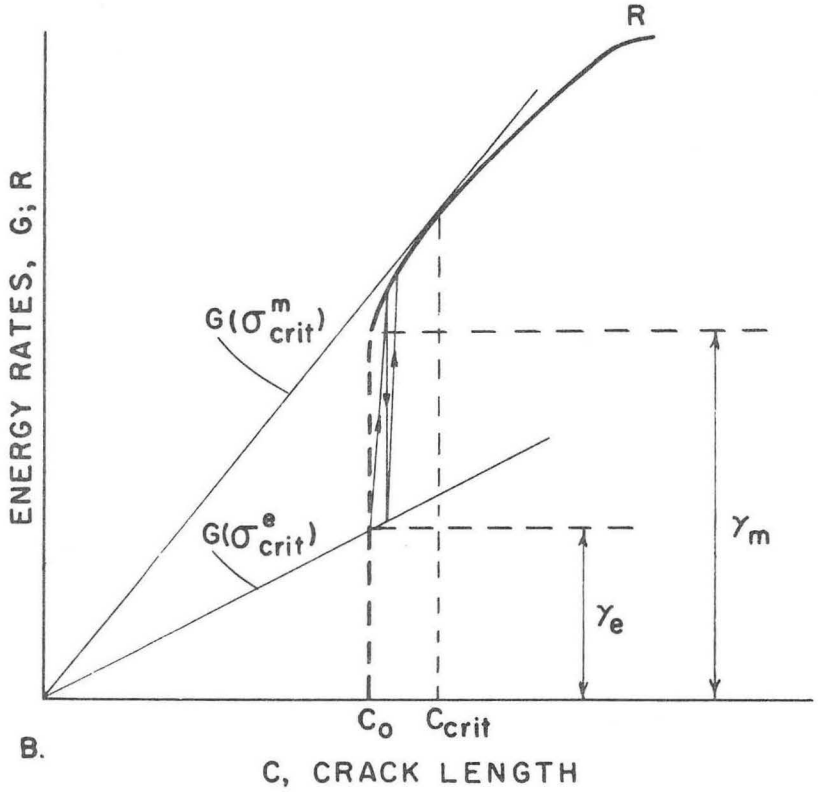

XBL 696-617

Figure 36

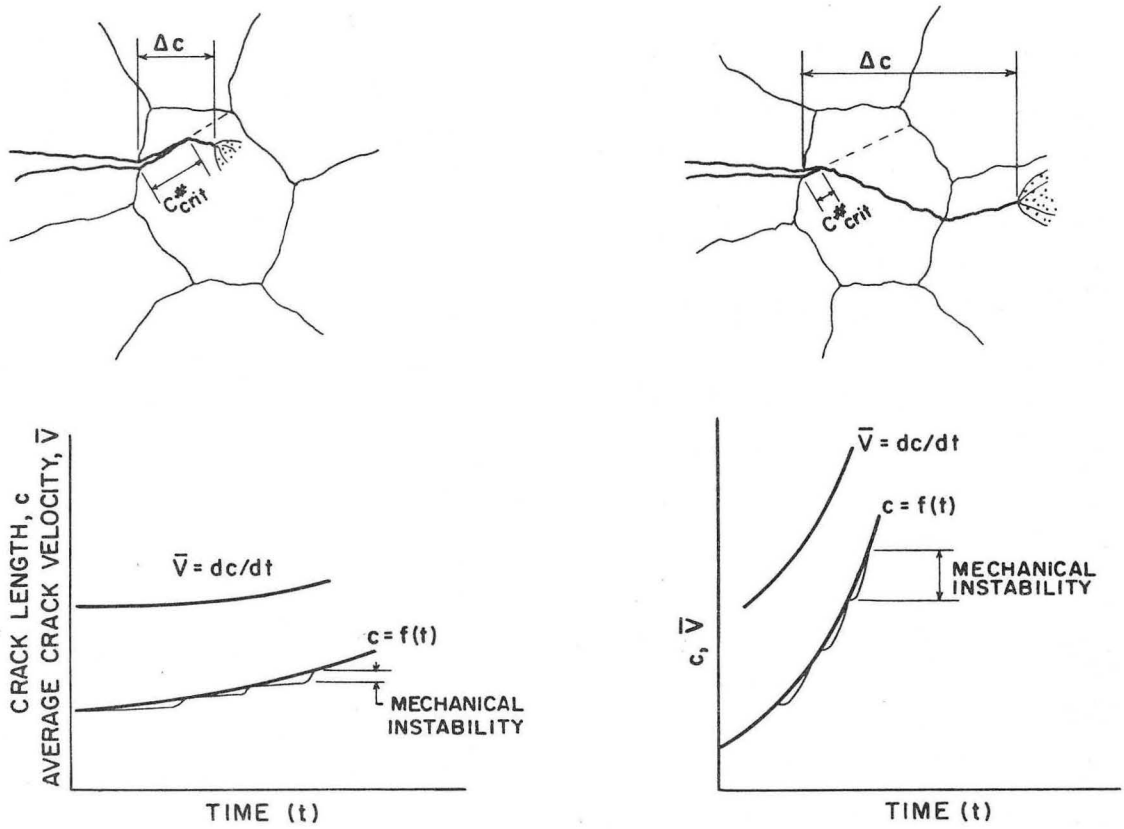

a. $K_{I_{scc}} < K_i << K_{Ic}$

b. $K_{I_{scc}} << K_i < K_{Ic}$

XBL 694-448

Figure 37

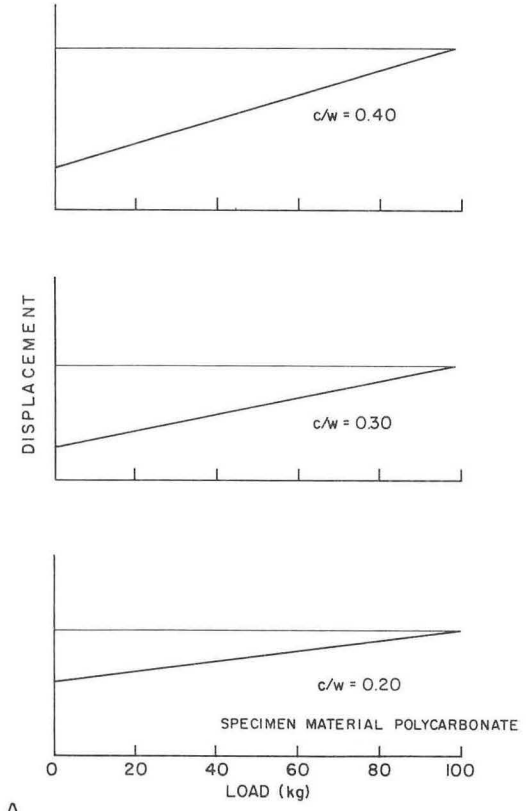

A.

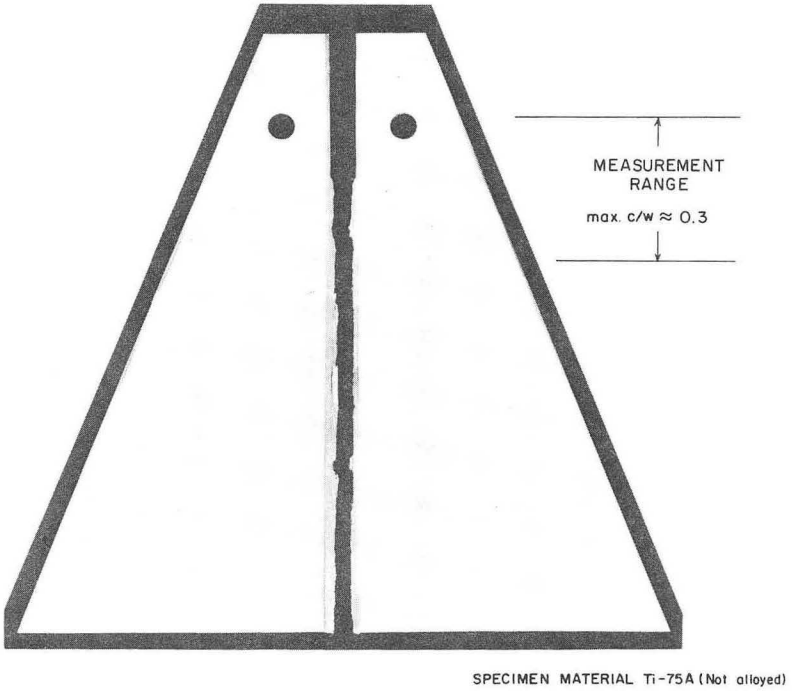

B.

XBB 696-3979

Figure 38

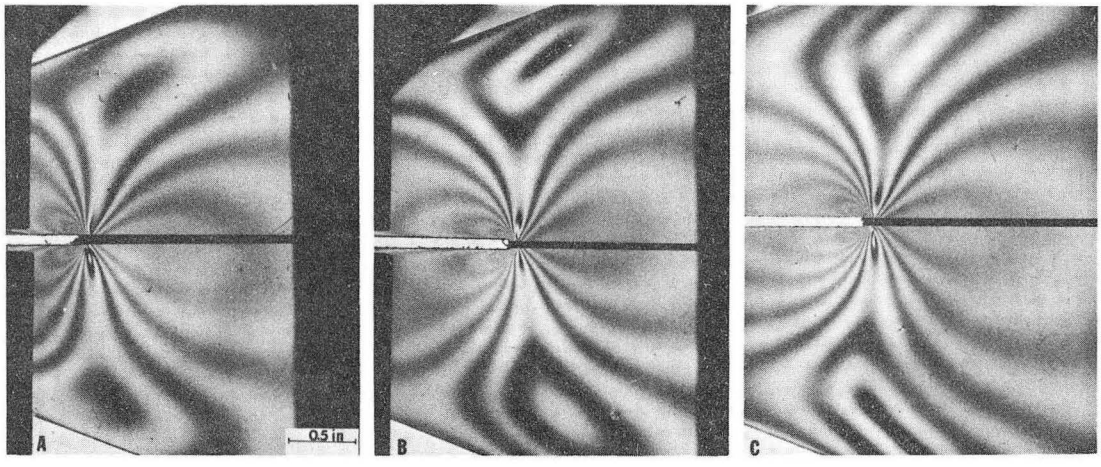

XBB 6812-7701

Figure 39

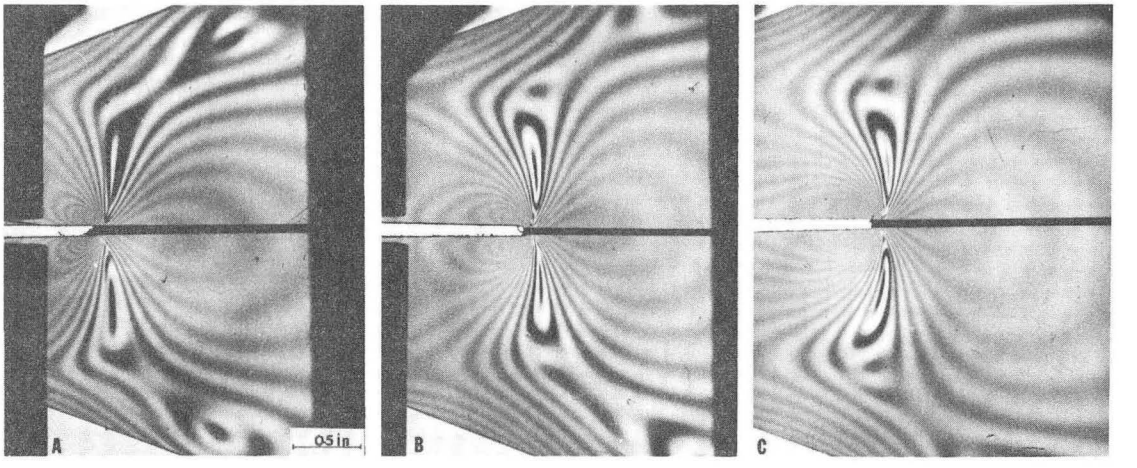

XBB 6812-7702

Figure 40

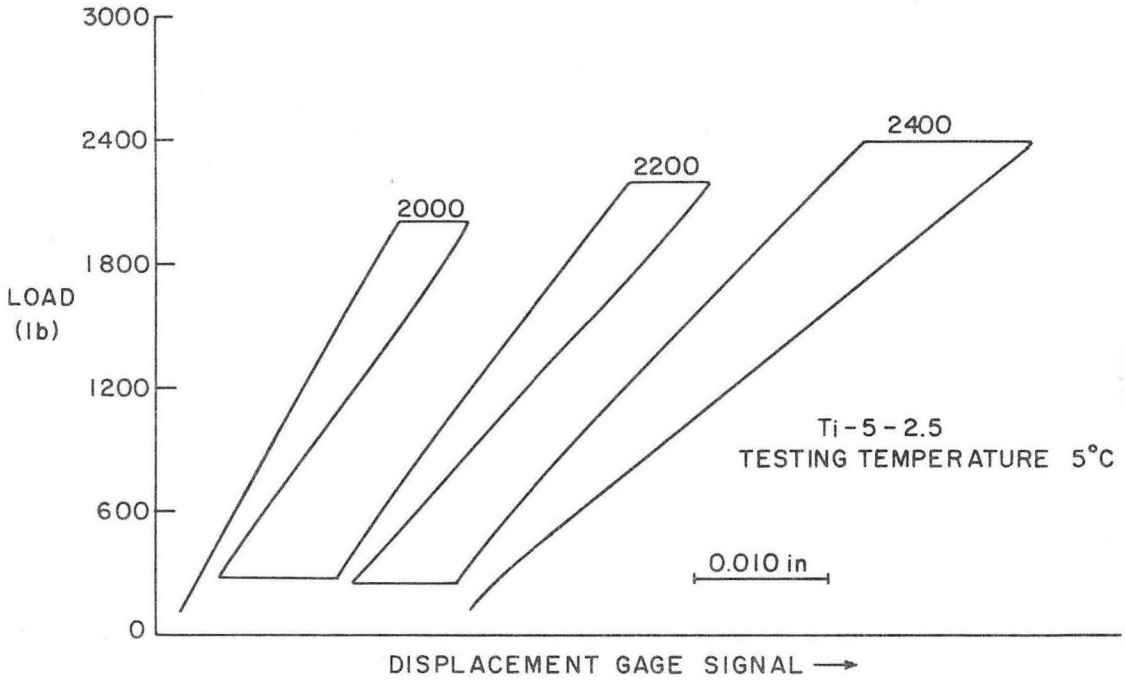

XBL 696-696

Figure 41

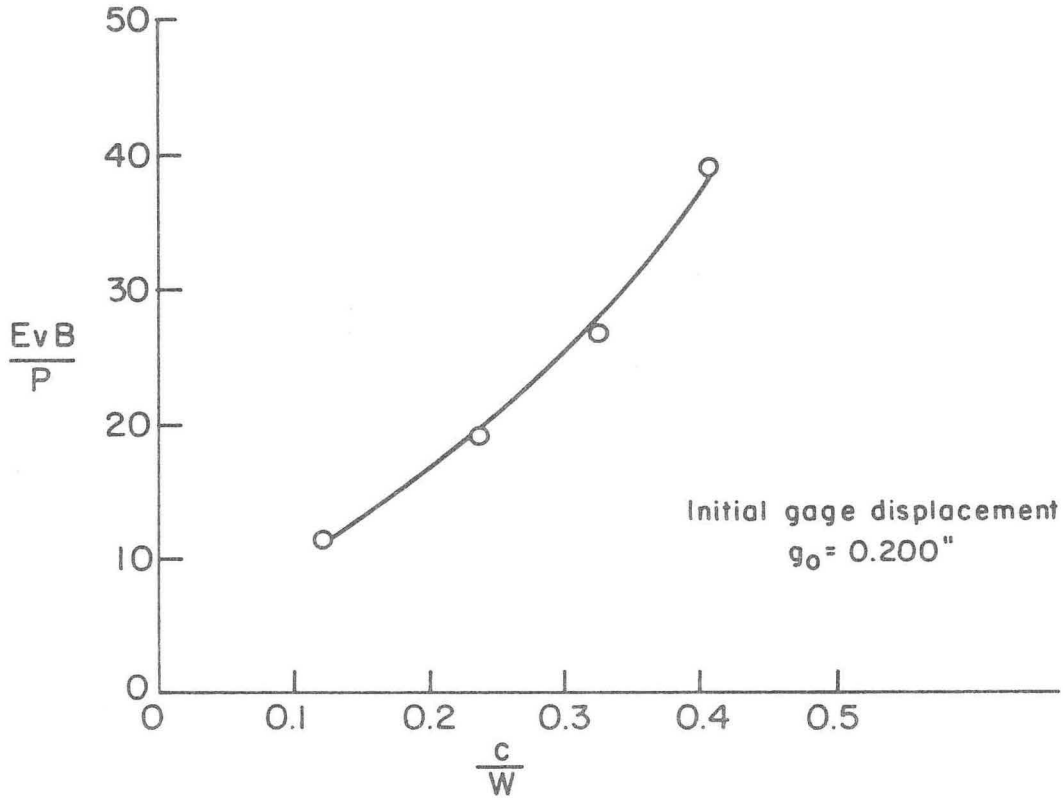

XBL 696-618

Figure 42

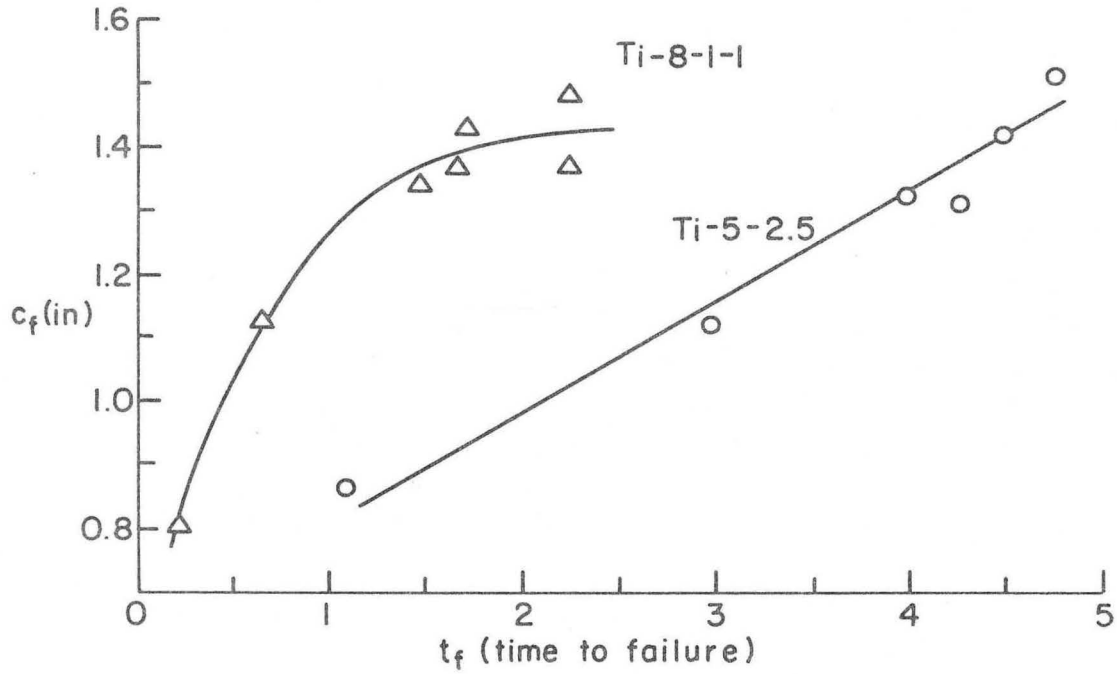

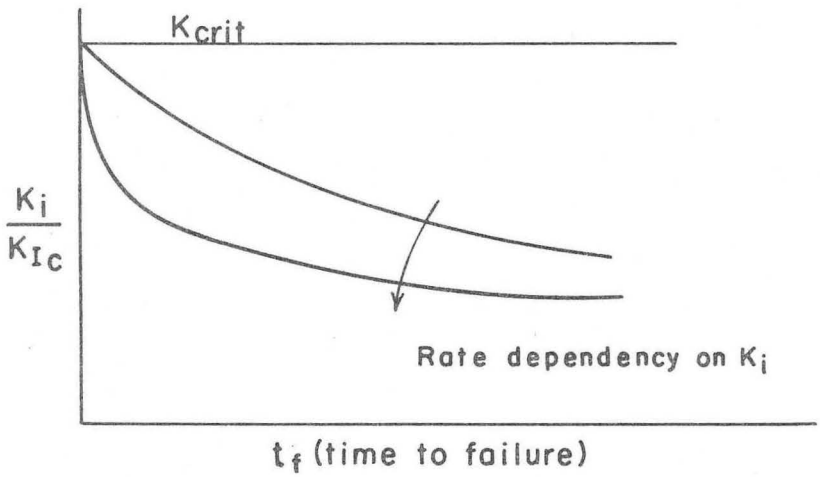

XBL 696-660

Figure 43

LEGAL NOTICE

This report was prepared as an account of Government sponsored work. Neither the United States, nor the Commission, nor any person acting on behalf of the Commission:

A. Makes any warranty or representation, expressed or implied, with respect to the accuracy, completeness, or usefulness of the information contained in this report, or that the use of any information, apparatus, method, or process disclosed in this report may not infringe privately owned rights; or

B. Assumes any liabilities with respect to the use of, or for damages resulting from the use of any information, apparatus, method, or process disclosed in this report.

As used in the above, "person acting on behalf of the Commission" includes any employee or contractor of the Commission, or employee of such contractor, to the extent that such employee or contractor of the Commission, or employee of such contractor prepares, disseminates, or provides access to, any information pursuant to his employment or contract with the Commission, or his employment with such contractor.

TECHNICAL INFORMATION DIVISION
LAWRENCE RADIATION LABORATORY
UNIVERSITY OF CALIFORNIA
BERKELEY, CALIFORNIA 94720